UC San Diego

UC San Diego Electronic Theses and Dissertations

Title

Plasmonic Metamaterials for Active and Passive Light Control /

Permalink

https://escholarship.org/uc/item/61s5d1w9

Author

Lu, Danyong Dylan

Publication Date

2014

Peer reviewed|Thesis/dissertation

eScholarship.org Powered by the California Digital Library
University of California

UNIVERSITY OF CALIFORNIA, SAN DIEGO

Plasmonic Metamaterials for Active and Passive Light Control

A dissertation submitted in partial satisfaction of the
requirements for the degree
Doctor of Philosophy

in

Electrical Engineering (Photonics)

by

Danyong Dylan Lu

Committee in charge:

Professor Zhaowei Liu, Chair
Professor Yeshaiahu Fainman
Professor Eric E. Fullerton
Professor Sungho Jin
Professor Paul K. Yu

2014

Copyright
Danyong Dylan Lu, 2014
All rights reserved.

The dissertation of Danyong Dylan Lu is approved, and it is acceptable in quality and form for publication on microfilm and electronically:

_____

_____

_____

_____

_____

Chair

University of California, San Diego

2014

DEDICATION

To my wife and our parents

EPIGRAPH

Let There Be Light

TABLE OF CONTENTS

Signature Page iii

Dedication iv

Epigraph v

Table of Contents vi

List of Figures viii

Acknowledgements xii

Vita xv

Abstract of the Dissertation xvii

Chapter 1 Introduction 1
1.1 Plasmonics and metamaterials 1
1.2 This thesis 4

Chapter 2 Plasmonic metamaterials: tunable plasmonic properties 6
2.1 Composite metamaterials 6
2.2 Multilayer hyperbolic metamaterials 14
2.3 Conclusion 18

Chapter 3 Multilayer hyperbolic metamaterials for enhancing spontaneous light emission 21
3.1 Introduction 21
3.2 Theoretical calculation and numerical design of Purcell factor and radiative enhancement 24
3.2.1 Analytical calculation 24
3.2.2 3D full-wave simulation 26
3.2.3 Calculation results of Purcell enhancement 27
3.3 Fabrication of multilayer hyperbolic metamaterials 37
3.4 Experimental demonstration 38
3.4.1 Time-resolved photoluminescence 38
3.4.2 Modeling of time-resolved spontaneous emission . 44
3.5 Discussion 46
3.6 Conclusion 47

Chapter 4 Plasmonic metamaterials for improving quantum-well light emitting devices . . . 49
4.1 Introduction . . . 49
4.2 Concept of plasmonic metamaterial enhanced QW LEDs 51
4.3 Theoretical and numerical designs . . . 54
4.4 Ag plasmonic metamaterials for enhancing blue QW LEDs 59
4.5 Ag-Si multilayer HMMs for enhancing green QWs . . . 61
4.6 Conclusion . . . 64

Chapter 5 Anomalously weak scattering in hyperbolic metamaterials . . . 66
5.1 Background . . . 66
5.2 Concept of AWS . . . 68
5.3 Numerical demonstration of AWS . . . 70
5.4 Experimental demonstration of AWS . . . 73
5.4.1 HMM fabrication . . . 73
5.4.2 Optical characterization . . . 74
5.4.3 AWS for optical stealth . . . 76
5.5 Discussion . . . 80
5.6 Conclusion . . . 80

Chapter 6 Plasmonic metamaterials for solar energy harvesting . . . 82
6.1 Introduction . . . 82
6.2 Theoretical modeling and design calculation . . . 85
6.3 Experimental demonstration . . . 89
6.3.1 Fabrication of multi-scaled SSCs . . . 89
6.3.2 Optical characterization of multi-scaled SSCs . . . 91
6.4 Discussion . . . 93
6.5 Conclusion . . . 93

Chapter 7 Summary and future directions . . . 95
7.1 Thesis summary . . . 95
7.2 Future directions . . . 97

Bibliography . . . 100

LIST OF FIGURES

Figure 1.1: Schematic of the dispersion relations of the free-space photon (dashed line) in the surrounding medium and SPPs (solid line). The inset shows the magnitude of electrical field along x direction for a SPP at metal-dielectric interfaces. 2

Figure 2.1: Schematic configuration of an oil-immersion optical microscope system for characterizing the SPP properties of composite metamaterial 8

Figure 2.2: Characterization of Ag-SiO_2 composite film. (a) SEM images; (b) Raw reflection images and normalized images; (c) Measured angular-resolved reflection spectra and theoretical fit. 9

Figure 2.3: Characterization of Ag-Si composite film. (a) SEM images; (b) Raw reflection images and normalized images; (c) Measured angular-resolved reflection spectra and theoretical fit. 10

Figure 2.4: SPP dispersion relations for Ag-SiO_2 and Ag-Si composite films. 13

Figure 2.5: (a) Schematic representation of metal-dielectric multilayer metamaterials. (b-d) Dispersion relations calculation for Ag-Al_2O_3 (b, Ag filling ratio 0.4), Ag-Al_2O_3 (c, Ag filling ratio 0.5), and Ag-Si (d, Ag filling ratio 0.5) multilayer metamaterials. 16

Figure 2.6: Multilayer HMM fabrications. (a) Cross-sectional SEM image of a Ag-Al_2O_3 multilayer. (b,c) Cross-sectional scanning transmission electron microscopy image of a Ag-Si multilayer (b) and a Au-Si multilayer (c). 17

Figure 2.7: Optical characterization of different metal-dielectric multilayer HMMs. (a) Optical transmission measurement of a Ag-Al_2O_3 multilayer HMM. (b) Optical transmission spectra of Ag-Si multilayer HMMs. The Ag filling ratio varies from 95% to 70%. . . 18

Figure 2.8: Nanopatterning Ag-Si multilayer HMMs. (a,b) SEM images of grating and hole array into the multilayer HMMs by focused ion beam milling. (c) SEM images of multilayer nanodisks by reactive ion etching. 19

Figure 3.1: Schematics of the light emitter-substrate interaction systems: (a) a metal film, (b) a uniform multilayer HMM, and (c) a nanopatterned multilayer HMM. 24

Figure 3.2: (a) Dispersion relations for EM waves at the interfaces between metals and a dielectric medium, (b) Purcell factor calculated for isotropic dipole emitters located a distance of $d = 10$ nm above a 200 nm thick metal of Ag, Al, and Au on a glass substrate. . 29

Figure 3.3: (a) Purcell factor for isotropic dipole emitters located at uniform Ag-Si multilayer HMMs. (b) Purcell factor, (c) radiative enhancement, and (d) EQE enhancement for the uniform multilayer HMM surface with a Ag filling ratio of 0.6. 32
Figure 3.4: (a) Radiative emission, (b) plasmonic modes, and (c) lossy-wave component for different distances away from uniform Ag-Si multilayer HMM. Three channels of decay rate enhancement as a function of the distance (d) and the emission wavelength (e). . . 33
Figure 3.5: (a) Normalized dissipated power spectra and (b) Purcell factor for a dipole above the uniform Ag-Si multilayer as depicted in the inset. 34
Figure 3.6: Cross-sectional mapping of Purcell factor (a) and radiative enhancement (b) for HMMs. (c) and (d) correspond to the dashed lines in (a) and (b). Purcell factor (e) and radiative enhancement (f) as a function of emission wavelength. 36
Figure 3.7: Simulated EQE enhancement as a function of the emission wavelength for isotropic dipoles at locations indicated in Figure 3.6. 37
Figure 3.8: Nanopatterned multilayer HMMs. (a) Schematic configuration. (b) SEM image of one of the fabricated nanopatterned HMMs. (c) Dark-field STEM images of the cross-sections of Ag-Si multilayers. (d) Element mapping for the constituent materials. . . 39
Figure 3.9: Experimental measurements and theoretical fit of time-resolved fluorescence for dye molecules on different plasmonic samples. . 41
Figure 3.10: Theoretical fit to the maximum and minimum decay rates of time-resolved fluorescence measurements for R6G on nanopatterned Ag-Si HMM and Ag grating. 42
Figure 3.11: (a) Purcell factor for a dipole located $d = 10$ nm above the uniform Si film with a thickness of 305 nm. (b) Time-resolved fluorescence measurements for R6G on the uniform Si film (in black) and Si grating with a period of 200 nm (in blue). 43
Figure 3.12: Experimental demonstration of the geometrical dependence of Purcell and fluorescence intensity enhancement. (a) Lifetime and (b) Fluorescence intensity enhancement for R6G on the Ag-Si HMM with different grating periods. 43
Figure 3.13: Averaged fluorescence intensity as a function of the location along the x axis across the regions of nanopatterned and uniform Ag-Si HMMs. 44

Figure 4.1: Plasmonic metamaterials for enhancing QW LEDs at different wavelengths. (a) Ag based metamaterials for blue QW LEDs. (b) nanopatterned Ag-Si multilayer HMMs for green QW LEDs. (c) Purcell factor calculation for uniform Ag-Si multilayer HMMs. 53

Figure 4.2: Numerical simulation for Ag plasmonic metamaterials. (a) One unit cell. (b) Purcell factor and radiative enhancement for a QW dipole parallel to a Ag nanodisk array. (c,d) Maxima of Purcell factor and radiative enhancement as the period (c) and the diameter (d) varies. 55
Figure 4.3: Numerical simulation for Ag-Si multilayer HMMs. (a) One unit cell. (b) Purcell factor and radiative enhancement for a QW dipole parallel to a Ag-Si multilayer nanodisk array. Maxima of Purcell factor and radiative enhancement as the period (c) and diameter (d) varies. 57
Figure 4.4: Numerical simulation for the spatial distribution of Purcell factor (a) and radiative enhancement (b) of QW dipole emitters in x-y plane at a distance of 10 nm away from nanopatterned Ag-Si multilayer plasmonic metamaterials. 58
Figure 4.5: (a) Schematic drawing of typical cross-section of a LED structure and optical images of two grown LED samples targeting different emission wavelengths. (b) Photoluminescence spectra of two grown InGaN/GaN multi-QW LED samples. 59
Figure 4.6: Electrically-pumped Ag plasmonic metamaterial enhanced QW LEDs. (a) Schematic cross-section layout. (b) Images of Ag plasmonic LED. (c) Optical image of the electroluminescence intensity. (d) Electroluminescence spectra for areas in (b). . . . 61
Figure 4.7: Time-resolved photoluminescence of QW LEDs. (a) Time correlated single photon counting and spatial mapping. (b) Measurement for bare QWs, QWs with nanopatterned Ag-Si multilayer HMMs. 63
Figure 4.8: Spatial Purcell factor mapping of green QW LED with nanopatterned Ag-Si multilayer HMMs with the array period 200 nm (a), 250 nm (b), and 300 nm (c) at the wavelength of 520 nm, and corresponding SEM images (d-f). 64

Figure 5.1: Schematics of anomalously weak scattering (AWS) by multilayer HMMs. EM plane waves are strongly scattered by an obstacle made of pure metal (a) or high-index dielectric (b), whereas AWS occurs for the obstacle made of HMMs (c). 70
Figure 5.2: Numerical simulations of slit scattering in HMMs. (a) Electric field distributions for a single slit in Au film (i), Si film (ii), and Au-Si HMMs (iii, iv). (b) Real and imaginary parts of the HMM permittivities. (c) Scattering intensity spectra for a slit. . 72
Figure 5.3: Simulated electric field distributions when a plane wave polarized perpendicular to the incident plane at the wavelength of 480 nm (a) and 700 nm (b) propagates through a single slit in the Au-Si HMM. 74

Figure 5.4: Fabrication of Au-Si multilayer HMMs. (a) Bright-field STEM images, (b) Element mapping for constituent materials. 75
Figure 5.5: Optical scattering spectra of individual slits in the Au-Si HMM. (a) Measured dark-field scattering spectra and (b) simulated scattering spectra for individual slits with different widths in the Au-Si HMM under TE-polarized light. 76
Figure 5.6: Measured scattering spectra in the forward direction for individual slits with a 150 nm width in the Au-Si HMM under TE and TM wave incidence at an angle of 53°. 77
Figure 5.7: Spectrum and imaging characterization of holes in Au-Si HMMs. (a) Forward dark-field scattering spectrum of individual holes. (b) SEM image of distributed holes. (c) Forward dark-field scattering images and (d) transmission images in pseudo colors. . . 78
Figure 5.8: Characterization of AWS by shaped patterns in Au-Si HMMs. (a) Top: SEM image. Bottom: measured dark-field scattering spectrum. (b) SEM image of the UCSD logo (i). Dark-field scattering images at 485 nm (ii), 540 nm (iii), and 735 nm (iv). 79

Figure 6.1: Spectrally selective coating (SSC) for concentrated solar power. (a) Schematic of a solar absorber with stainless steel (SS) tube coated with the SSC. (b) Optical reflectance of an ideal SSC. . 84
Figure 6.2: Optical modeling system for the SSC. The nanostructured SSC in (a) is modeled by a multilayer system consisting of a gradient refractive index layer and a uniform effective layer on the SS substrate as schematically shown in (b). 86
Figure 6.3: Numerical simulation results of the reflectance spectra for the SSC. (a) Reflectance with respect to incident wavelengths and the volumetric filling ratios. (b) Reflectance of the SSC layer when the filling ratio of the nanoparticles is equal to 0.75. . . . 88
Figure 6.4: Numerical simulation results of the reflectance spectra with respect to different incident wavelengths and collection angles when the volumetric filling ratio of the nanoparticles is fixed at 0.75. (a) P-polarized waves; (b) S-polarized waves. 88
Figure 6.5: Characterization of the SSCs. (a-b) SEM images of the SSC. (c-d) SEM images of the SSC made by Si nanoparticles. SEM images of the same Si-Ge sample (e) before and (f) after annealing at 750°C in air for 1 hour. 90
Figure 6.6: (a) Measured reflectance of the SSCs in the UV to near-IR regime. (b) Measured IR emission spectra at 500°C. The black curve in (b) is the normalized blackbody spectrum at 500°C. . . 92

ACKNOWLEDGEMENTS

I would like to express my deepest gratitude to my advisor, Prof. Zhaowei Liu, for his precious detailed advice and kind support throughout my PhD research, study and life. He opened the door for me to an exciting research area of plasmonics and metamaterials, and guided me through difficulties with his insightful perspectives. Not only his physics pictures and solid knowledge but also his attitude and strategies to group and project management inspire me a lot. Brainstorming and rigorous training from him will benefit me in my future professional life.

I would like to thank Prof. Shaya Y. Fainman, Prof. Eric E. Fullerton, Prof. Sungho Jin, and Prof. Paul K. Yu for serving on my PhD committee. My research outcome and dissertation will not be possible without their fruitful guidance, continuous experimental collaboration and generous hardware support.

Also, I want to extend my thankfulness to Prof. Renkun Chen, Dr. Michelle Digman, Prof. Enrico Gratton, Prof. Deli Wang, Prof. Jie Xiang, Prof. Sunil Sinha, Prof. Yongmin Liu, Prof. Liang Feng, and Peng Zhang for their collaborations and discussions, and Prof. Shayan Mookherjea, Prof. Sadik Esener, Prof. Stojan Radic, and Prof. Kevin Quest for their instructions, and also the ECE and OGS officers, specially, Miss Shana Slebioda, Stefanie Battaglia, Tawnee Gomez, Samantha Garcia, Jennifer Kim, and Yahira Cordero for their kind help.

Furthermore, I would like to thank my group fellows, collaborators, Nano3 staff, and all my colleagues and friends in UCSD and other universities for discussions and assistance. My previous and current group fellows are Feifei Wei, Haoliang Qian, Bryan VanSaders, Kangwei Wang, Lorenzo Ferrari, Weiwei Wan, Li Chen, Hao Shen, Joshua Hoemke, Qian Ma, Dominic Lepage, Joseph Ponsetto, Eric Huang, Bahar Khademhosseinieh, Justin Park, Dae Yup Han, Changbao Ma, Houdong Hu, Ryan Aguinaldo, Marco Escobar, Wenwei Zheng, Yunfeng Jiang, Conrad Rizal, Devin Cela, and Conor Riley. Distinguished collaborators include Jimmy J. Kan, Jaeyun Moon, Edward Dechaumphai, Wei Lu, Hongtao Chen, Jingjin Song. Sanwen Chen, Yuchun Zhou, Ke Sun, Ali Kargar, and Tae Kyoung Kim. And Nano3 staff includes but not limit to Bernd Fruhberger, Larry Grissom,

Sean Parks, Xuekun Lu, Maribel Montero, Ryan Anderson, and Ivan Harris.

Besides, I appreciate my previous training received from Prof. Zhao-Qing Zhang and colleagues for my master degree in Hong Kong, as well as Prof. Shi-Ning Zhu and Prof. Hui Liu in my undergrad Nanjing University.

Last but not least, I am grateful and dedicate this thesis to my wife Yan, our parents and family. Thanks for their unconditional endless support and encouragements in my life and study.

Chapter 1 and 2, in part, are reprints of the material as it appears on Appl. Phys. Lett. 98, 243114 (2011). Dylan Lu, Jimmy Kan, Eric E. Fullerton, and Zhaowei Liu, "Tunable surface plasmon polaritons in Ag composite films by adding dielectrics or semiconductors." The dissertation author was the first author of this paper.

Chapter 2, in part, is being prepared for submission for publication. Dylan Lu, Haoliang Qian, Kangwei Wang, Feifei Wei, Eric E. Fullerton, Paul K. Yu, and Zhaowei Liu, "Multilayer hyperbolic metamaterials speeding up green InGaN/GaN quantum wells (tentative)." The dissertation author was the first author of this paper.

Chapter 3, in part, is a reprint of the material as it appears on Nature Nanotech. 9, 48-53 (2014). Dylan Lu, Jimmy J. Kan, Eric E. Fullerton, and Zhaowei Liu, "Enhancing spontaneous emission rates of molecules using nanopatterned multilayer hyperbolic metamaterials." The dissertation author was the first author of this paper.

Chapter 3, in part, is being prepared for submission for publication. Dylan Lu, Lorenzo Ferrari, Jimmy J. Kan, Eric E. Fullerton, and Zhaowei Liu, "Nanopatterned multilayer hyperbolic metamaterials for spontaneous light emission control." The dissertation author was the first author of this paper.

Chapter 4, in part, is being prepared for submission for publication. Dylan Lu, Haoliang Qian, Kangwei Wang, Bryan VanSaders, Paul K. Yu, and Zhaowei Liu, "Plasmonic metamaterial enhanced InGaN/GaN blue light-emitting diodes (tentative)." The dissertation author was the first author of this paper.

Chapter 4, in part, is being prepared for submission for publication. Dylan Lu, Haoliang Qian, Kangwei Wang, Feifei Wei, Eric E. Fullerton, Paul K. Yu, and Zhaowei Liu, "Multilayer hyperbolic metamaterials speeding up green InGaN/GaN quantum wells (tentative)." The dissertation author was the first author of this paper.

Chapter 5, in part, is being prepared for submission for publication. Hao Shen, Dylan Lu, Bryan VanSaders, Jimmy J. Kan, Hongxing Xu, Eric E. Fullerton, and Zhaowei Liu, "Anomalously weak scattering in metal-semiconductor multilayer hyperbolic metamaterials." The dissertation author was the co-first author of this paper.

Chapter 6, in part, is a reprint of the material as it appears on Nano Energy 8, 238-246 (2014). Jaeyun Moon, Dylan Lu, Bryan VanSaders, Tae Kyoung Kim, Seong Deok Kong, Sungho Jin, Renkun Chen, and Zhaowei Liu, "High performance multi-scaled nanostructured spectrally selective coating for concentrating solar power." The dissertation author was the co-first author of this paper.

VITA

2007	B.S. in Physics, Nanjing University
2007-2009	Teaching Assistant, Department of Physics, Hong Kong University of Science and Technology
2007-2009	Research Assistant, Hong Kong University of Science and Technology
2009	M.Phil. in Physics, Hong Kong University of Science and Technology
2009-2014	Research Assistant, University of California, San Diego
2014	Ph.D. in Electrical Engineering (Photonics), University of California, San Diego

PUBLICATIONS

D. Lu, H. Qian, K. Wang, B. VanSaders, P. K. Yu, and Z. Liu, "Plasmonic metamaterial enhanced InGaN/GaN blue light-emitting diodes (tentative)," Paper under preparation.

D. Lu, H. Qian, K. Wang, F. Wei, E. E. Fullerton, P. K. Yu, and Z. Liu, "Multilayer hyperbolic metamaterials speeding up green InGaN/GaN quantum wells (tentative)," Paper under preparation.

D. Lu, and Z. Liu, "Hyperlenses and Metalenses," Book Chapter under preparation.

D. Lu, L. Ferrari, J. J. Kan, E. E. Fullerton, and Z. Liu, "Nanopatterned multilayer hyperbolic metamaterials for spontaneous light emission control," Paper under preparation.

F. Wei, **D. Lu**, R. Aguinaldo, Y. Ma, S. K. Sinha, and Z. Liu, "Localized surface plasmon assisted high contrast microscopy for ultrathin transparent specimen," Paper submitted.

H. Shen*, **D. Lu***, B. VanSaders, J. J. Kan, H. Xu, E. E. Fullerton, and Z. Liu, "Anomalously weak scattering in metal-semiconductor multilayer hyperbolic metamaterials," Paper submitted.

F. Wei, **D. Lu**, H. Shen, W. Wan, J. Ponsetto, E. Huang, and Z. Liu, "Wide Field Super-Resolution Surface Imaging Through Plasmonic Structured Illumination Microscopy," *Nano Letters* 14, 4634-4639 (2014).

J. Moon*, **D. Lu***, B. VanSaders, T. K. Kim, S. D. Kong, S. Jin, R. Chen, and Z. Liu, "High performance multi-scaled nanostructured spectrally selective coating for concentrating solar power," *Nano Energy* 8, 238-246 (2014).

E. Dechaumphai, **D. Lu**, J. J. Kan, J. Moon, E. E. Fullerton, Z. Liu, and R. Chen, "Ultralow thermal conductivity of multilayers with highly dissimilar Debye temperatures," *Nano Letters* 14, 2448-2455 (2014).

L. Ferrari, **D. Lu**, D. Lepage, and Z. Liu, "Enhanced spontaneous emission inside hyperbolic metamaterials," *Opt. Express* 22, 4301-4306 (2014).

D. Lu, J. J. Kan, E. E. Fullerton, and Z. Liu, "Enhancing spontaneous emission rates of molecules using nanopatterned multilayer hyperbolic metamaterials," *Nature Nanotech.* 9, 48-53 (2014).

A. Kargar, K. Sun, S. Kim, **D. Lu**, Y. Jing, Z. Liu, X. Pan, and D. Wang, "Three-dimensional ZnO/Si broom-like nanowire heterostructures as photoelectrochemical anodes for solar energy conversion," *Phys. Status Solidi A* 1-8 (2013).

D. Lu, and Z. Liu, "Hyperlenses and metalenses for far-field super-resolution imaging," *Nature Comm.* 3, 1205 (2012).

D. Lu, J. J. Kan, E. E. Fullerton, and Z. Liu, "Tunable surface plasmon polaritons in Ag composite films by adding dielectrics or semiconductors," *Appl. Phys. Lett.* 98, 243114 (2011).

*These authors contributed equally to this work.

ABSTRACT OF THE DISSERTATION

Plasmonic Metamaterials for Active and Passive Light Control

by

Danyong Dylan Lu

Doctor of Philosophy in Electrical Engineering (Photonics)

University of California, San Diego, 2014

Professor Zhaowei Liu, Chair

Fundamental study on plasmonics excites surface plasmons opening possibility for stronger light-matter interaction at nanoscales and optical frequencies. On the other hand, metamaterials, known as artificial materials built with designable subwavelength units, offer unprecedented new material properties not existing in nature. By combining unique advantages in these two areas, plasmonic metamaterials gain tremendous momentum for fundamental research interest and potential practical applications through the active and passive interaction with and control of light. This thesis is focused on the theoretical and experimental study of plasmonic metamaterials with tunable plasmonic properties, and their applications in controlling spontaneous emission process of quantum emitters, and manipulating light propagation, scattering and absorption.

To break the limitation of surface plasmon properties by existing metal materials, composite- and multilayer-based metamaterials are investigated and their tunable plasmonic properties are demonstrated. Nanopatterned multilayer metamaterials with hyperbolic dispersion relations are further utilized to enhance spontaneous emission rates of molecules at desired frequencies with improved far-field radiative power through the Purcell effect. Theoretical calculations and experimental lifetime characterizations show the tunable broadband Purcell enhancement of 76 fold on the hyperbolic metamaterials that better aligns with spontaneous emission spectra and the emission intensity improvement of 80 fold achieved by the out-coupling effect of nanopatterns. This concept is later applied to quantum-well light emitting devices for improving the light efficiency and modulation speed at blue and green wavelengths.

On the passive light manipulation, in contrast to strong plasmonic scattering from metal patterns, anomalously weak scattering by patterns in multilayer hyperbolic metamaterials is observed and experimentally demonstrated to be insensitive to pattern sizes, shapes and incident angles, and has potential applications in scattering cross-section engineering, optical encryption, low-observable conductive probes and opto-electric devices. Lastly, the concept of metamaterials is also extended to selective control of light absorption and reflection for potential solar energy applications. A high-performance spectrally selective coating based on multi-scaled metamaterials is designed and fabricated with 90-95% solar absorptivity and <30% infrared emissivity near the peak of 500°C black body radiation, which can be utilized for designing solar absorbers with high thermal efficiency for future high temperature concentrating solar power systems.

Chapter 1

Introduction

1.1 Plasmonics and metamaterials

Studies on the fundamental properties of surface plasmon polaritons (SPPs) have provided better understanding of physical phenomena in the field of plasmonic science and have inspired exciting applications of SPP based structures and devices [1, 2, 3]. SPPs, also known as surface plasmons (SPs), are quasi-particles excited at metal-insulator interfaces through resonant coupling of electromagnetic (EM) waves to the free electrons in the metal [4]. These EM waves are propagating along the interfaces while being evanescently confined along the direction perpendicular to the interfaces as shown in the inset of Figure 1.1.

The dispersion relation of SPPs can be derived based on the Maxwell's equations and the boundary conditions at the interface. The SPP wavevector for semi-infinite metal-dielectric interface can be written as [4],

$$k_{\mathrm{SPP}} = k_0 \sqrt{\frac{\epsilon_1 \epsilon_2}{\epsilon_1 + \epsilon_2}} \tag{1.1}$$

with k_0 representing the wavevector of light in free space, ϵ_1 and ϵ_2 representing the dielectric constants of metal and dielectric, respectively. A typical dispersion curve for SPPs at metal-air interfaces described by Equation (1.1) is represented by the red line in Figure 1.1. It approaches a SP resonance frequency $\omega_{\mathrm{SP,Air}}$ as the slop, corresponding to the group velocity, goes to zero. This SP resonance frequency can be tuned to lower frequencies by changing to higher-index dielectric interface

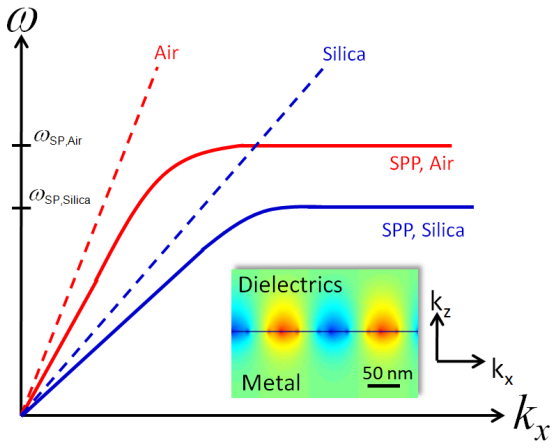

Figure 1.1: Schematic of the dispersion relations of the free-space photon (dashed line) in the surrounding medium and SPPs (solid line). The inset shows the magnitude of electrical field along x direction for a SPP at metal-dielectric interfaces.

as the blue line in Figure 1.1. Since the dispersion curves of SPPs always lie on the right side to that of the free-space photon in surrounding media (dashed lines in Figure 1.1), k_{SPP} is always larger than the corresponding k_{Photon}. And such wavevector mismatch depends strongly on the incident frequency, the refractive index of the surrounding dielectric, and the property of the metal film.

To compensate the momentum mismatch between SPPs and free-space photons, coupling schemes are required in order to realize the inter-conversion between these two states. One of the effective coupling schemes is like in a prism coupling structure: free-space photon from a relatively higher-index medium side could overlap with the dispersion curve of SPP at the other lower-index medium interface and therefore provides large enough wavevector at a resonance angle for SPP excitation at the lower-index side. Another approach to excite SPP is simply by near field excitation. Some scattering centers or emission points placed to the near field of metal surface will have sufficient-intensity high wavevector components to excite SPPs. The third effective way is to use patterned nanostructures, like a grating structure, that could provide a series of additional resonant diffraction wavevectors to compensate the mismatch. When the summation of the momentum provided by the grating structure and the in-plane momentum of the illumination photon equals that of the SPP, metal SPPs could be effectively excited on the same side.

By well combination of these coupling schemes, SPPs could be effectively manipulated and utilized. For example, an emission medium could be used in the near field to excite the metal SPPs whereas a grating structure could out-couple these excited SPPs back to free-space photons for far-field collection of the light-matter interaction.

With deep understanding of the nature of SPPs, a lot of plasmonic applications have been made possible with concurrent advances in nanotechnology. Based on the nanoscale energy concentration and quick response speed of SPPs, these applications include light guiding and manipulation at the nanoscale [5, 6], sub-diffraction-limited optical imaging [7, 8], highly sensitive detection [9, 10], ultrafast optoelectronic devices [11, 12], highly efficient light emission [13, 14], and enhanced solar energy efficiency [15, 16]. Yet, all these applications so far strongly rely on the unique wavelength-dependent SPP mode properties and the dispersive permittivity profiles associated with a set of existing materials. Well known plasmonic materials in the optical regime have limited selections, including Al, Ag, and Au. Therefore, it leads to the quest for new materials for extensive and tunable plasmonic study and applications.

Metamaterials, known as artificial materials built with designable subwavelength units, offer unprecedented new material properties not existing in nature. Since the building unit cells in metamaterials are subwavelength, the macroscopic properties of metamaterials, including permittivity, permeability, refractive index and impedance, can be described by an effective medium approximation [17, 18]. In addition to mimic nature materials, the most interesting phenomenon made possible only by metamaterials is negative refraction and negative index materials. After the first experimental demonstration of negative refraction in microwave frequency in 2001 [19], a tremendous research interests and efforts emerge paving the way to the realization of negative refraction in optical frequency with various types of configurations [20, 21] as well as multifunctional devices [22]. A generalized manipulation of light propagation by metamaterials was inspired by the concept of transformation optics [23, 24], and was later demonstrated for the EM wave cloaking at microwave and optical frequencies [25, 26].

Built on the extraordinary control of light by metamaterials, one of the most useful applications focused on sub-diffraction-limited optical imaging. Initiated by a concept of the perfect lens proposed by Pendry [27], a number of super-lenses were demonstrated with resolving powers beyond the diffraction limit [7, 28, 29]. The optical superlens first achieved sub-diffraction-limited resolution by enhancing evanescent waves through a slab of silver although limited to the near field [7]. Far-field super-resolution imaging was later realized by employing a metamaterial-based lens, the hyperlens, with a magnification mechanism [28, 29]. Based on the transformation optics, flat hyperlenses with better adaption to real bio-imaging situation with larger imaging field could also become possible utilizing well-engineered metamaterial properties [30, 31].

1.2 This thesis

In this thesis, we will theoretically study and experimentally demonstrate extraordinary material properties of plasmonic metamaterials with tunable plasmonic responses, and their applications in controlling spontaneous emission process of quantum emitters, and manipulating light propagation, scattering and absorption.

Earlier in Chapter 1, we briefly introduce some background about SPPs and metamaterials, and their respectively interesting and useful applications.

Chapter 2 investigates two possible plasmonic metamaterials for tunable plasmonic properties. Composite metamaterials are first discussed with their effective material properties experimentally characterized and theoretically fitted. Later, multilayer-based metamaterials as an alternative material system are introduced and their optical characterizations are presented.

Chapters 3 and 4 focus on the control of spontaneous emission process of fluorescence molecules and quantum well light emitting diodes by nanopatterned plasmonic metamaterials. Chapter 3 mainly talks about the enhancement of spontaneous emission rates of molecules with improved radiative power by nanopatterned multilayer hyperbolic metamaterials. This concept is applied to the quantum well

system in Chapter 4 for improved LED intensity and enhanced modulation speeds.

Chapters 5 and 6 utilize metamaterials for controlling light propagation and absorption. Chapter 5 describes an approach to control the EM wave scattering by engineering the material properties of anisotropic multilayer-based metamaterials. An anomalously weak scattering is demonstrated. Whereas, in Chapter 6, a high-performance spectrally selective coating based on a multi-scaled metamaterials is reported for a concentrating solar power system.

In the end, Chapter 7 summarizes this thesis and discusses several future directions based on plasmonic metamaterials.

Chapter 1, in part, is a reprint of the material as it appears on Appl. Phys. Lett. 98, 243114 (2011). Dylan Lu, Jimmy Kan, Eric E. Fullerton, and Zhaowei Liu, "Tunable surface plasmon polaritons in Ag composite films by adding dielectrics or semiconductors." The dissertation author was the first author of this paper.

Chapter 2

Plasmonic metamaterials: tunable plasmonic properties

2.1 Composite metamaterials

To address this limitation of material properties, artificially nanostructured materials often exhibit extraordinary properties not found in nature [32, 33]. Theoretical descriptions and experimental results detailing the optical properties of metal clusters have been extensively discussed as a pathway to modify material properties [32]. Recent investigations on silver-gold clusters reveal that their plasmonic band evolves with the particle size and relative concentrations, which are well predicted by a model based on the time-dependent local-density approximation [34]. The tunability of metal alloys has been utilized to optimize the enhanced emission from semiconductors [35]. Metals mixed with dielectrics provide an alternative route towards engineered SPP properties [36]. It has been proposed that a composite metal-dielectric films enables superlenses working at any desired wavelength with a designed metal filling factor [37]. Efforts have been made to fabricate smooth metal-dielectric nanocomposite films, but their absorption spectra and retrieved material properties do not agree well with effective medium theory [38, 39].

In this section, we describe modifying the optical properties of metals by

adding a small percentage of dielectrics or semiconductors. We have studied Ag films mixed with SiO_2 or Si where the SPPs are excited and measured. Angular-resolved reflection spectra at different wavelengths are obtained in the Fourier space and agreed well with a theoretical model. Effective material properties of such composite films are also derived and discussed.

The optical properties of composite films can be characterized by measuring their angular-resolved reflection spectra at different wavelengths using an oil-immersion optical microscope as illustrated in Figure 2.1. The numerical aperture (NA) of the oil immersion objective is NA = 1.4. Monochromatic waves produced by passing a broadband light source through a series of bandpass optical filters are incident onto the composite film samples from the glass substrate side. A charge coupled device (CCD) camera located at the back-focal plane of the objective lens captures the reflection in the Fourier space. At a certain wave vector, phase matching conditions are satisfied to excite SPPs at the film-air interface by the P-polarized light. This excitation is visualized as a dip in the captured reflection intensity. A linear polarizer is used to filter out the S-polarized component.

The composite films were fabricated by doping a small amount of SiO_2 or Si into pure silver. The Ag-SiO_2 (30 nm thick with 4.7% atom SiO_2) and Ag-Si (40 nm thick with 5% atom Si) composite films were prepared by co-sputtering onto ambient temperature glass substrates from magnetron sputtering sources. Corresponding scanning electron microscope (SEM) images are given in Figures 2.2 (a) and 2.3 (a), respectively. Sputtering rates for DC-sputtered Ag and Si at 50 W were 1.6 Å/s and 0.16 Å/s, respectively. SiO_2 was RF sputtered at 90 W at a rate of 0.17 Å/s. The sputtering rates were determined by low angle x-ray reflectivity measurements of total film thickness versus time. The base pressure of the chamber was $5 \sim 8 \times 10^{-9}$ Torr and the Ar pressure during sputtering was fixed at 2.5 mTorr. Average compositions are determined stoichiometrically based on material deposition rates.

The inset in Figure 2.1 gives a typical reflection intensity profile at the back-focal plane of the microscope (this case $\lambda = 523$ nm). The radius of the reflected intensity disk is limited by the numerical aperture of the oil-immersion objective

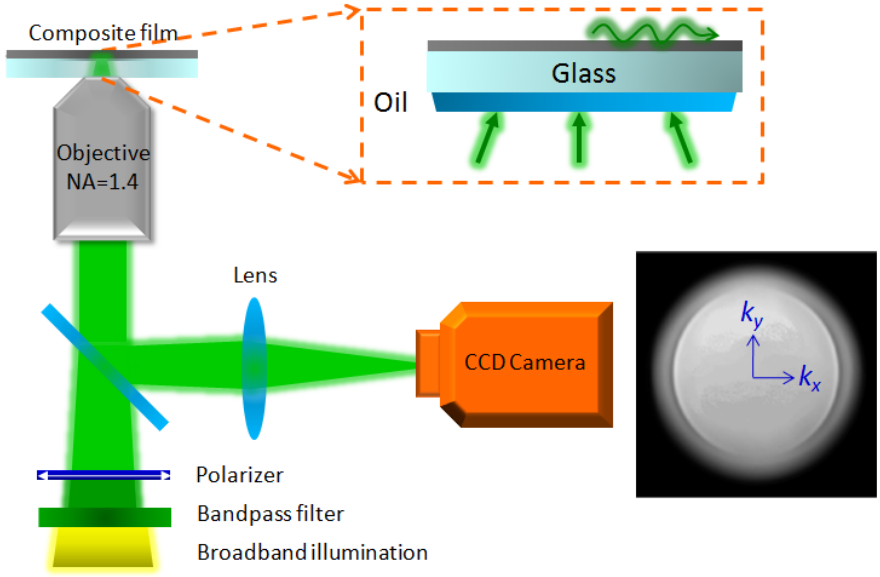

Figure 2.1: Schematic configuration of an oil-immersion optical microscope system for characterizing the SPP properties of composite metamaterial films at different wavelengths. The inset picture gives a typical reflection at the back-focal plane of the system captured by a CCD camera.

corresponding to a free-space wave vector, i.e., NA = 1.4, while the symmetric dark rings inside the bright disk indicates the position of the SPP excitation in the k space. The reflection images at the Fourier plane for different wavelengths across the optical spectrum are taken for both Ag-SiO_2 (Figure 2.2 (b)) and Ag-Si (Figure 2.3 (b)) composite films. After normalized by the corresponding incident light intensity, the reflection spectra are retrieved along the k_x axis for each wavelength. Three experimental curves for the wavelengths $\lambda = 405$ nm, 523 nm and 633 nm obtained following this method are plotted as open symbols in Figures 2.2 (c) and 2.3 (c) for Ag-SiO_2 and Ag-Si composite films, respectively. The intensity peak around k_0 in each curve corresponds to where total internal reflection takes place, while the intensity dip afterwards indicates the excitation of SPPs when the parallel wave vector k_x matches the wave vector of SPP resonances at the film-air interface. Similar to those in pure metals, the SPPs in the composite films shift to higher wave vectors with broadened resonance bandwidths when the incident wavelength blueshifts.

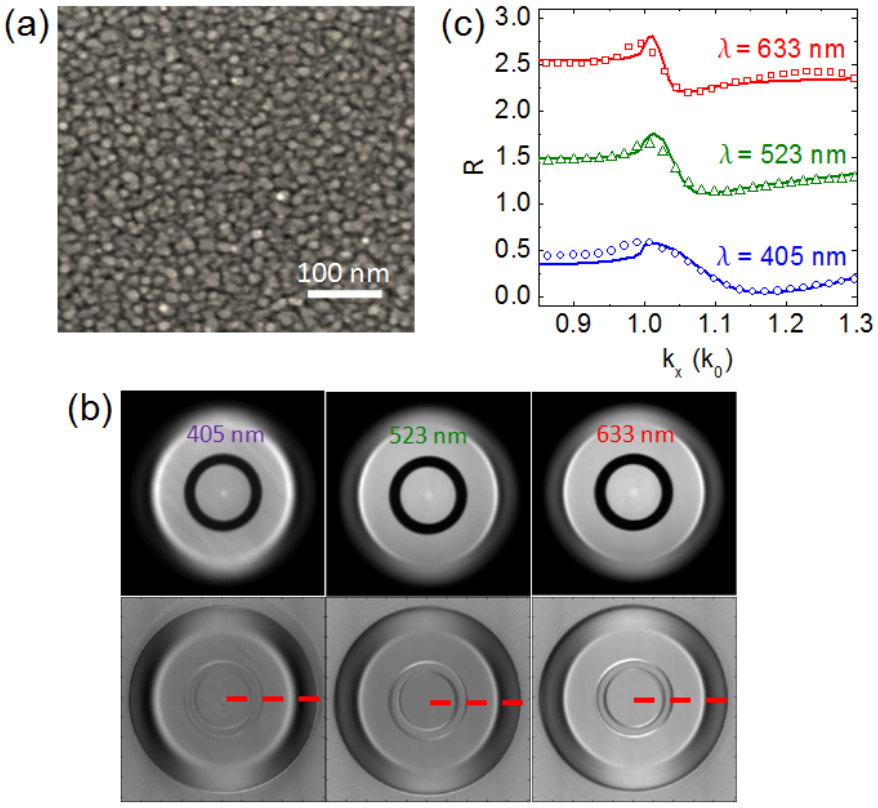

Figure 2.2: Characterization of Ag-SiO_2 composite film. (a) SEM images for the fabricated Ag-SiO_2 composite film of 30 nm thick with 4.7% atom SiO_2; (b) Raw reflection images taken at the Fourier plane for different wavelengths and corresponding images after normalized by the incident light intensity. The reflection spectra are retrieved along the k_x axis for each wavelength as indicated by the dashed red lines; (c) Measured angular-resolved reflection spectra (open circles, open triangles, and open squares) and theoretical fit curves (solid lines) for Ag-SiO_2 at the wavelengths $\lambda = 405$ nm, 523 nm and 633 nm, respectively.

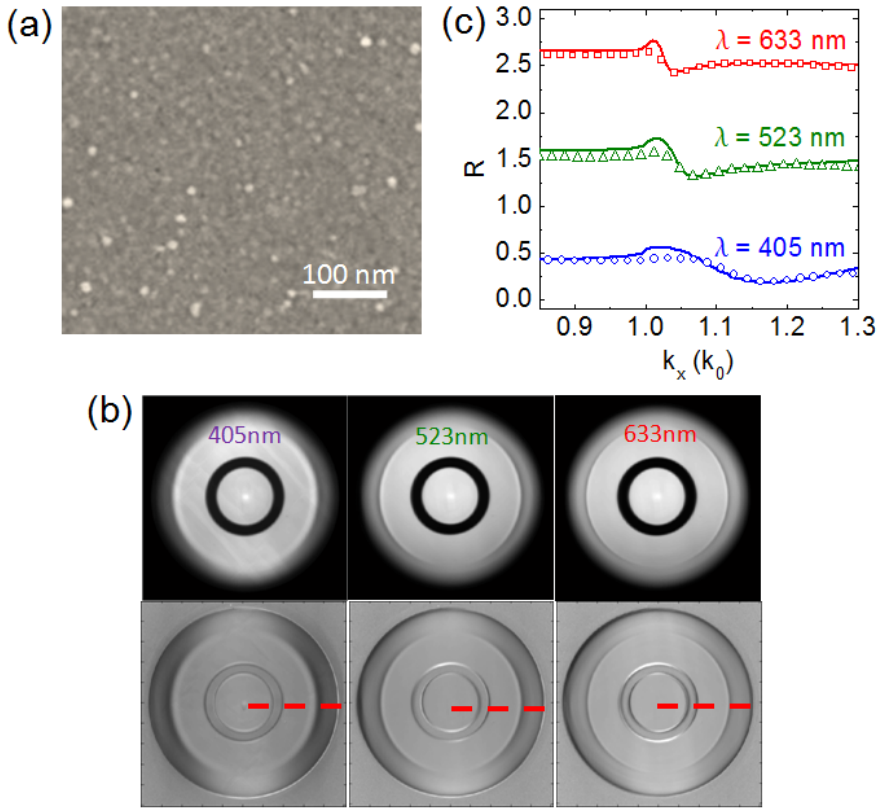

Figure 2.3: Characterization of Ag-Si composite film. (a) SEM images for the fabricated Ag-Si composite film of 40 nm thick with 5% atom Si; (b) Raw reflection images taken at the Fourier plane for different wavelengths and corresponding images after normalized by the incident light intensity. The reflection spectra are retrieved along the k_x axis for each wavelength as indicated by the dashed red lines; (c) Measured angular-resolved reflection spectra (open circles, open triangles, and open squares) and theoretical fit curves (solid lines) for Ag-Si at the wavelengths $\lambda = 405$ nm, 523 nm and 633 nm, respectively.

To get a better understanding of the effective material properties of the metal film after being doped with a small percentage of dielectrics or semiconductors, a simple phenomenological model was investigated to fit the experimental results. The effective dielectric function of the metal-dielectric composites was assumed to follow the Maxwell-Garnett formalism or the Bruggerman mixing theory [37]. In the case of a small fraction of dielectrics, the percolation of metal dominates the optical properties of the composite films. Therefore, we approximate the effective dielectric function $\epsilon_{\text{eff}}(\omega, x)$ for the composite film $\text{Ag}_{1-x}\text{D}_x$ as the volumetric average of the metal Ag and the doping D components [34, 40]:

$$\epsilon_{\text{eff}}(\omega, x) = \epsilon_{\text{Ag}}(\omega) \cdot (1 - x') + \epsilon_{\text{D}}(\omega) \cdot x', \tag{2.1}$$

where D stands for the doped dielectric or semiconductors, whose volume percentage x' can be calculated from its mole fraction x in the composite film as $x' = xV_{\text{D}}/[xV_{\text{D}} + (1-x)V_{\text{Ag}}]$ with V as the volume per mole. The permittivity $\epsilon_{\text{D}}(\omega)$ for SiO_2 and Si are taken from Refs. [41] and [42], respectively. The Drude model is used to characterize the metal Ag in the optical spectral range, $\epsilon_{\text{Ag}}(\omega) = \epsilon_\infty - \omega_{\text{P}}^2/(\omega^2 - i\gamma'\omega)$, where for Ag, the high-frequency permittivity $\epsilon_\infty = 6.0$, the plasma frequency $\omega_{\text{P}} = 1.5 \times 10^{16}$ rad/s obtained by fitting the model to the experimental data taken from Ref. [43], and γ' is the relaxation frequency.

In contrast with the pure metal film, the optical properties of the composite film depend strongly on the details of the nanostructures, especially the critical length scales of the heterogeneities [34]. The relaxation frequency γ' is no longer a constant but depends on the particle or grain size and doped media [39, 44, 45],

$$\gamma' = \gamma + A\frac{v_{\text{F}}}{R}, \tag{2.2}$$

where $\gamma = 7.73 \times 10^{13}$ rad/s is the relaxation frequency for bulk Ag when fitted to the experimental data in Ref. [43], $v_{\text{F}} = 1.39 \times 10^6$ m/s is the Fermi velocity. R corresponds to the averaged particle or grain radius obtained from SEM pictures in Figures 2.2 (a) and 2.3 (a) as $R = 10$ nm and 5 nm for Ag-SiO_2 and Ag-Si composite films, respectively. The characteristic parameter A includes both the quantum size effect in extremely small particles of free surface and the dynamic interface charge transition effect between Ag particles and the embedded dopant

[44], and therefore is used as the only fit parameter in this model to capture the resonance positions and bandwidths of SPPs.

With the effective dielectric functions for the composite films assigned, the multilayer system in the simulation is a composite film sandwiched between two infinite dielectric claddings, glass ($n = 1.5$) and air ($n = 1.0$). The thickness of the composite film is set according to the fabricated samples (30 nm for Ag-SiO_2 and 40 nm for Ag-Si). Reflection spectra for different wavelengths at the glass side are calculated using a transfer matrix method [46]. The simulated reflection curves are plotted as solid lines alongside the experimental data in Figures 2.2 (c) and 2.3 (c). The simulations reproduce the key features of the experimental data, accurately depicting the approximate positions of total internal reflection peaks and SPP resonances. The fit parameter $A = 1.5$ and 0.6 are used for Ag-SiO_2 (Figure 2.2 (c)) and Ag-Si (Figure 2.3 (c)) composite films, respectively. Therefore the relaxation frequency γ' for Ag mixed with a small amount of SiO_2 and Si are found to be 138.73×10^{13} rad/s and 112.53×10^{13} rad/s, respectively, which are about one order of magnitude larger than that for bulk Ag. It thereby indicates a stronger scattering loss in the composite films. By using the modified relaxation frequency, this theoretical model well characterizes the SPP resonances at different wavelengths for both doped samples.

The SPP dispersion relation at the film-air interface can be obtained from the effective dielectric function of the composite film by $k_x = k_0\sqrt{\epsilon_{\text{air}}\epsilon_{\text{eff}}/(\epsilon_{\text{air}} + \epsilon_{\text{eff}})}$. As a comparison, the permittivity for a pure Ag film is also retrieved following the same method. Figure 2.4 shows the dispersion relation for the fabricated Ag-SiO_2 (in red) and Ag-Si (in blue) composite films as well as for the Ag film (in black). The SPP dispersion of Ag film after being doped with a small amount of SiO_2 or Si deviates from that of a pure Ag film. For Ag-SiO_2 composite films, the SP frequency redshifts to $\lambda_{\text{SP}} \sim 385$ nm from originally $\lambda_{\text{SP}} \sim 355$ nm, while for Ag-Si composite films, it goes even further to $\lambda_{\text{SP}} \sim 400$ nm. In principle, larger-percent dopants will enable even larger shifts towards possibly green wavelengths. This designable SPP property opens up the possibility of applications at different wavelengths. In addition, at wavelengths longer than 425 nm, the composite films

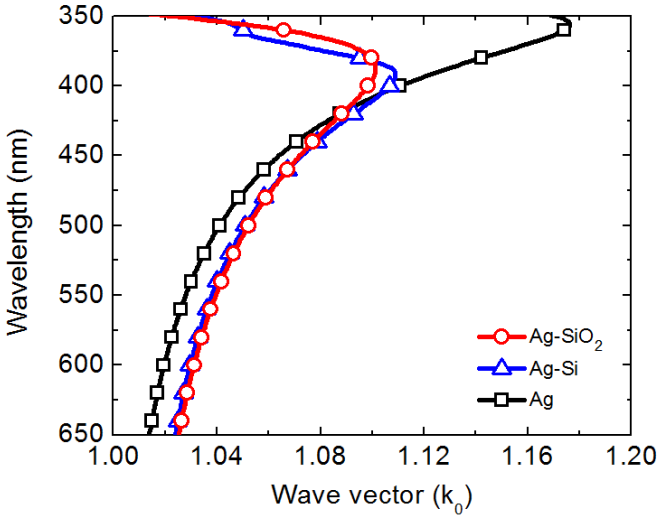

Figure 2.4: SPP dispersion relations for Ag-SiO_2 (red line with open circles) and Ag-Si (blue line with open triangles) composite films. Pure Ag film is present in black line with open squares as a comparison.

have the advantage to provide larger SPP wave vectors than the pure metal film, and therefore a higher EM field confinement is expected.

In the composite film fabrication, the film thickness has been optimized to provide a pronounced measurement. Highly doped composite films produce unidentifiable wide resonances. Losses in such highly doped composite films become pronounced, leading to very wide bandwidths and less conspicuous resonance dips. A potential solution for more flexible tunability of the SPP dispersion in composite films is to investigate binary or ternary alloy systems such as Ag-Au, or Ag-Al.

In summary, by charactering the optical properties of composite films, we demonstrate a promising way to tune the SPP properties of existing metal films by adding additional dielectrics or semiconductors. A phenomenological model that takes into account the filling ratio and particle size effect describes the effective material properties of the measured composite films, and shows their distinct difference from pure metal films.

2.2 Multilayer hyperbolic metamaterials

Although composite metamaterials provide an effective way to tune the SPP resonances, higher loss limits the plasmonic performance and accessibility to large SPP wavevector. An alternative way to modify existing material properties utilizes metal-dielectric based multilayer metamaterials as shown in Figure 2.5 (a). This simplest anisotropic plasmonic metamaterials are made of alternating metal-dielectric layers. When the layer thickness is much smaller than the probing wavelength, an effective-medium approximation is commonly used to describe the effective permittivities along different directions, that is, ϵ_x, ϵ_y and ϵ_z (ref. [47]), following,

$$\epsilon_x = \epsilon_y \equiv \epsilon_{\parallel} = P\epsilon_{\mathrm{m}} + (1-P)\epsilon_{\mathrm{d}}, \tag{2.3}$$

$$\epsilon_z \equiv \epsilon_{\perp} = \epsilon_{\mathrm{m}}\epsilon_{\mathrm{d}} \Big/ \left(P\epsilon_{\mathrm{d}} + (1-P)\epsilon_{\mathrm{m}}\right), \tag{2.4}$$

where $\epsilon_{\parallel}$ describes effective permittivity parallel to the constituent layer and $\epsilon_{\perp}$ corresponds to that perpendicular to the layer; ϵ_{m} and ϵ_{d} are the permittivity for the constituent metal and dielectric, respectively, and P is the volumetric filling ratio of metal.

The equi-frequency contour described by $\frac{k_x^2+k_y^2}{\epsilon_{\perp}} + \frac{k_z^2}{\epsilon_{\parallel}} = \frac{\omega^2}{c^2} = k_0^2$ for a TM-polarized light propagation in the isotropic medium is generally an isotropic sphere as the dashed circle showing the cross section in Figure 2.5 (a). General anisotropic materials, like crystals, will induce anisotropic permittivity along different directions, giving an elliptic equi-frequency contour (Figure 2.5 (a), blue line). Due to the large negative real part in metal permittivity, metal-dielectric multilayer based anisotropic metamaterials can have different signs for $\epsilon_{\parallel}$ and $\epsilon_{\perp}$ under TM wave incidence, resulting in a hyperbolic equi-frequency contour as the red lines shown in Figure 2.5 (a). This type of metamaterials is commonly named as hyperbolic metamaterials (HMMs). Another type of HMMs builds on metallic nanowires embedded in a dielectric host with the effective material properties described by the effective medium theory as,

$$\epsilon_z = P\epsilon_{\mathrm{m}} + (1-P)\epsilon_{\mathrm{d}}, \tag{2.5}$$

$$\epsilon_x = \epsilon_y = \epsilon_{\mathrm{d}} \frac{(1-P)\epsilon_{\mathrm{d}} + (1+P)\epsilon_{\mathrm{m}}}{(1+P)\epsilon_{\mathrm{d}} + (1-P)\epsilon_{\mathrm{m}}}, \tag{2.6}$$

with ϵ_z parallel to and $\epsilon_{x/y}$ perpendicular to the nanowires. These types of HMMs provide high wavevector coverage due to their unbounded dispersion with ultrahigh density of states for unprecedented nanoscale light control. Based on the effective medium theory, the general working wavelength ranges for multilayer and nanowire metamaterials are UV-Red and Green-IR, respectively. In this study, multilayer HMMs will be mainly investigated.

Figure 2.5 (b) presents a typical ω-k dispersion relations for a Ag-Al_2O_3 multilayer HMM with the Ag filling ratio of 0.4. This multilayer HMM has a transmission band at wavelengths less than 410 nm. Three types of dispersion relations are present: Type-I and type-II hyperbolic dispersions exist at wavelength ranges $<$360 nm and $>$410 nm, respectively, whereas elliptic dispersion also displays at the wavelengths 360 nm$\sim$410 nm. Their corresponding equi-frequency contours are shown respectively on the right panel. These dispersion relations and their defining material properties are highly dispersive and strongly depend on the constituting materials, filling ratios and working wavelengths. By changing the Ag filling ratio to 0.5, the transmission band blueshifts in the Ag-Al_2O_3 multilayer HMM accompanied by a dramatic variation in the dispersion relations (Figure 2.5 (c)). A plasmonic-mode merging wavelength was found close to 400 nm, which corresponds to the maximum density-of-state contribution. This plasmonic resonance can be shifted to longer wavelengths for instance 600 nm by switching to different material systems like a Ag-Si multilayer HMM with the same Ag filling ratio 0.5 (Figure 2.5 (d)). By well combined engineering of materials and filling ratios, the working wavelength for multilayer HMMs can be tuned across a broad band of wavelengths.

To demonstrate the tunable plasmonic properties in experiments, metal-dielectric multilayer HMMs were fabricated by alternative deposition of metal and dielectric materials onto different substrates. A series of multilayer samples with different material combinations and component filling ratios were made using either e-beam evaporation or DC magnetron sputtering. Figure 2.6 shows the cross sectional characterization of a few different multilayer HMM samples fabricated by

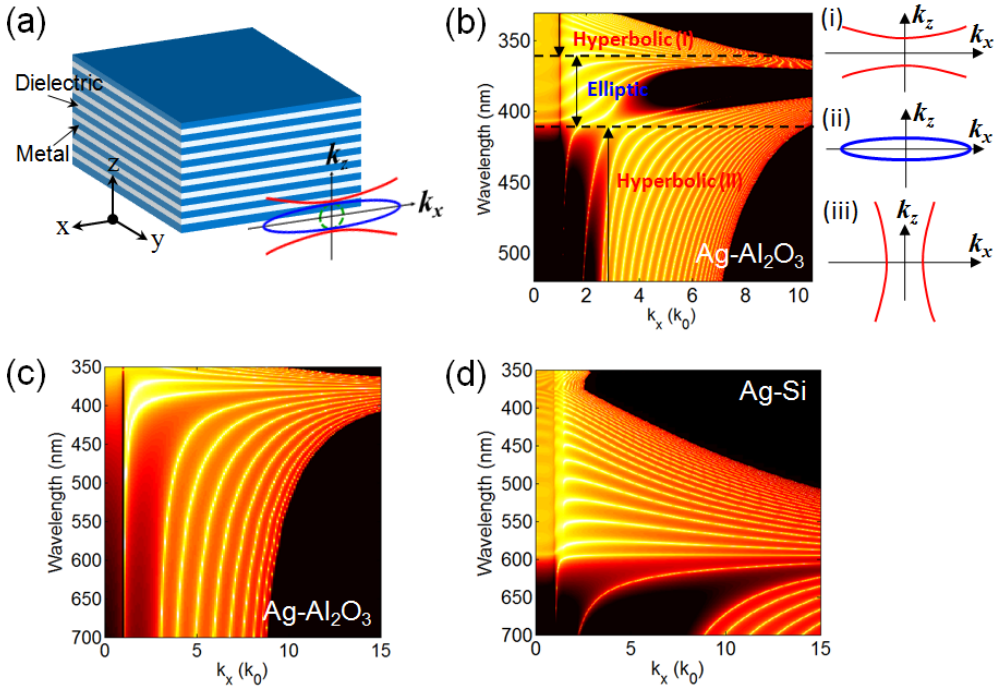

Figure 2.5: (a) Schematic representation of metal-dielectric multilayer metamaterials with different colors representing two constituent materials. The inset shows hyperbolic (in red), elliptic (in blue), and isotropic spherical (in green) equi-frequency contours. (b-d) Dispersion relations calculation for Ag-Al_2O_3 (b, Ag filling ratio 0.4), Ag-Al_2O_3 (c, Ag filling ratio 0.5), and Ag-Si (d, Ag filling ratio 0.5) multilayer metamaterials. The inset in (b) corresponds to type-I hyperbolic (i), elliptic (ii), and type-II hyperbolic (iii) dispersions.

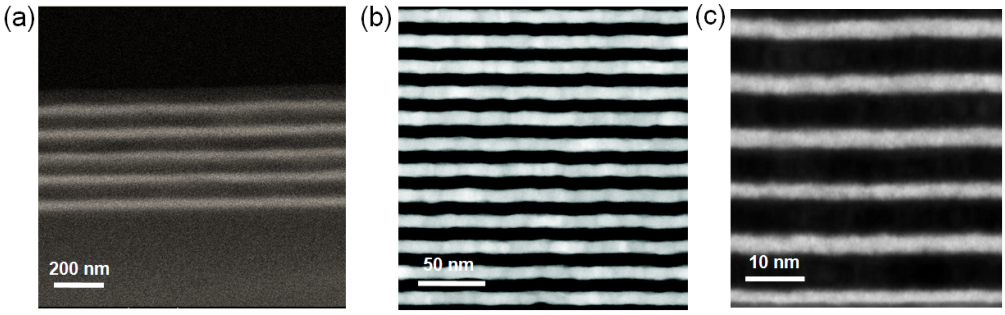

Figure 2.6: Multilayer HMM fabrications. (a) Cross-sectional SEM image of a Ag-Al_2O_3 multilayer with a period of 70 nm and Ag filling ratio 0.5 fabricated by e-beam evaporation process. (b,c) Cross-sectional scanning transmission electron microscopy image of a Ag-Si multilayer with a period of 20 nm and Ag filling ratio of 0.5 (b) and a Au-Si multilayer with a period of 10 nm and Au filling ratio of 0.6 fabricated by a DC magnetron sputtering system.

both approaches. Ag-Al_2O_3 multilayers with a period of 70 nm were fabricated by a e-beam evaporation process as the SEM image shown in Figure 2.6 (a), whereas Ag-Si multilayers with a period of 20 nm and Ag filling ratio of 0.5 and Au-Si multilayers with a period of 10 nm and Au filling ratio of 0.6 were made by a DC sputtering system with the scanning transmission electron microscopy images shown in Figure 2.6 (b) and (c), respectively. These fabricated multilayers have well-formed layered structure, which will be suitable for extensive plasmonic applications. From the fabrication aspect, metal-Si based multilayer system proves relatively better material compatibility than metal-oxide multilayers. A much smaller period of 10 nm was demonstrated here. Also sputtering techniques make much smoother multilayers, and even thinner layers down to 2-3 nm will be expected.

The optical properties of fabricated multilayer samples were characterized by optical transmission measurement in a microspectroscopy system. Figure 2.7 (a) shows the transmission peak at a wavelength 380 nm by a Ag-Al_2O_3 multilayer and the corresponding optical transmission image. The multilayer was made of 5 periods of 70 nm and a Ag filling ratio 0.5. Compared with the violet transmission, Ag-Si multilayers shift the optical transmission to longer wavelengths as shown in Figure 2.7 (b). As the Ag filling ratio decreases from 95% to 70%, transmission through Ag-Si multilayers shifts from the wavelength 460 nm to 550 nm. It well

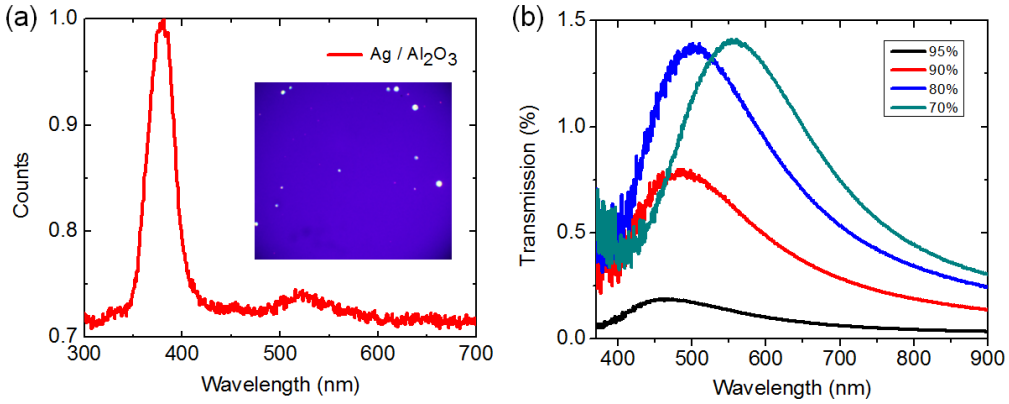

Figure 2.7: Optical characterization of different metal-dielectric multilayer HMMs. (a) Optical transmission measurement of a Ag-Al_2O_3 multilayer HMM. It is made of 5 period of 70 nm Ag-Al_2O_3 with the Ag filling ratio 0.5. The inset shows the optical transmission image through the sample. (b) Optical transmission spectra of Ag-Si multilayer HMMs. They are made of 5 period of 20 nm Ag-Si and a capping Si 5 nm. The Ag filling ratio varies from 95% to 70%.

demonstrates the tunable plasmonic properties in multilayer HMMs by a choice of different material combinations and filling ratios.

To introduce additional degree-of-freedom modification on the plasmonic response from HMMs, these uniform multilayer HMMs can be further nanopatterned by different lithography approaches. Figure 2.8 shows nanopatterned Ag-Si multilayer HMMs by focused ion beam milling (a,b) and reactive ion etching using e-beam lithography patterned Ni as the hard mask (c). Focused ion beam milling provides relatively straightforward technique by directly removing unwanted areas, whereas the dry etching process is more efficient in etching away large areas to leave nanoscale patterns. Both approaches will be good assists for fabricating nanopatterns into multilayer HMMs, leading to extended plasmonic applications such as out-coupling high-wavevector plasmonic modes in light emission control.

2.3 Conclusion

In conclusion, composite metamaterials and multilayer metamaterials were introduced as promising alternatives to existing plasmonic materials for providing tunable plasmonic properties in many applications. We demonstrate tunable SPPs

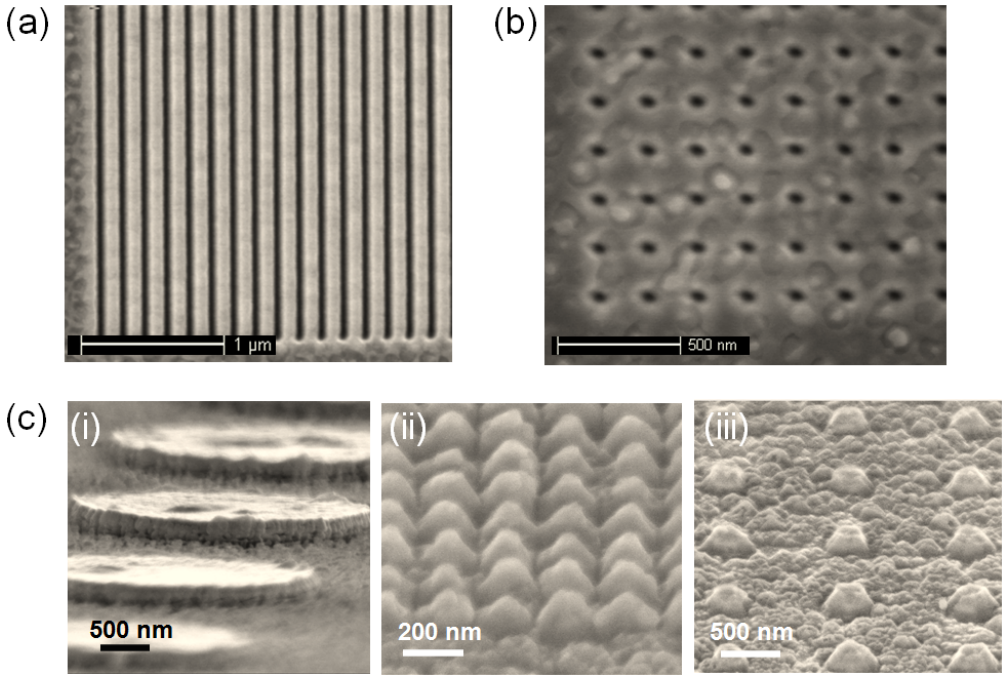

Figure 2.8: Nanopatterning Ag-Si multilayer HMMs. (a,b) SEM images of one-dimensional grating and two-dimensional hole array into the multilayer HMMs made by focused ion beam milling. (c) SEM images at a tilted angle of multilayer nanodisks with microscale diameter (i), a period of 200 nm (ii), and a diameter of 250 nm (iii, separation 1 μm) made by reactive ion etching.

in composite metamaterials by adding additional dielectrics or semiconductors into bulk Ag. On the other hand, the tunability in multilayer metamaterials was enabled by tuning the filling ratio of each component. The ability to construct new material properties paves the way toward various useful applications such as superlens imaging, SPP based sensors, enhanced photoluminescence, and SPP based photovoltaics, etc.

This research is partially supported by the startup fund of the University of California at San Diego and NSF-ECCS under Grant 0969405.

Chapter 2, in part, is a reprint of the material as it appears on Appl. Phys. Lett. 98, 243114 (2011). Dylan Lu, Jimmy Kan, Eric E. Fullerton, and Zhaowei Liu, "Tunable surface plasmon polaritons in Ag composite films by adding dielectrics or semiconductors." The dissertation author was the first author of this paper.

Chapter 2, in part, is being prepared for submission for publication. Dylan Lu, Haoliang Qian, Kangwei Wang, Feifei Wei, Eric E. Fullerton, Paul K. Yu, and Zhaowei Liu, "Multilayer hyperbolic metamaterials speeding up green InGaN/GaN quantum wells (tentative)." The dissertation author was the first author of this paper.

Chapter 3

Multilayer hyperbolic metamaterials for enhancing spontaneous light emission

3.1 Introduction

Recent advances in plasmonics enable the dramatic manipulation of light emitters by controlling radiative intensity or spontaneous recombination rates [48, 3, 49, 50, 13, 51]. Molecular fluorescence enhanced by surface structures improves the sensitivity and detection efficiency for many applications in optical sensing, bio-imaging, and surface enhanced Raman scattering (SERS) [52, 53, 54, 55, 56, 57]. In addition, tailoring spontaneous recombination rates in plasmonic nanostructures is important for high-speed optoelectric devices [13, 51, 58, 59, 60, 61]. These applications increasingly depend on the interaction between light emitters and their local EM environment, known as the Purcell effect [62]. Compared to photonic crystals [59, 60, 61] or high Q-factor cavities [51, 63, 64, 65, 66], spontaneous emission is strongly modified in the vicinity of metal films due to local resonant electric-field enhancement [49, 50]. This approach to control spontaneous emission inherently relies on the alignment of SP resonances with emission wavelengths [67, 68]. However, since plasmonic resonances are mainly determined by the intrinsic

material properties of a metal, the enhancement of spontaneous emission rates usually only works for a few narrow bands of frequencies due to limited available metals in nature.

In contrast to standard metallic materials, metamaterials built by artificial nanoscale structures offer new routes to design material dispersions for potential applications in super-resolution imaging, and multifunctional devices [28, 69, 22]. Multilayer-based anisotropic metamaterials, the most promising optical metamaterials in practice, have recently attracted considerable attention for their designed hyperbolic materials properties [70, 71, 72, 73, 74, 75, 76]. When brought into the near field of the multilayer metamaterials, light emitters decay to the lower-energy level by releasing energy mainly through three channels: radiative emission, plasmonic modes, and other non-radiative decay modes [67, 68]. Since plasmonic modes with high wavevectors dominate over other decay channels [70, 71], HMMs provide larger plasmonic density of states (PDOS) at wavelengths where hyperbolic dispersions are achieved yielding a concomitant enhancement in spontaneous emission rates. More remarkably, this enhancement is broadband and also tunable by simply changing the filling ratio of the constituent materials.

As one implementation of such structures, multilayer-based HMMs have been utilized to control spontaneous emission process, however, only a moderate spontaneous emission-rate enhancement has been observed using uniform multilayer-based HMMs [73, 77, 78, 79, 80]. It is not only due to difficulties in fabricating metal-dielectric multilayers with deep subwavelength periods but also because the dominating plasmonic modes in uniform multilayer metamaterials are usually non-radiative, preventing the detection of large Purcell enhancement in the far field. Therefore, a good out-coupling mechanism is needed to extract the plasmonic modes. Inspired by the work carried out with nanoparticles, plasmonic gratings, and nanoantennas [81, 82, 83, 84, 14, 85, 86], the incorporation of out-coupling nanostructures into HMMs will provide an effective route for engineering better PDOS and enhanced radiative emission simultaneously.

In this chapter, we study nanopatterned multilayer HMMs for controlling the process of light emission, obtaining both strongly enhanced decay rates and im-

proved radiative emission into the far field [87]. The Purcell factor, defined as the ratio of enhanced to free-space spontaneous emission rate [62], is proportional to PDOS, and quantifies the spontaneous emission-rate enhancement in this study. A theoretical model to describe the interaction of dipole emitters with metallic substrates has been extended to multilayer metamaterials, and verified through full-wave EM simulations. We investigate Purcell effect on flat pure metallic films, uniform and nanopatterned metal-dielectric multilayer HMMs as shown in Figure 3.1, and demonstrate tunable Purcell enhancement on HMMs across the visible spectrum by engineering the hyperbolic material properties, which is not possible with fixed plasmonic resonances in pure metals. By analyzing the contribution of three decay channels, we observe that the non-radiative nature of dominating plasmonic-mode component in uniform multilayer HMMs leads to low radiative emission which prevents the observation of strong Purcell effect in the far field. Nanopatterned multilayer HMMs, however, increase radiative emission while keep strong Purcell enhancement through the incorporation of a grating nanostructure that out-couples plasmonic modes. To demonstrate the Purcell enhancement, nanopatterned multilayer HMMs were fabricated by multilayer sputtering and making grating nanostructures into the uniform HMMs, obtaining improved radiative emissions and thus better Purcell-effect detection in the far field. Through a systematic study of the geometrical dependence, a 76-fold spontaneous emission-rate enhancement is observed by time-resolved photoluminescence on the nanopatterned multilayer HMM with a grating period better matching the high-wavevector plasmonic modes, which is close to one order of magnitude faster than on pure Ag with the same out-coupling geometry. About 80-fold emission intensity enhancement is simultaneously achieved in our experiment compared to the case without the out-coupling gratings. The experimental results are quantitatively explained using a dynamic Lorentzian model describing the spontaneous emission processes in the time domain. The promise in achieving light emission with both high decay rates and increased brightness has potential in various plasmonic applications, including light-emitting devices, single-molecule detection, and SERS.

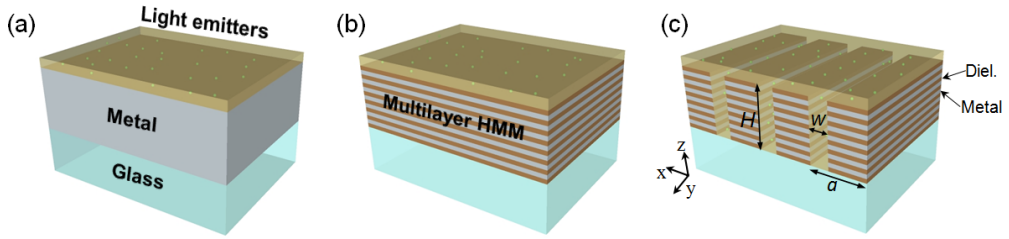

Figure 3.1: Schematics of the light emitter-substrate interaction systems: light emitters embedded in a dielectric medium with a permittivity locate in the vicinity of (a) a metal film, (b) a uniform multilayer HMM, and (c) a nanopatterned multilayer HMM. All the structures are assumed to be on top of glass substrates. The nanopatterned multilayer HMM has period a, nanoslit width w, and height H.

3.2 Theoretical calculation and numerical design of Purcell factor and radiative enhancement

To characterize the interaction between dipole light emitters and plasmonic substrates, we describe the theoretical framework to calculate the quantifying parameters, Purcell factor and radiative enhancement, in the case of dipole emitters on top of metal films [62, 67], and extend the theory to HMM substrates with any number of constituent layers. The study of nanopatterned HMM is carried out by three-dimensional (3D) full-wave EM simulations.

3.2.1 Analytical calculation

Spontaneous emission is not an intrinsic property of dipoles, but subject to their external environment. The probability of spontaneous emission is governed by the Fermi's golden rule [68], $\Gamma_{ij} \sim |M_{ij}|^2 \rho(\hbar\omega)$, where Γ_{ij} is the rate of transition between excited state i and lower-energy state j; M_{ij} is a matrix element that connects these two energy levels; ρ is the PDOS at the transition frequency. Therefore, spontaneous emission can be modified by altering the PDOS as pointed out by Purcell [62]. The ratio of enhanced to free-space spontaneous emission rate is commonly defined as the Purcell factor F.

The decay rate for dipole emitters in free space is given by the Larmor

formula, $\Gamma_0 = |\boldsymbol{\mu}|^2\sqrt{\epsilon_1}\omega^3/3\hbar c^3$, where $\boldsymbol{\mu}$ is the electric dipole moment, ω is the emission angular frequency, and ϵ_1 is the permittivity for the host medium [67]. When a dipole is placed at a distance of d away from a metallic film with a perpendicular ($\perp$) or parallel ($||$) orientation to the interfaces, the corresponding Purcell factors F can be written as [67, 68],

$$F_\perp = 1-\eta_0+\frac{3}{2}\eta_0\mathrm{Re}\int_0^\infty \mathrm{d}k_x \frac{1}{k_z}\left(\frac{k_x}{\sqrt{\epsilon_1}k_0}\right)^3\left[1+r_\mathrm{P}\mathrm{e}^{2ik_zd}\right], \tag{3.1}$$

$$F_{||} = 1-\eta_0+\frac{3}{4}\eta_0\mathrm{Re}\int_0^\infty \mathrm{d}k_x \frac{1}{k_z}\frac{k_x}{\sqrt{\epsilon_1}k_0}\left[1+r_\mathrm{S}\mathrm{e}^{2ik_zd}+\frac{k_z^2}{\epsilon_1 k_0^2}\left(1-r_\mathrm{P}\mathrm{e}^{2ik_zd}\right)\right], \tag{3.2}$$

where η_0 is the internal quantum efficiency of the dipole in free space, which is close to unity for fluorescent molecules like Rhodamine 6G (R6G) and assumed to be unity in the present calculations; k_x (k_z) is the component of the wave vector along x (z) axis while k_0 is the magnitude of the wave vector in vacuum; and $r_{\mathrm{P,S}}$ is the reflection coefficient at the interfaces for P- or S-polarized wave, respectively. For isotropic orientation, the average Purcell enhancement is given by $F_\mathrm{iso} = (1/3)F_\perp + (2/3)F_{||}$ (ref. [68]).

The integrants in equations (3.1) and (3.2) represent the normalized dissipated power spectra of emitters close to a substrate with respect to free space, which describe the distribution of the spontaneous emission rate enhancement or decay channels for different dipole orientations,

$$\frac{\mathrm{d}P_\perp}{\mathrm{d}k_x} = \frac{3}{2}\frac{1}{k_z}\left(\frac{k_x}{\sqrt{\epsilon_1}k_0}\right)^3\left[1+r_\mathrm{P}\mathrm{e}^{2ik_zd}\right], \tag{3.3}$$

$$\frac{\mathrm{d}P_{||}}{\mathrm{d}k_x} = \frac{3}{4}\frac{1}{k_z}\frac{k_x}{\sqrt{\epsilon_1}k_0}\left[1+r_\mathrm{S}\mathrm{e}^{2ik_zd}+\frac{k_z^2}{\epsilon_1 k_0^2}\left(1-r_\mathrm{P}\mathrm{e}^{2ik_zd}\right)\right]. \tag{3.4}$$

Integration of the normalized dissipated power in the range of $0 < k_x < \sqrt{\epsilon_1}k_0$ gives the propagating-wave contribution of spontaneous emission enhancement. For those propagating waves, only emission with $k_x < k_\mathrm{cf}$ is able to escape from the dielectric medium to reach the far field into a certain observation angle. We define the radiative enhancement as the ratio of radiative emission from dipole emitters on the substrates to those in the free space under the same collection angle,

$$f_{\mathrm{rad},\perp/||} = \mathrm{Re}\int_0^{k_\mathrm{cf}} \mathrm{d}k_x \frac{\mathrm{d}P_{\perp/||}}{\mathrm{d}k_x}\Bigg/\int_0^{k_\mathrm{cf}} \mathrm{d}k_x \frac{\mathrm{d}P_0}{\mathrm{d}k_x}, \tag{3.5}$$

where k_{cf} is the cutoff wave vector, and P_0 is the normalized dissipated power for emitters in free space. For isotropic orientation, the average radiative enhancement is given by $f_{\mathrm{rad,iso}} = (1/3)f_{\mathrm{rad},\perp} + (2/3)f_{\mathrm{rad},||}$. With the knowledge of radiative enhancement, the external quantum efficiency (EQE, ref. [88]) enhancement, defined as the ratio of EQE for emitters near the substrates to that in free space, can be obtained as,

$$f_{\eta,\perp/||} = f_{\mathrm{rad},\perp/||}/F_{\perp/||}, \tag{3.6}$$

For isotropic orientation, the average EQE enhancement is given by $f_{\eta,\mathrm{iso}} = (1/3)f_{\eta,\perp} + (2/3)f_{\eta,||}$. In order to apply the above analytical equations to the case of multilayer substrates, the reflection coefficient $r_{\mathrm{P,S}}$ has to be replaced with those for the multilayer interfaces calculated via the transfer matrix method [46, 89]. Consider a scalar wave incident in the negative z direction onto a multilayer substrate of L layers. In the jth layer of thickness l_j and permittivity ϵ_j, the scalar field can be written in the form, $G_j(z) = A_j \mathrm{e}^{ik_{z,j}(z-z_{j-1})} + B_j \mathrm{e}^{-ik_{z,j}(z-z_{j-1})}$, where G represents electrical (magnetic) field for S (P) polarization, z_j is the coordinate of the bottom boundary in the jth layer, and $k_{z,j} = \sqrt{\epsilon_j k_0^2 - k_x^2}$ is the z component of the wave vector in the jth layer. The imposition of the boundary conditions for the EM field leads to the following recursion relation,

$$\begin{pmatrix} A_{j+1} \\ B_{j+1} \end{pmatrix} = \frac{1}{2} \begin{pmatrix} (1+f)\mathrm{e}^{i\phi} & (1-f)\mathrm{e}^{-i\phi} \\ (1-f)\mathrm{e}^{i\phi} & (1+f)\mathrm{e}^{-i\phi} \end{pmatrix} \begin{pmatrix} A_j \\ B_j \end{pmatrix} \equiv T_j \begin{pmatrix} A_j \\ B_j \end{pmatrix}, \tag{3.7}$$

where $\phi = k_{z,j} l_j$, and $f = k_{z,j}/k_{z,j+1}$ for S polarized waves or $f = k_{z,j}\epsilon_{j+1}/(k_{z,j+1}\epsilon_j)$ for P polarized wave. By repeatedly applying the matrix T_j from $j = 0$, the reflection and transmission amplitude r and t can be determined by,

$$\begin{pmatrix} t \\ 0 \end{pmatrix} = \frac{1}{2} \begin{pmatrix} \tau_{11} & \tau_{12} \\ \tau_{21} & \tau_{22} \end{pmatrix} \begin{pmatrix} 1 \\ r \end{pmatrix} \equiv \boldsymbol{\tau} \begin{pmatrix} 1 \\ r \end{pmatrix}, \tag{3.8}$$

where the matrix $\boldsymbol{\tau} = T_L T_{L-1} \cdots T_0$.

3.2.2 3D full-wave simulation

The modified spontaneous emission process through Purcell effect can also be predicted by means of 3D full-wave simulations, performed with the commer-

cial software Comsol Multiphysics^{TM}. To study the emitter-substrate interaction, an electric point dipole is placed in the vicinity of the substrates with the same geometry and permittivity of constituent materials as assumed in theoretical calculations. The total radiated power P_{r}, the power $P_{\mathrm{r,cf}}$ within a certain collection angle into the far field, and the power P_{nr} dissipated due to ohmic loss in the substrate are calculated by integrating power flow through the boundaries [14]. With the knowledge of the total power P_0 and the power $P_{0,\mathrm{cf}}$ within the same collection angle radiated from the same dipole in the absence of any substrate, the Purcell factor, the radiative enhancement, and the EQE enhancement can be determined respectively as,

$$F = 1 - \eta_0 + \eta_0(P_{\mathrm{r}} + P_{\mathrm{nr}})/P_0, \tag{3.9}$$

$$f_{\mathrm{rad}} = P_{\mathrm{r,cf}}/P_{0,\mathrm{cf}}, \tag{3.10}$$

$$f_\eta = f_{\mathrm{rad}}/F. \tag{3.11}$$

This full-wave simulation procedure is not limited to uniform substrates but can be applied to patterned nanostructures with a suitable choice of integration boundaries. While for uniform substrates calculations for dipoles perpendicular and parallet to the interface are sufficient to mimic isotropic dipoles, it is usually required to simulate for dipole orientations along all thress axies x, y and z on nanopatterned structures.

3.2.3 Calculation results of Purcell enhancement

We apply the theoretical framework to study Purcell effect and radiative enhancement in metal-dielectric multilayer HMMs, and compare the results with those obtained from traditional pure metal surface. Full-wave simulations for nanopatterned HHMs show enhancement for both decay rate and radiative emission.

Figure 3.2 shows the calculated dispersion relations and corresponding Purcell factors for conventional plasmonic metallic materials, Ag, Al, and Au. The dispersion relations are calculated for the metal-dielectric interfaces, according to

[4],

$$k_x = \frac{\omega}{c}\sqrt{\frac{\epsilon_{\mathrm{m}}\epsilon_1}{\epsilon_{\mathrm{m}}+\epsilon_1}}, \tag{3.12}$$

where ϵ_{m} and ϵ_1 are frequency-dependent permittivities of the metal and surrounding dielectric materials. The permittivity for Ag is taken from refs. [43] while those for Al and Au from Ref. [41]. The surrounding medium is assumed to have $\epsilon_1 = 2.25$. In the calculations of Purcell factor, the dipole emitter is surrounded by a dielectric medium of the same permittivity $\epsilon_1 = 2.25$ and placed $d = 10$ nm above a 200 nm thick metal on a glass substrate (Figure 3.1 (a)). Purcell factors for isotropic dipoles are obtained by averaging over the results of Equations. (3.1) and (3.2).

For pure metallic substrates, the spontaneous emission decay rate is enhanced when the emission wavelength aligns with the SP resonance. Correspondingly high PDOS at these SP resonances leads to strong Purcell effect. Owing to its superior plasmonic property extended to higher wave vectors, Ag shows a decay rate enhancement of two orders of magnitude at its resonance $\lambda = 360$ nm, which is much higher than the other metals. The plasmonic resonance frequency is determined by the permittivities of both metal and the dielectric, which is limited by the properties of existing materials. For dipole emissions at wavelengths not aligned with the resonances, the Purcell enhancement by using these conventional plasmonic materials diminishes.

As compared with the fixed plasmonic resonances in metals, multilayer-based metamaterials provide the solution for tunable material properties not available in nature. In this section, we will focus our study on a Ag-Si HMM. Figure 3.3 (a) shows the Purcell factors calculated for isotropic dipole emitters in a dielectric medium with $\epsilon_1 = 2.25$ at a distance $d = 10$ nm away from uniform Ag-Si HMMs. In this simulation, the multilayer metamaterial consists of 10 layers of Ag and 11 layers of Si with a period of 20 nm on a glass substrate. The permittivity for Si is taken from refs. [42]. The filling ratio p of Ag varies from 1 to 0.4 with $p = 1$ corresponding to a pure Ag film.

By varying the constituent material filling ratio, Purcell enhancement by Ag-Si multilayer HMMs can be tuned across the visible spectrum with a broader

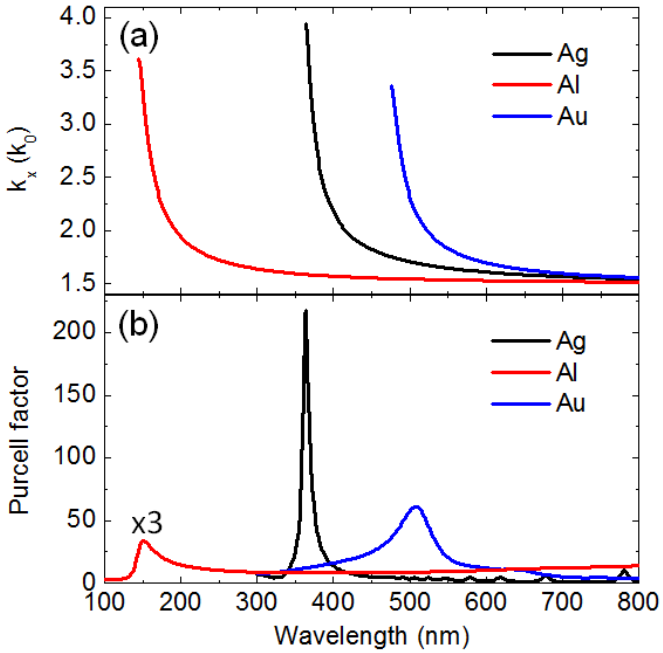

Figure 3.2: (a) Dispersion relations for EM waves at the interfaces between metals, Ag (black), Al (red), and Au (blue), and a dielectric medium with permittivity $\epsilon_1 = 2.25$. (b) Purcell factor calculated for isotropic dipole emitters located a distance of $d = 10$ nm above a 200 nm thick metal of Ag (black), Al (red), and Au (blue) on a glass substrate with a permittivity of 2.25. The magnitude Purcell factor for Al is multiplied by 3 for better display.

bandwidth in contrast with a fixed one by pure Ag film at $\lambda = 360$ nm with a narrow bandwidth of about 10 nm. The tunability in multilayer metamaterials demonstrates engineered material properties and enables optimized alignment of Purcell effect with different emission spectra from molecules or semiconductors for better applications in modification of spontaneous emission process. For instance, the decay rate of spontaneous emission around the wavelength of 580 nm will be enhanced by close to 120 fold for the multilayer HMMs with $p = 0.6$ but less than 5 fold for pure Ag whose SP resonance is far away from the emission wavelength.

At the wavelength of peak Purcell enhancement, dipole emissions on multilayer metamaterials are strongly modified because the extraordinary hyperbolic dispersions in HMMs creates additional high wave-vector modes, leading to increased PDOS at the resonance wavelengths for the spontaneous decay [70, 77]. The inset of Figure 3.3 (a) shows the normalized dissipated power spectrum calculated based on Equation (3.3) for a perpendicular dipole above a multilayer HMM with $p = 0.6$. It represents different decay channels, showing the high wave-vector modes in the multilayer HMM at the resonance wavelength $\lambda = 582$ nm.

In the calculation for multilayers, the first layer interacting with the dipole emitter is set to be Si. Therefore, the peak magnitude of the Purcell factor in multilayer HMMs is lower than that in pure Ag, and further drops at smaller metallic filling ratio as the effective distance between emitters and first Ag layer is enlarged. However, magnitudes of the peak in the Purcell factor similar to that for pure Ag can be achieved by optimizing the thickness of the first layer.

To further understand the Purcell effect in HMMs, we inspect the Ag-Si multilayer HMM with a Ag filling ratio of 0.6 in Figure 3.3 (b-d). Figure 3.3 (b) shows analytical calculations of Purcell factor for dipoles perpendicular and parallel to the multilayer surface whose average gives the result for isotropic dipoles. Perpendicular dipoles display stronger Purcell enhancement than parallel dipoles due to the constructive interference of electric field in the near field of the substrate [68]. On average, namely for isotropic dipoles, a decay-rate enhancement of close to 120 fold is achievable with the multilayer HMM at the wavelength $\lambda = 582$ nm. Such a high Purcell enhancement consists of mainly three contribu-

tions including radiative emission, plasmonic modes, and lossy waves. The latter two components are non-radiative in uniform multilayer HMMs while radiative emission with $k_x < k_{\mathrm{cf}}$ is able to be collected within a corresponding observation angle in the far field. Figure 3.3 (c) depicts the radiative enhancement defined in Equation (3.10) with a cutoff wave vector $k_{\mathrm{cf}} = 0.5k_0$. The radiative enhancement together with the Purcell factor for isotropic dipoles reaches maximum almost at the same wavelength, however, the ratio of the former to the latter, namely the EQE enhancement defined in Equation (3.11), becomes accordingly a minimum as shown in Figure 3.3 (d) since radiative enhancement is still a small portion of the Purcell enhancement. This may prevent the observation of strong Purcell effect in the far field and limit practical applications of such Purcell enhancement. All these analytical results are also well reproduced by those from full-wave simulations as shown in Figure 3.3 in open circles, which confirms the validity of numerical simulations.

To better engineer the radiative emission, a detailed analysis of the contribution from different decay channels will be helpful. The distribution of different decay channels depends on both the emission wavelength and the emitter-metamaterial distance. Figures 3.4 (a-c) show the spectra of radiative emission, plasmonic modes and lossy-wave components as the emitter-metamaterial distance increases from 10 to 100 nm. The radiative emission is obtained by the integration of normalized dissipated power over the wave-vector range of $0 < k_x < \sqrt{\epsilon_1}k_0$. The results indicate that radiative emission from emitters close to the uniform multilayer HMM contributes a small portion of the Purcell effect and barely depends on the distance (Figure 3.4 (d)). Most of the dissipated power goes to plasmonic modes and lossy-wave component, which are non-radiative in uniform multilayer HMM. Since lossy-wave component corresponds to very high wave-vector modes which are inefficiently coupled out and are ultimately lost as heat, plasmonic modes represent the portion potentially capable to contribute to far-field emission. Plasmonic enhancement is mostly confined in space within the short distance of 10$\sim$30 nm from the multilayer HMM surface, and is concentrated close to the resonance wavelength $\lambda = 582$ nm. In order to extract this contribution into the far field for

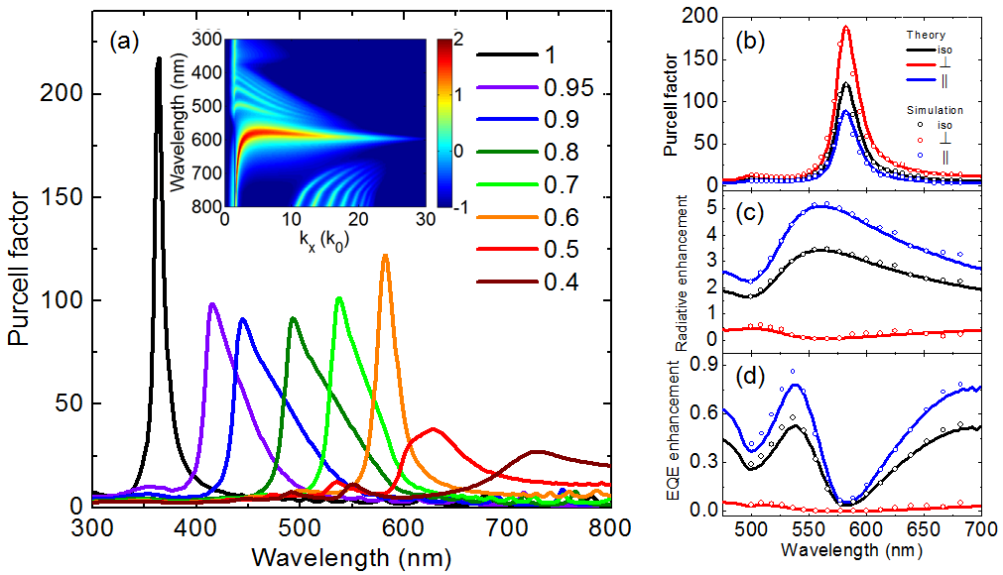

Figure 3.3: (a) Purcell factor for isotropic dipole emitters located at a distance $d = 10$ nm away from the top surface of uniform Ag-Si multilayer HMMs. The multilayers consist of 10 layers of Ag and 11 layers of Si with a period of 20 nm on a glass substrate with a permittivity of 2.25. The filling ratio of Ag varies from 1 to 0.4 as indicated by different colors. The inset shows the normalized dissipated power spectrum with the intensity on a logarithmic scale for a dipole perpendicular to the multilayer HMM with a Ag filling ratio of 0.6. (b) Purcell factor, (c) radiative enhancement, and (d) EQE enhancement for dipoles of the isotropic orientation (iso, black lines), perpendicular ($\perp$, red lines), and parallel ($\parallel$, blue lines) to the uniform multilayer HMM surface in the case of a Ag filling ratio of 0.6. The results of corresponding 3D full-wave simulations in open circles agree with the theoretical calculations.

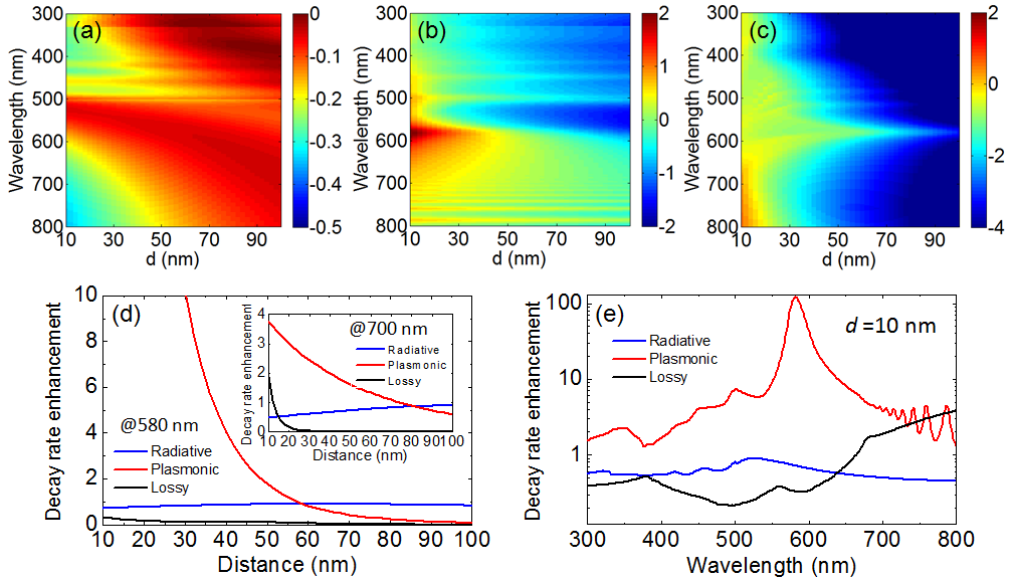

Figure 3.4: (a) Radiative emission, (b) plasmonic modes, and (c) lossy-wave component spectra plotted with the intensity on a logarithmic scale for dipole emitters of isotropic orientation located at a distance of d varying from 10 nm to 100 nm away from the top surface of uniform Ag-Si multilayer HMM. The multilayers consist of 10 layers of Ag and 11 layers of Si with a period of 20 nm on a glass substrate with a permittivity of 2.25. The filling ratio of Ag is 0.6. (d) Three channels of decay rate enhancement as a function of the emitter-metamaterial distance d at the wavelength $\lambda = 582$ nm based on (a-c). The inset shows the same quantities at $\lambda = 700$ nm. (e) Three channels of decay rate enhancement as a function of the emission wavelength at a fixed distance $d = 10$ nm.

enhanced radiative emission, an out-coupling mechanism is needed to compensate for the wave-vector mismatch between plasmonic modes and propagating modes in free space.

The multilayer metamaterial for full-wave simulation study is chosen to be made of Ag-Si stacks with a thickness of 10 nm for each layer and 5 nm of Si capping layer, resulting in a total thickness 305 nm. Figure 3.5 (a) shows the normalized dissipated power spectra for perpendicular dipoles at a distance of $d =$ 10 nm above the Ag-Si multilayers at different emission wavelengths. It presents the k-space power distribution of the spontaneous emission, indicating different decay channels. Components with the wave number less than $\sqrt{\epsilon_1}k_0$ correspond to the power propagating in the surrounding dielectric medium (permittivity =

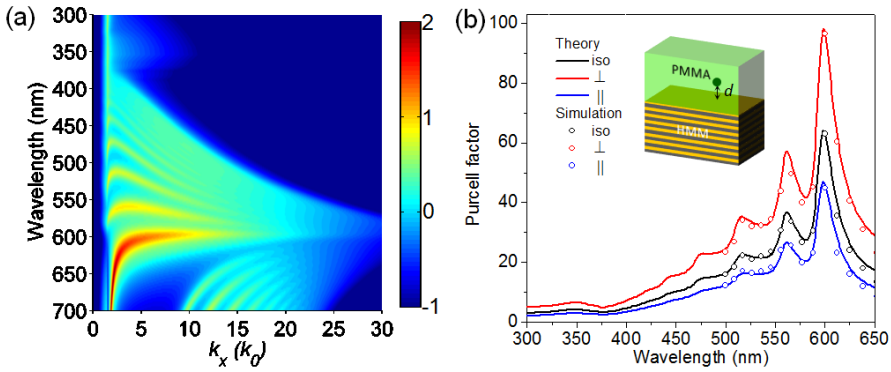

Figure 3.5: (a) Normalized dissipated power spectra with the intensity on a logarithmic scale for a dipole perpendicular to and a distance of $d = 10$ nm above a uniform Ag-Si multilayer with a total thickness of 305 nm. The multilayer has 15 pairs of Ag and Si with each layer thickness of 10 nm. (b) Purcell factor for a dipole located $d = 10$ nm above the uniform Ag-Si multilayer as depicted in the inset. The Purcell factor for isotropic dipoles (iso, black lines) is averaged from that for the dipoles perpendicular ($\perp$, red lines) and parallel ($\parallel$, blue lines) to the surface. Corresponding 3D full-wave simulations in open circles agree with theoretical calculations.

ϵ_1) whereas those larger than $\sqrt{\epsilon_1}k_0$ are dominating non-radiative parts including plasmonic modes. By integrating normalized dissipated power across all wave numbers, the resulting Purcell factor quantifies the spontaneous emission-rate enhancement at different emission wavelengths. The solid lines in Figure 3.5 (b) represent the theoretical calculations of Purcell factor for perpendicular- ($\perp$, red lines) and parallel- ($\parallel$, blue lines) oriented dipoles whose average is for the isotropic ones (iso, black lines). For the Ag-Si multilayer the Purcell factor peaks around $\lambda = 600$ nm with a broad bandwidth of over 60 nm, which aligns better with the emission spectrum of chosen light emitters. The spontaneous emission-rate enhancement is $\sim$60 fold on the Ag-Si multilayer metamaterials as compared with less than 10 fold on the Ag single layer since the emission wavelength is far away from the SP wavelength of Ag. Theoretical calculations are also compared well with 3D full-wave simulations shown as open circles.

We use the full-wave simulation method to study the interaction of dipole emitters with the nanopatterned Ag-Si HMMs. Figures 3.6 (a) and (b) show the calculated cross-sectional mapping of Purcell factor and the enhancement of radia-

tive emission for isotropic dipole emitters placed at different locations on uniform and nanopatterned Ag-Si multilayer HMMs for $\lambda = 600$ nm. Each data point is obtained by averaging the results of dipole orientations along x, y, and z axis. The sweeping length step is 10 nm, and the dipole is kept at least 10 nm away from the surface of the HMM. The collection angle for radiative power is fixed at 23°. Data corresponding to the dashed lines is replotted in Figures 3.6 (c) and (d) for a direct comparison of characteristics on different substrates. The Purcell enhancement for a uniform multilayer HMM is known to decay exponentially as the distance between the dipole and the substrate increases along the z axis. The introduction of nanopatterning in uniform multilayer HMMs leads to new variations in Purcell factor in the x-y plane. The nanopatterned multilayer HMM keeps the similar trend in Purcell enhancement at x-y locations away from the nanoslit, but has weak enhancement close to the nanoslit opening due to effectively larger emitter-metamaterial distances. At dipole locations 1, 2, and 3 (Figure 3.6 (a)), the Purcell factor as a function of the emission wavelength (Figure 3.6 (e)) further illustrates the local PDOS and the spectral similarity between uniform and nanopatterned HMMs, whereas the Purcell enhancement close to the sidewall of the nanoslit shifts to longer wavelengths because of the anisotropic material property of multilayer-based metamaterials.

Thanks to the out-coupling effect of the grating, radiative emission is significantly enhanced on nanopatterned HMMs compared with uniform HMMs as shown in Figure 3.6 (b). The radiative enhancement is defined as the ratio of radiative power from dipole emitters on the substrates to those in free space under the same collection angle. On the uniform multilayer HMM radiative emission is almost invariant to the emitter-metamaterial distance, whereas on the nanopatterned multilayer HMM, it has strong improvement especially close to the surface of the HMMs where higher PDOS is available for out-coupling as indicated in the mapping of Purcell factor in Figure 3.6 (a). At dipole locations 1', 2', and 3', the corresponding spectra of radiative enhancement are also present in Figure 3.6 (f). In comparison with the uniform multilayer HMM, radiative emission on the nanopatterned multilayer HMM gets over 100% improvements at the peak

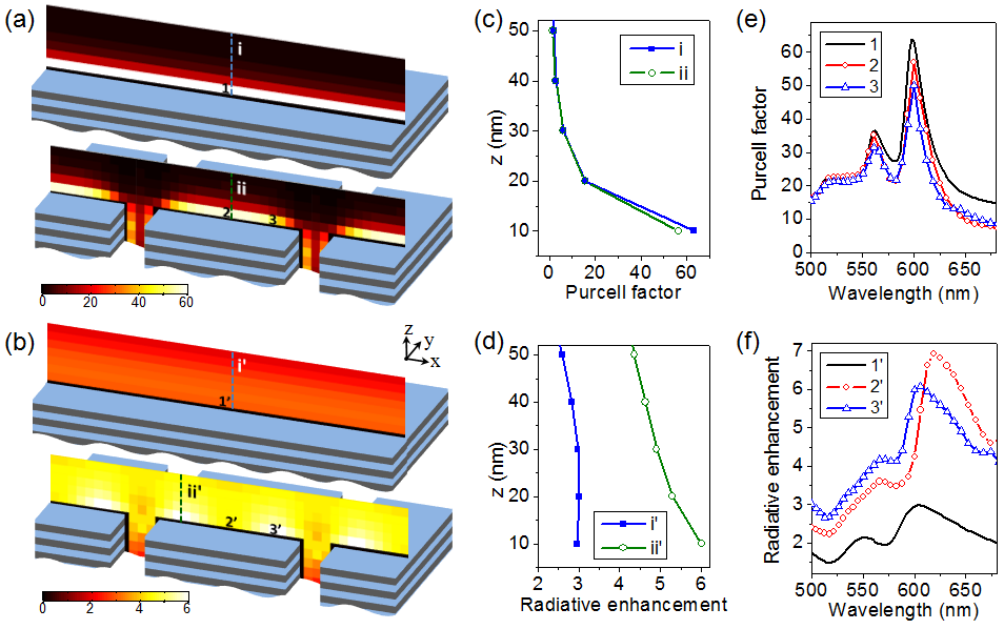

Figure 3.6: Comparison of Purcell enhancement for uniform and nanopatterned multilayer HMMs. Cross-sectional mapping of Purcell factor (a) and radiative enhancement (b) for isotropic dipoles on the uniform and nanopatterned multilayer HMMs at an emission wavelength of 600 nm. The nanopatterned HMM has a grating period of $a = 200$ nm and width of $d = 40$ nm. Color bar in (a) and (b) represents the magnitude of Purcell factor and radiative enhancement, respectively. Purcell factor (c) and radiative enhancement (d) corresponding to the dashed lines in (a) and (b) are replotted for comparison. (e) Purcell factor as a function of emission wavelength for isotropic dipoles at locations indicated in (a). (f) Radiative enhancement as a function of emission wavelength for isotropic dipoles at locations indicated in (b)

wavelength, which will lead to the same improvement for EQE of dipole emitters (see Figure 3.7). Although the magnitude of radiative enhancement is modest in this specific example, a geometry optimization process will provide significant improvements, leading to spontaneous emission enhancement on both decay rates and strong radiative emission.

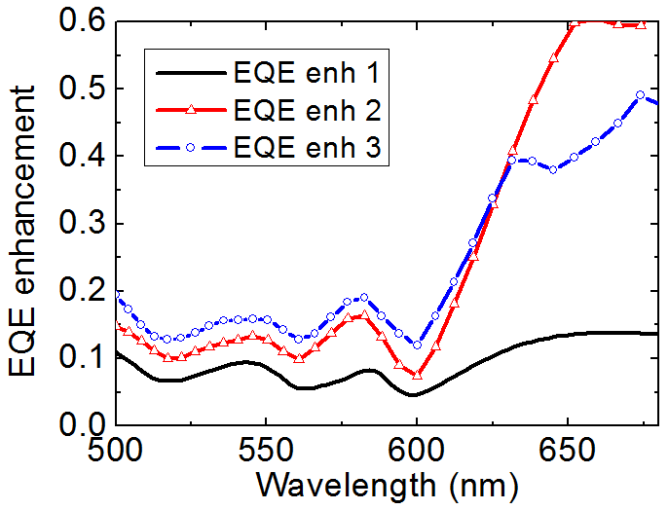

Figure 3.7: Simulated EQE enhancement as a function of the emission wavelength for isotropic dipoles at locations indicated in Figure 3.6. For dipole emitters with high intrinsic internal quantum efficiency, the EQE enhancement becomes a minimum at the peak wavelength of radiative emission since radiative emission is a small portion of the Purcell enhancement. However, nanopatterning helps increase the EQE of dipole emitters placed on the HMMs.

3.3 Fabrication of multilayer hyperbolic metamaterials

To demonstrate Purcell enhancement and radiative emission improvement in experiment, nanopatterned Ag-Si multilayer HMMs were fabricated by a ultra-high vacuum sputtering system and nanopatterning as the schematic configuration shown in Figure 3.8. This multilayer combination was selected based on their material properties in the optical regime and compatibility in film growth. The Ag-Si multilayer HMMs, made of 15 pairs of 10 nm Ag and 10 nm Si layers with a capping Si layer of 5 nm, were prepared by alternatively DC magnetron sputtering Si and Ag layers onto glass substrates at room temperature. Sputtering rates for Ag and Si at 50 W ($\sim$2.5 W/cm^2) were 1.6 Å/s and 0.16 Å/s, respectively, determined by low-angle x-ray reflectivity measurements of calibration sample film thicknesses. The 5 nm capping layer help prevent silver oxidation as well as rapid quenching of emitters in the vicinity of metal surface. The base pressure of the chamber was

5×10^{-8} Torr and the Ar pressure was fixed at 2.0 mTorr. Nanoscale trenches were inscribed into the multilayers by focused ion beam (FIB) with different periods to form grating nanostructures. The gallium ion implantation effect introduced in the FIB milling process is negligible. As a probe, the fluorescence R6G dye molecules mixed in polymethyl methacrylate (PMMA) were spin-coated onto the uniform and nanopatterned surface of the multilayer HMMs. A R6G/PMMA layer with a thickness h =$\sim$80 nm and flat top surface was formed.

A SEM image of one of the fabricated grating nanostructures is shown in Figure 3.8 with the inset image at a titled angle. The individual Si and Ag layers in the multilayers are not visible due to limited resolution in these SEM images. Dark-field scanning transmission electron microscope (STEM) images for the cross-sectional view at different magnifications indicate a well-formed periodic lattice structure in the Ag-Si multilayers with a highly conformal coating across the substrate (Figure 3.8). There is no accumulation of the film roughness throughout the growth direction, and the 10 nm layer thicknesses are well achieved. The element mapping for silicon and silver verifies the multilayer structure and some minor diffusion of Ag into Si (Figure 3.8). The layer thicknesses and multilayer structure were also confirmed by X-ray reflectivity scans.

3.4 Experimental demonstration

3.4.1 Time-resolved photoluminescence

In order to quantitatively identify Purcell effect on the HMMs, the lifetime of R6G dye molecules on various substrates was measured by time-resolved photoluminescence in a two-photon microscope system [90]. A Ti:Sapphire laser system (Spectra-Physics Mai Tai) with a pulse width of less than 100 fs and a repetition rate of 80 MHz was incident to excite R6G, with the excitation wavelength chosen at 800 nm. A dichroic filter (700 nm) was used to block the laser light from the detection. Through an emission filter at 560 nm with a bandwidth of 15 nm, the fluorescence signal was collected by an objective of 20×, numerical aperture (NA) = 0.4 before recorded by a Hamamatsu photomultiplier tube.

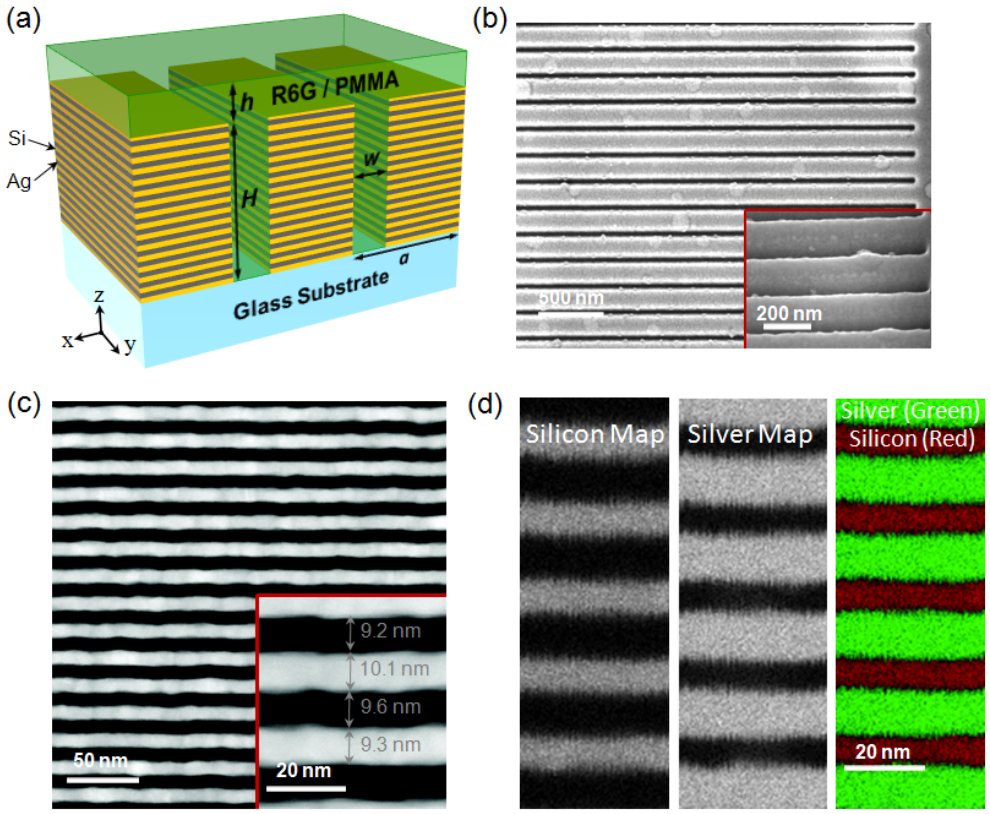

Figure 3.8: Nanopatterned multilayer HMMs. (a) Schematic configuration of nanopatterned multilayer HMMs on a glass substrate. The multilayers consist of Ag-Si stacks (thickness of each layer, 10 nm; total thickness H, 305 nm). Grating patterns with different periods are formed in the multilayers by FIB milling. The R6G dye molecules mixed in PMMA are spin-coated onto the surface to a thickness $h = 80$ nm. (b) SEM image of one of the fabricated nanopatterned HMMs (period $a = 200$ nm; width $w = 40$ nm). Inset: perspective-view SEM image of the grating nanostructure. (c) Dark-field STEM images of the cross-sections of Ag-Si multilayers under different magnifications, showing well-formed periodic lattice structures (each layer thickness, 10 nm). The white colour corresponds to Ag and the black to Si. (d) Element mapping for the constituent materials (Si and Ag), verifying the established multilayer lattice with some minor diffusion of Ag into Si.

Figure 3.9 shows the measured time-resolved fluorescence decay curves in open circles with peaks normalized to one for R6G prepared on both nanopatterned Ag-Si HMM (iv) and Ag grating (ii) substrates. The lifetime of R6G in methanol solution was determined to be 3.8 ns according to the corresponding decay curve in black circles as a reference, which agrees with the typical lifetime of R6G in free space [91]. Compared to the case of R6G in methanol, the decay rate for R6G on the nanopatterned Ag-Si HMM and Ag grating cannot be fitted by a single-exponential function since the detected fluorescence signals come from the collective response of molecules randomly distributed in PMMA. For the nanopatterned Ag-Si HMM substrate with a period of 200 nm, the fluorescence intensity initially decays at a maximum rate of about $1/(0.07 \pm 0.003)$ ns^{-1} by the molecules strongly coupled to the HMM structure before slowing down to a minimum rate of $1/(2.2 \pm 0.3)$ ns^{-1} determined mainly by those away from the HMM. By the same token, for the Ag grating substrate, the decay rates at the maximum and minimum are $1/(0.4 \pm 0.03)$ ns^{-1} and $1/(2.0 \pm 0.1)$ ns^{-1}, respectively (see Figure 3.10). The HMMs with PDOS aligned with the molecular emission spectra further enhance the decay rate by about one order of magnitude compared with the pure Ag gratings (see Figure 3.11 for the comparison with pure Si films). A total 54-fold Purcell enhancement of the decay rate was measured for R6G on the nanopatterned HMM with a period of 200 nm at the emission wavelength.

The measurement results from uniform Ag-Si HMM (iii) and Ag single layer (i) are also presented in Figure 3.9 after divided by the same normalization factor as that on the nanopatterned Ag-Si HMM and Ag grating, respectively. Compared with uniform films, a stronger Purcell enhancement was detected in both the nanopatterned HMM and Ag grating. The grating nanostructures out-couple the dominating plasmonic modes in the HMM for better far-field detection of fast-decaying signals from molecules strongly coupled to the metamaterials. Not only strong Purcell effect becomes accessible in the far field, but the fluorescence intensity is enhanced. A systematic study of the geometrical dependence of decay-rate and intensity enhancement was carried out for nanopatterned HMMs with different grating periods. Figure 3.12 (a) shows measured lifetime of R6G further

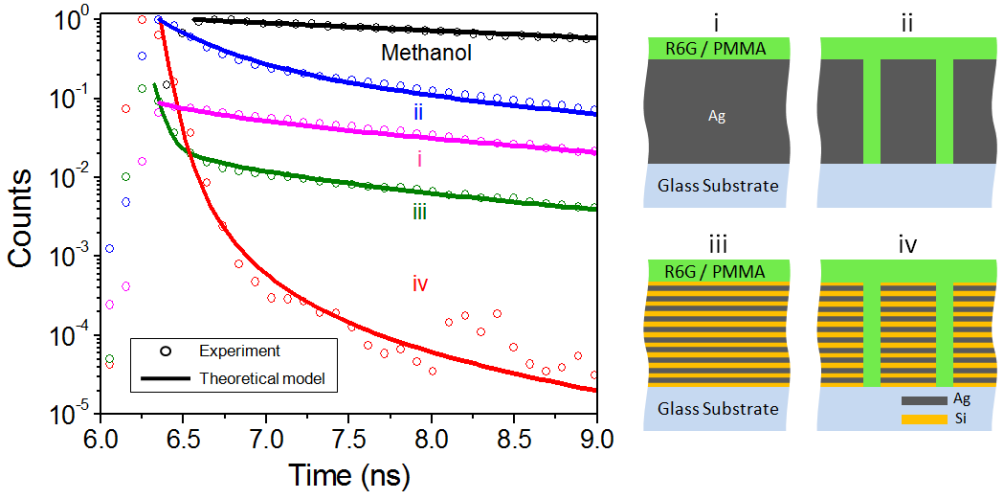

Figure 3.9: Experimental measurements and theoretical fit of time-resolved fluorescence for dye molecules on different plasmonic samples. Time-resolved fluorescence measurements for R6G on the nanopatterned Ag-Si HMM (iv, red open circles), Ag grating (ii, blue open circles) and in methanol solutions (black open circles) after being normalized to the maximum of individual curves observed at an emission wavelength of 560 nm. Grating period, 200 nm. Data for a uniform Ag-Si HMM (iii, green open circles) and a Ag single layer (i, purple open circles) are divided by the same normalization factor as used for the nanopatterned Ag-Si HMM and Ag grating, respectively. Corresponding theoretical fit curves in solid lines explain well the spontaneous emission behaviour in the time domain. Right: schematics of the analysed samples.

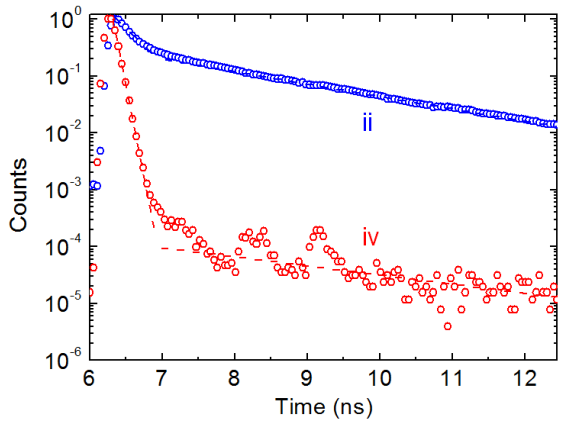

Figure 3.10: Time-resolved fluorescence measurements for R6G on the nanopatterned Ag-Si HMM (iv, red open circles) and Ag grating (ii, blue open circles), replotted from Figure 3.9. The dashed lines fit to the maximum and minimum decay rates of each curve.

decreases as the period of the grating reduces. Corresponding larger Purcell factor results in a total 76-fold decay-rate enhancement for R6G on the nanopatterned HMM with a period of 80 nm. The fluorescence intensity image accumulated for 100 frames at the emission wavelength was also captured on the area with both nanopatterned and uniform Ag-Si HMM regions. The ratio of averaged intensity of the nanopatterned region to the uniform region identifies the fluorescence intensity enhancement (see Figure 3.13). As shown in Figure 3.12, an enhancement factor close to 80 fold was achieved for the nanopatterned HMM with a period of 80 nm as compared with an 8-fold intensity enhancement from larger periods. This intensity enhancement on nanopatterned HMMs comprises contributions from both enhanced radiative emission and enhanced excitation electric field. Smaller grating periods better match and out-couple high-wavevector plasmonic modes, resulting in stronger Purcell and fluorescence intensity enhancement simultaneously. Nevertheless, optimized designs that compensate multiple mismatched wavevectors may further help out-couple more high-wavevector modes.

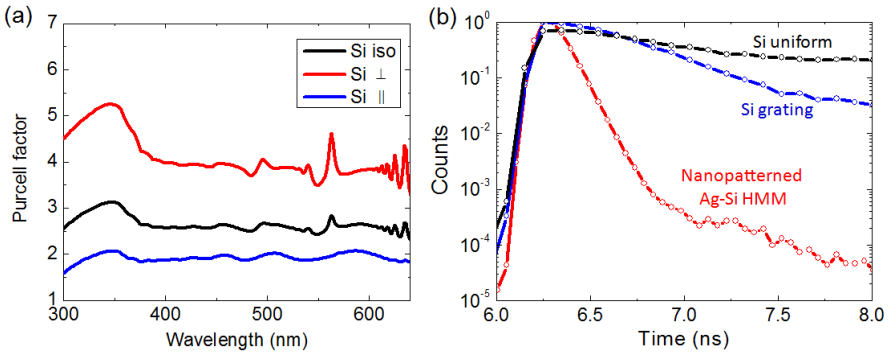

Figure 3.11: (a) Theoretical calculations of Purcell factor for a dipole located $d = 10$ nm above the uniform Si film with a thickness of 305 nm. The Purcell factor for isotropic dipoles (iso, black line) is averaged from that for the dipoles perpendicular ($\perp$, red line) and parallel ($\parallel$, blue line) to the surface. (b) Time-resolved fluorescence measurements for R6G on the uniform Si film (in black) and Si grating with a period of 200 nm (in blue). The data for nanopatterned Ag-Si HMM (in red) from Figure 3.9 is also included for comparison. It indicates Purcell enhancement in pure silicon is only about 3 fold on uniform film and 9 fold on nanopatterned film since no plasmonic modes are excited.

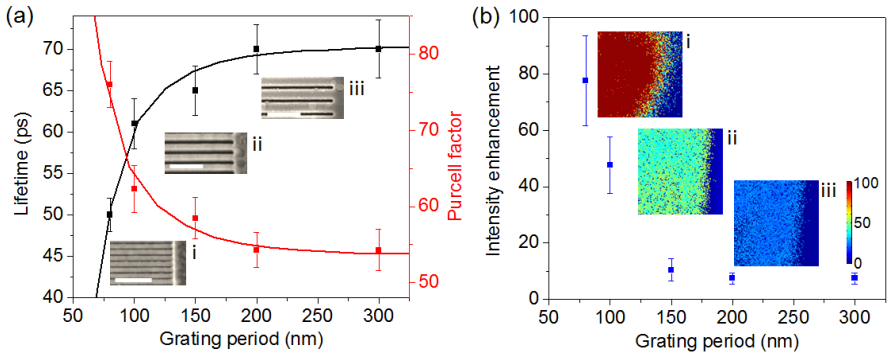

Figure 3.12: Experimental demonstration of the geometrical dependence of Purcell and fluorescence intensity enhancement on nanopatterned HMMs. (a) Lifetime measured at the maximum decay rate of time-resolved fluorescence with the corresponding Purcell factor for R6G on the nanopatterned Ag-Si HMM with different grating periods. The inset shows SEM images of the measured structures (i: $a =$ 80 nm; ii: $a = 150$ nm; iii: $a = 200$ nm).. Scale bar, 500 nm. Solid lines are a guide to the eye. (b) Fluorescence intensity enhancement for R6G on the nanopatterned Ag-Si HMM with different grating periods. Inset: optical images of the fluorescence intensity accumulated over 100 frames (grating periods: $a = 80$ nm (i); $a =$ 100 nm (ii); $a = 200$ nm (iii)).

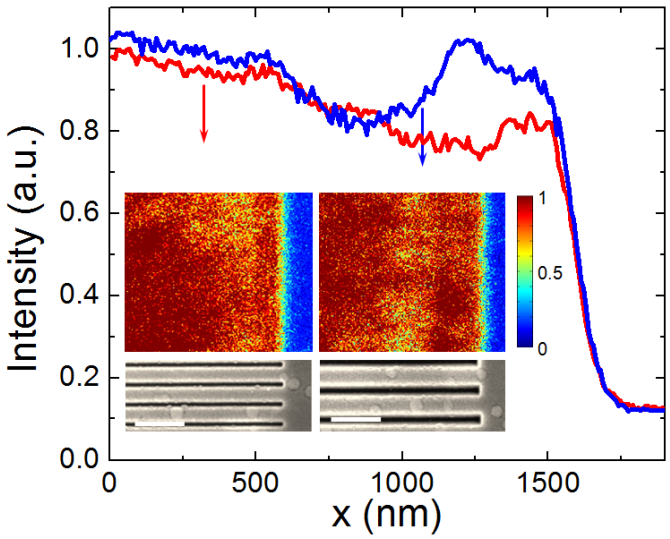

Figure 3.13: Averaged fluorescence intensity as a function of the location along the x axis across the regions of nanopatterned and uniform Ag-Si HMMs separated at $x = 1500$ nm. Measurements shown here were carried out for nanopatterned HMMs with two grating periods of 200 nm and 300 nm. The inset shows the corresponding optical images of the fluorescence intensity accumulated for 400 frames and SEM images of the measured structures. Scale bar, 500 nm.

3.4.2 Modeling of time-resolved spontaneous emission

In order to understand Purcell enhancement and the out-coupling effect in the nanopatterned multilayer HMMs, we adopted a dynamic Lorentzian model [92] to explain the spontaneous emission behavior in the time domain. Emissions from a dipole in the frequency domain is approximated by a Lorentzian shape as, $E_i(\omega) = \alpha_i / (1 - i2(\omega - \omega_i)/\Gamma_i)$, where α_i and ω_i are the emission amplitude and central angular frequency, respectively. Γ_i is the full width at half maximum of the emission spectrum determined by the spontaneous emission rate of a dipole at a specific spatial location on the substrate. Time-resolved spontaneous emission intensity for an ensemble of dipoles on the substrate is calculated by a Fourier transform, resulting in a dynamic Lorentzian model,

$$I(t) = \left| \sum_{i=1}^{N} \left(\left(\alpha_{\mathrm{r},i} + C \cdot \alpha_{\mathrm{PM,i}} \right) \exp\left(-\frac{\Gamma_i}{2} t - i\omega_i t \right) \frac{\Gamma_i}{2} \right) \right|^2, \tag{3.13}$$

where the summation is over the dipole molecules randomly distributed in space on the substrates with a band of emission wavelengths. The emission amplitude is

composed of both a radiative component α_{r} and an out-coupled plasmonic-mode (PM) component α_{PM}, i.e., $\alpha_i = \alpha_{\mathrm{r},i} + C \cdot \alpha_{\mathrm{PM,i}}$, with each component retrieved from the normalized dissipated power spectra. C is the effective out-coupling coefficient for those plasmonic modes when nanostructures are incorporated into the flat substrate. In the approximation of narrow frequency bands and short time range, the effective out-coupling coefficient is defined as,

$$C = \frac{\sum_{i=1}^{N}\left(C_i \cdot \alpha_{\mathrm{PM,i}} \exp\left(-\frac{\Gamma_i}{2}t\right)\frac{\Gamma_i}{2}\right)}{\sum_{i=1}^{N}\left(\alpha_{\mathrm{PM,i}} \exp\left(-\frac{\Gamma_i}{2}t\right)\frac{\Gamma_i}{2}\right)} \approx \frac{\sum_{i=1}^{N}\left(C_i \cdot \alpha_{\mathrm{PM,i}}\frac{\Gamma_i}{2}\right)}{\sum_{i=1}^{N}\left(\alpha_{\mathrm{PM,i}}\frac{\Gamma_i}{2}\right)}, \tag{3.14}$$

where C_i is the spatially dependent out-coupling coefficient. Therefore C is effectively an averaged out-coupling coefficient which is independent of space locations, serving as the only adjusting parameters in this model. More accurate calculation for the emission amplitude can be obtained by the 3D full-wave simulations. When given the spatial distribution of dipole emitters and their individual radiated power, no adjustable parameters will be needed in this model. Nevertheless, the use of an effective out-coupling coefficient spares time-consuming 3D numerical mapping without losing the essence of the underlying physics. By using such an effective parameter, our model not only agrees with the experimental results very well but also provides a straightforward guideline for the future plasmonic-structure optimizations.

Compared with $C = 0$ for uniform films, the fit parameter C is 0.15 ± 0.03 and 0.3 ± 0.05 for the pure Ag grating and nanopatterned multilayer HMM, respectively. In the fitting process, the starting time point and maximum photon counts were obtained from the experimental results. For each dipole at a specific spatial location, its radiative component $\alpha_{\mathrm{r},i}$, PM component $\alpha_{\mathrm{PM},i}$, and spontaneous emission rate Γ_i are rigorously calculated according to the previous sections. The dipoles are assumed to be evenly distributed in space. Therefore the summation includes responses from all dipoles evenly distributed within the PMMA layer. By incorporating the out-coupling coefficient, this model provides a simple theoretical description of the dynamic spontaneous emission behavior.

The theoretical fit based on Equation (3.13) is given in solid lines in Figure

3.9, which agrees well with experimental measurements. Since Purcell enhancement depends on the dipole-substrate distance, time-resolved fluorescence measures an averaged effect from molecules distributed within a PMMA layer thickness. The theoretical model takes this into account by averaging the time response of the dipoles at different spatial locations. The model not only predicts the change of spontaneous emission rates at different time phases determined by the interaction strength of molecules to the substrate but also explains the out-coupling mechanism that helps improved the radiative emission for better identification of the Purcell enhancement of the system.

3.5 Discussion

In our calculations, the distance between dipole emitters and substrates is kept larger than 10 nm. In the regime of smaller distances, the classical theoretical model fails, and a nonlocal or quantum description of the interaction process has to be adopted [67]. At a distance of a few nanometers, Purcell factor will be dramatically enhanced up to a couple of thousands. However, most of dissipated power would be channeled into lossy waves or other non-radiative decay routes which are inefficiently coupled out. Such high Purcell enhancement would therefore lead only to a diminished EQE, without benefiting far-field radiative emission. So, we focus exclusively the classical regime where plasmonic modes dominate.

Our results indicate that at the wavelength of peak Purcell enhancement the EQE for dipole emitters on the metamaterial substrate is always smaller than that in free space since the intrinsic internal quantum efficiency of the emitters is close to unity. A large EQE enhancement is possible only when the internal quantum efficiency of quantum emitters is low. However, according to Equations. (3.1) and (3.2) this would cause a concomitant drop in the Purcell factor. Therefore, in order to utilize the Purcell effect, quantum emitters with high quantum efficiency are needed. Despite of low EQE enhancement, radiative emission into the far field can be enhanced.

We made use of a grating nanostructured HMMs to extract plasmonic

modes into the far field. The possible out-coupling structures are not limited to one-dimensional geometries, but can include for instance two-dimensional hole arrays or bowtie antennas [14]. The ultimate brightness of emitters on the HMM substrates is not only determined by the radiative enhancement but also absorption enhancement if an optical excitation is used. Hence, design procedures combining enhanced electrical field intensity at the absorption wavelength and enhanced radiation at the emission wavelength are needed.

3.6 Conclusion

In conclusion, we propose and study the nanopatterned Ag-Si multilayer HMM to control the spontaneous emission by engineering the PDOS and out-coupling plasmonic modes. The theoretical model for the interaction of dipoles with flat metallic substrates was extended to study Purcell effect on the uniform and nanopatterned HMM substrates. Purcell factor calculations indicate that the enhancement from the multilayer-based metamaterials can be well tuned to desired wavelengths with much broader bandwidths than from pure metal structures. By utilizing an out-coupling mechanism, the dominating plasmonic modes in the HMMs contribute to the increased radiative emission for far-field detection of strong Purcell effect. Time-resolved fluorescence measurements show a 76-fold spontaneous emission-rate enhancement and 80-fold emission intensity improvement from the nanopatterned HMM. The theory, based on a dynamic Lorentzian model, explains both the spontaneous emission decay in the time domain on different substrates and the out-coupling effect by nanostructures for radiative enhancement. By optimizing the distribution of dipole emitters and the design of out-coupling nanostructures, multilayer-based metamaterials can provide more tunability than conventional materials for achieving light emission with both high speed and large radiative intensity at broadband operational frequencies. The HMMs with engineered PDOS will find potential applications in high-speed and high-efficiency bio-sensing, SERS, and light-emitting devices.

This work was supported by ONR Young Investigator Award (no. N00014-

13-1-0535), NSF-ECCS (grant no. 0969405) and NSF-CMMI (grant no. 1120795). The authors thank P. Zhang for help with STEM characterization and M. Digman, E. Gratton, L. Feng, H. Chen and Y. Liu for assistance during various phases of simulations and experiments.

Chapter 3, in part, is a reprint of the material as it appears on Nature Nanotech. 9, 48-53 (2014). Dylan Lu, Jimmy J. Kan, Eric E. Fullerton, and Zhaowei Liu, "Enhancing spontaneous emission rates of molecules using nanopatterned multilayer hyperbolic metamaterials." The dissertation author was the first author of this paper.

Chapter 3, in part, is being prepared for submission for publication. Dylan Lu, Lorenzo Ferrari, Jimmy J. Kan, Eric E. Fullerton, and Zhaowei Liu, "Nanopatterned multilayer hyperbolic metamaterials for spontaneous light emission control." The dissertation author was the first author of this paper.

Chapter 4

Plasmonic metamaterials for improving quantum-well light emitting devices

4.1 Introduction

We have shown in the previous chapter the tunable Purcell effect by multilayer based plasmonic metamaterials for enhancing the spontaneous emission rate of molecules. The concept of manipulating spontaneous emission process by plasmonic metamaterials has much wider possible applications and can be extended to another quantum emitter, the quantum well (QW) system, for improving the light intensity and speed of conventional light-emitting devices (LEDs).

LED has been an active research field for a few decades since its first demonstration in semiconductor lasers in 1962 [93, 94]. Modern LEDs are now available in a variety of colors from UV to infrared for a wide range of applications. The external quantum efficiency (EQE) and the light emission speed are two most important indicators for competitive LEDs. The EQE (η_{e}) value of LED, which determines the brightness, is given by a product of the light extraction efficiency (C_{ext}) and the internal quantum efficiency (IQE, η_i): $\eta_{\mathrm{e}} = \eta_i C_{\mathrm{ext}}$. The η_i is governed by $\eta_i = \tau/\tau_{\mathrm{r}} = \tau_{\mathrm{nr}}/(\tau_{\mathrm{r}} + \tau_{\mathrm{nr}})$, where τ_{r} and τ_{nr} are the radiative and nonradiative life-

times, respectively, and $1/\tau = 1/\tau_{\rm r} + 1/\tau_{\rm nr}$. The effort to improve the performance of LEDs is concentrated to increase $\eta_{\rm e}$ and to reduce $\tau_{\rm r}$ [88].

In order to improve the EQE of LEDs, high internal efficiency designs and high extraction efficiency structures have been adopted. High internal efficiency LEDs are mainly achieved through enhancing the radiative recombination probability or decreasing the non-radiative recombination probability. Growing LEDs with double heterostrucctres leads to higher free-carrier concentration for improved radiative rates. QWs with high crystal quality eliminate deep levels caused by defects, which helps reduce non-radiative recombination. On the other hand, owing to the high refractive index of grown QW semiconductor materials, a certain portion of light emission from QWs will be trapped and reabsorbed in the LEDs. To improve light extraction efficiency, several approaches have been used including shaping LED dies into pedestal or truncated inverted pyramid, introducing surface textures, and combining anti-refection coatings [88]. Similar functionality for EQE improvement has also been demonstrated by nanostructured plasmonic materials [13, 95].

Conventional LEDs have a maximum modulation speed of about a few hundred MHz [96]. There are mainly two approaches to improve the speed of a LED [88]. The first approach consists of introducing a larger carrier concentration in the active region. In a III-V device, the carrier radiative lifetime can be reduced to $\sim$100 ps ($\sim$1.6 GHz) by using a heavily doped ($\sim 10^{19}$ cm^{-3}) active region. Increasing the dopant concentration further commonly leads to severe reduction of internal efficiency. Therefore, to reach higher speeds beyond the 2 GHz limit, the second approach to improve the recombination rate through the Purcell effect should be utilized. As pointed out by Purcell, spontaneous emission may be enhanced by altering the PDOS. The ratio of enhanced to free space emission is commonly called the Purcell factor F. The Purcell enhancement has recently become the key method to modify the spontaneous emission rate, leading to both high speed and high efficiency in plasmonic enhanced LEDs [13, 97, 98, 99, 100, 101]. The degree of spontaneous emission rate modification (or Purcell factor) for a given wavelength depends on the corresponding SPP DOS of commonly used metals.

Therefore, the strongest enhancement occurs near the asymptotic limit of the SPP dispersion branch, where the DOS is maximized. However, common plasmonic materials, such as Ag, barely interact with LED emitting at other wavelengths than the SP resonances, such as green LEDs. The wavelength misalignment between the SP enhancement and the LED emission is one of the most significant yet to be solved challenges in existing plasmonic LEDs. Therefore, we can replace the single metal layer by nanopatterned multilayer plasmonic metamaterials to drastically improve the performance of LEDs in both intensity and speed at desired working wavelengths.

In this chapter, we study and experimentally demonstrate the spontaneous emission intensity and rate enhancement of InGaN/GaN QW-based LEDs by tunable Purcell effect on nanopatterned plasmonic metamaterials. The concept of light emitting enhancement by plasmonic metamaterials will be introduced, and numerical design of plasmonic structures aiming for blue and green light emitting wavelengths details such enhancement dependence on plasmonic materials and nanostructure geometry. In experiments, InGaN/GaN multi-QW LEDs were fabricated for both blue and green emissions. Ag-based plasmonic structures were incorporated into blue LEDs and the strongly improved light emitting intensity was optically characterized. Ag-Si multilayer HMMs were nanopatterned onto the green QWs and time-resolved photoluminescence measurement quantifies close to 60-fold spontaneous emission rate enhancement corresponding to potentially a 3 dB modulation speed of $\sim$9.3 GHz.

4.2 Concept of plasmonic metamaterial enhanced QW LEDs

Figure 4.1 shows schematic configuration of QW-based LED enhancement by placing nanopatterned plasmonic metamaterials close to the vicinity of the active emitting layer. The active emitting layer consists of three multi-QWs with a total thickness of 36-40 nm, and keeps a distance of 10 nm away from the plasmonic structures. The strong interaction between QWs and their nearby plasmonic

materials excites SPPs, and as the emission wavelength approaches the SPP resonance of the plasmonic structures, large DOS becomes available and corresponding dramatic Purcell enhancement of the light emission process is expected.

A theoretical calculation of the Purcell factor based on the modified theory of dipole interaction with metallic substrates as introduced in Chapter 3.2 was carried out for the QW system by modeling the spontaneous emission from QWs as individual dipoles. Figure 4.1 (c) shows the calculated Purcell factor of a dipole emitter at a distance of 10 nm away from the uniform Ag-Si multilayer HMMs. The HMMs consist of Ag-Si multilayers with a thickness period of 20 nm and the bottom layer to be Si closest to the QW emitters. Surrounding medium for the QW emitters was chosen to be GaN, with the permittivity properties taken from [102]. And the internal quantum efficiency for the QW emitters was assumed to be 50%. Resulting Purcell factor gradually blue shifts as the Ag filling ratio in the Ag-Si HMMs increases from 0.6 to 1 with the filling ratio 1 corresponding to a pure Ag film, demonstrating the tunability in such multilayer based HMMs in the application of LEDs. The absolute magnitude also increases with larger Ag filling ratio since the effective distance between dipole emitters and the first Ag layer is reduced.

Based on this theoretical estimation, for a QW LED emitting at violet and blue wavelengths, plasmonic metamaterials using pure Ag provide sufficient Purcell enhancement with the maximum of close to 90 fold and easier practical fabrication and integration. Whereas, for a QW LED emitting at longer wavelengths, for example, green wavelength 530 nm, pure Ag based plasmonic metamaterials no longer support strong local SPP field enhancement, and have to be replaced by Ag-Si multilayer HMMs. Multilayer HMMs demonstrate a close to 50-fold spontaneous emission rate enhancement compared with less than 5 fold by pure Ag plasmonic metamaterials. In order to improve the emission intensity at the same time, nanopatterned structure will be made into these two types of plasmonic metamaterials. As shown in Figure 4.1 (a,b), a simple out-coupling geometry – a periodic nanodisk array – was utilized in this investigation.

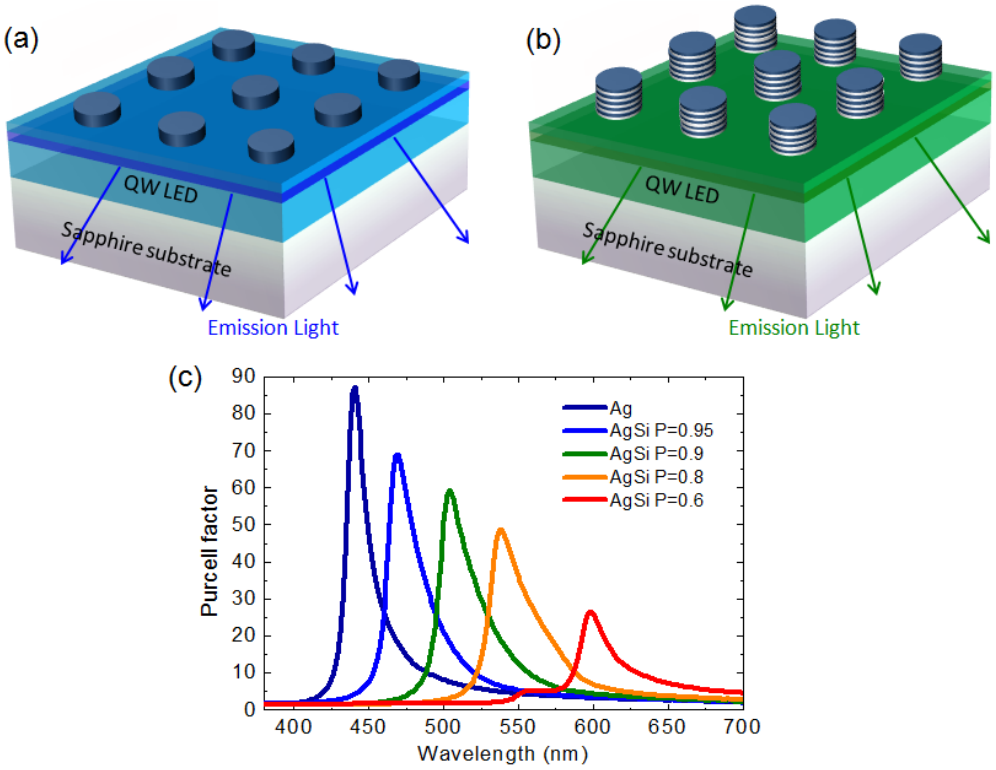

Figure 4.1: Plasmonic metamaterials for enhancing QW LEDs at different wavelengths. (a) Ag based nanopatterned plasmonic metamaterials for blue QW LEDs. (b) nanopatterned Ag-Si multilayer HMMs for green QW LEDs. (c) Purcell factor calculation for a QW dipole emitter at a distance of 10 nm away from the uniform Ag-Si multilayer HMMs with the Ag filling ratio range from 0.6 to 1 (with 1 corresponding to a pure Ag film). The Ag-Si multilayers have a thickness period of 20 nm and 5 periods in total. The bottom layer is Si. Surrounding medium for the QW emitters is GaN, and the internal quantum efficiency is assumed to be 50%.

4.3 Theoretical and numerical designs

The interaction between QW dipole emitters and plasmonic nanopatterns was analyzed and calculated using a 3D full-wave simulation scheme introduced in Chapter 3.2.2. The optimized geometry, including nanodisk thickness, diameter and array period, for respectively employed plasmonic metamaterials will be systematically investigated and designed.

Figure 4.2 (a) shows a unit cell of the Ag plasmonic metamaterial nanodisk array sitting 10 nm above the QW active layer where the red arrow indicates the QW dipole emitter located at the center axis of the Ag nanodisk. A thickness of 20 nm was chosen for the Ag nanodisk since simulations indicate the Purcell factor starts to saturate for Ag film thickness larger than 20 nm. The QW dipole emitter sits in the GaN medium with the other half surrounding space to be air. The internal quantum efficiency η_0 of the QW dipole emitter was kept at 50%. The rest of the geometry parameters for Purcell enhancement optimization includes the nanodisk diameter D and the period of the array A. Figure 4.2 (b) shows a calculation result of Purcell factor and radiative enhancement for a QW dipole oriented parallel to a Ag nanodisk array of $D = 80$ nm and $A = 200$ nm. The permittivity for Ag was taken from [103], and the collection angle for the radiative enhancement was fixed at $\pm 30^\circ$. Purcell factor for such nanopatterned Ag plasmonic metamaterials has an enhancement factor of close to 40 fold aligned exactly with the blue LED emission wavelength at 460 nm. Meanwhile, strong radiative enhancement is achievable at close wavelengths due to the out-coupling effect from the nanopatterns.

Both Purcell factor and radiative enhancement depends on the Ag nanodisk diameter and the array period. Figures 4.2 (c,d) illustrate such dependence by plotting out the maximum enhancement factors within the wavelength range 460 ± 20 nm as a function of the period A and diameter D, respectively. Purcell factor does not have strong dependence on these two geometry parameters when the dipole location was fixed at the center. When the Ag nanodisk diameter keeps 80 nm, Purcell factor generally stays around 36-37 fold as the periods sweep from 150 nm across 250 nm as shown in Figure 4.2 (c), which indicates the Purcell en-

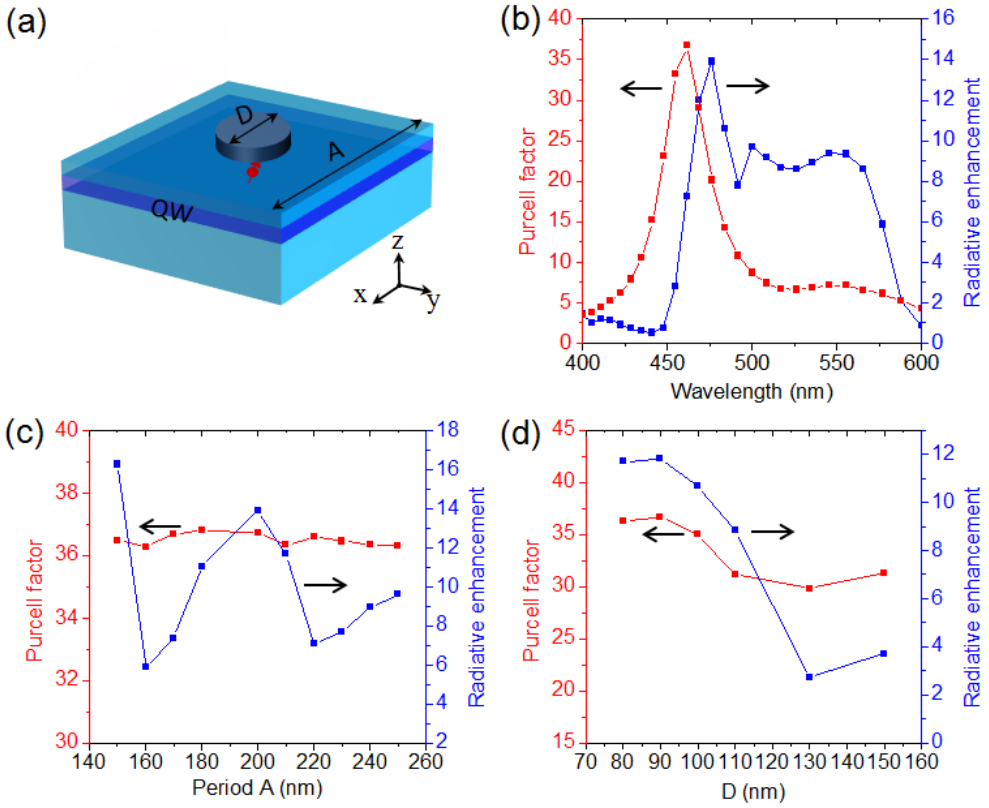

Figure 4.2: Numerical simulation for the geometry design of Ag plasmonic metamaterials. (a) One unit cell of the Ag plasmonic metamaterial nanodisk array, 10 nm above the QW active layer where the red arrow indicates the QW dipole emitter located at the center axis of the Ag nanodisk. The nanodisk has a thickness 20 nm. Internal quantum efficiency η_0 of the QW dipole emitter is 50%. (b) Calculation of Purcell factor (red) and radiative enhancement (blue) for a QW dipole oriented parallel to a Ag nanodisk array of $D = 80$ nm and $A = 200$ nm. The collection angle for the radiative enhancement is $\pm 30°$. (c) Maxima of Purcell factor (red) and radiative enhancement (blue) within the wavelength range 460±20 nm for a QW dipole oriented parallel to a Ag nanodisk array as the period A varies and the diameter $D = 80$ nm. (d) Maxima of Purcell factor (red) and radiative enhancement (blue) within the wavelength range 460±20 nm for a QW dipole oriented parallel to a Ag nanodisk array as the diameter D varies and the period $A = 210$ nm.

hancement is more local interaction. Yet at a period of 210 nm, it increases some when the diameter shrinks (Figure 4.2 (d)). Companying the Purcell factor, radiative enhancement evolves more dramatically as the geometry parameters change. First, the radiative power becomes periodically modulated as the out-coupling array period increases, indicating the strong dependence of radiative enhancement on the plasmonic metamaterial periods. Each radiative enhancement maximum corresponds to the period that could provide the best out-coupling wavevector, and in general, smaller periods provide higher wavevectors for accessing more DOS of the SPPs. Second, smaller nanodisk diameters bring up the radiative power by overlapping the spatial radiative enhancement maxima with the QW dipole emitter. Stronger local electric field interaction enables higher far-field radiative power.

Similar geometry parameter investigation was carried out for the nanopatterned Ag-Si multilayer HMMs as shown in Figure 4.3. Before that, an appropriate Ag-Si filling ratio should be chosen to best align Purcell enhancement with the green wavelength at 530 nm. In this simulation, a Ag filling ratio of 90% was used and the Ag-Si multilayer HMMs consist of 6 pairs of 18 nm Ag and 2 nm Si with the bottom Si layer. Figure 4.3 (b) shows calculated Purcell factor (red line) and radiative enhancement (blue line) for a QW dipole emitter parallel to a Ag-Si multilayer nanodisk array with $D = 100$ nm and $A = 200$ nm. The internal quantum efficiency was set to be 50% and radiative power collection angle to be $\pm 30^{\circ}$. Purcell factor peaks around $\lambda = 530$ nm best aligned with the targeting green LED wavelength with an estimated 35-fold spontaneous emission rate enhancement for a parallel dipole. Meanwhile, radiative enhancement of over tenfold could be achieved at exactly the same wavelength range, indicating the simultaneous spontaneous emission intensity and rate enhancement. These enhancement can be further optimized by varying the Ag-Si multilayer HMMs geometry parameters as presented in Figure 4.3 (c,d). As Purcell factor stays more or less 35 fold, the radiative enhancement could be further improved by using smaller nanodisk diameters.

To better understand the Purcell interaction of QW dipole emitters with the plasmonic metamaterials, spatial distributions of Purcell factor and radiative

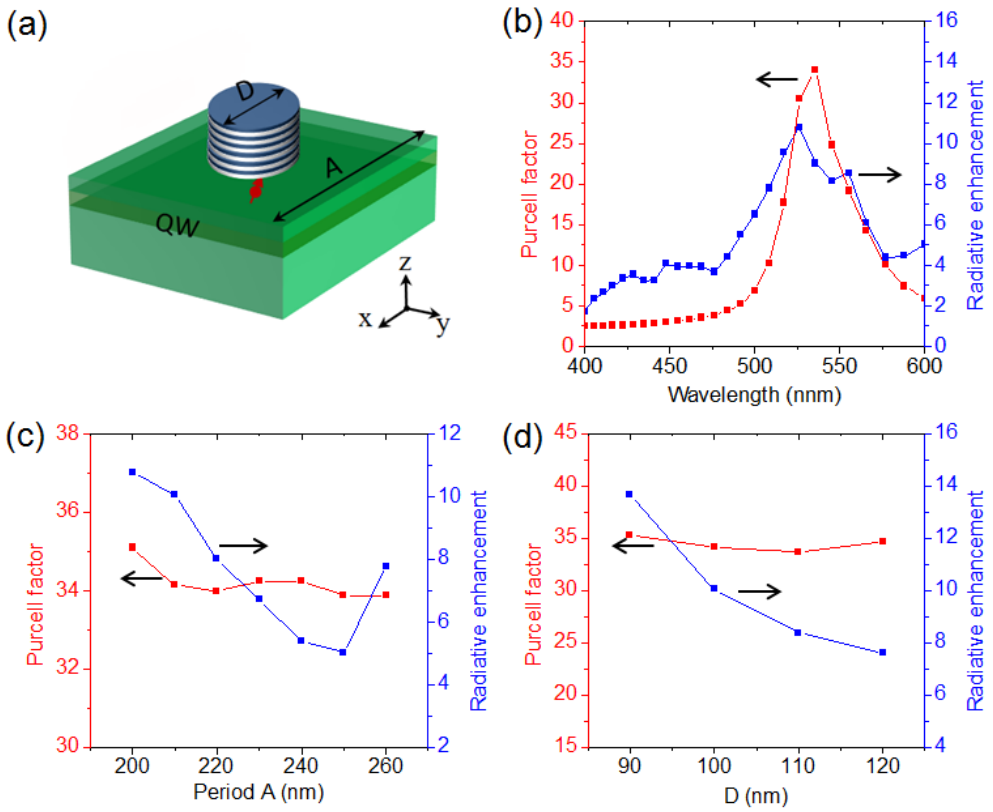

Figure 4.3: Numerical simulation for the geometry design of Ag-Si multilayer plasmonic metamaterials. (a) One unit cell of the Ag-Si multilayer HMM nanodisk array, 10 nm above the QW active layer where the red arrow indicates the QW dipole emitter located at the center axis of the nanodisk. The nanodisk has 6 pairs of 18 nm Ag and 2 nm Si with the bottom Si layer. Internal quantum efficiency η_0 of the QW dipole emitter is 50%. (b) Calculation of Purcell factor (red) and radiative enhancement (blue) for a QW dipole oriented parallel to a Ag-Si multilayer nanodisk array of $D = 100$ nm and $A = 200$ nm. The collection angle for the radiative enhancement is $\pm 30°$. (c) Maxima of Purcell factor (red) and radiative enhancement (blue) within the wavelength range 530±20 nm for a QW dipole oriented parallel to a Ag-Si multilayer nanodisk array as the period A varies and the diameter $D = 100$ nm. (d) Maxima of Purcell factor (red) and radiative enhancement (blue) within the wavelength range 530±20 nm for a QW dipole oriented parallel to a Ag-Si multilayer nanodisk array as the diameter D varies and the period $A = 210$ nm.

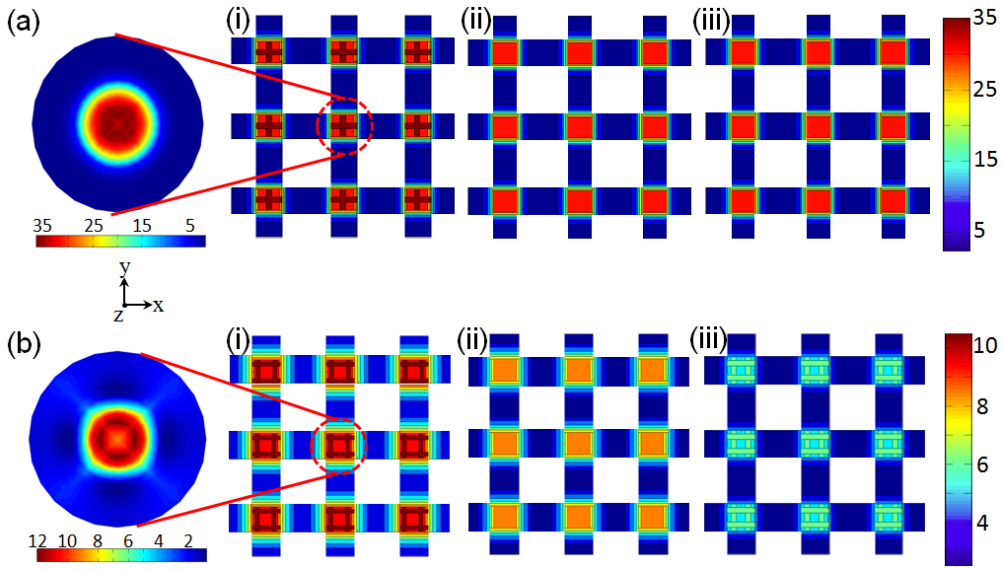

Figure 4.4: Numerical simulation for the spatial distribution of Purcell factor (a) and radiative enhancement (b) of QW dipole emitters in x-y plane at a distance of 10 nm away from nanopatterned Ag-Si multilayer plasmonic metamaterials with periods 200 nm (i), 220 nm (ii), and 230 nm (iii). The enlarged plots on the left provide finer mapping for respective enhancement factors. The wavelength is fixed at 530 nm.

enhancement in the x-y plane at a distance of 10 nm away from the Ag-Si multilayer nanodisk with different geometry periods were compared in Figure 4.4. Generally, strong Purcell effect mainly takes place at locations right underneath the nanodisk. Smaller period $A = 200$ nm provides both larger Purcell factor and radiative enhancement as previously discussed. Purcell factor has a spatial maximum mainly confined close to the center of the nanodisk whereas the radiative enhancement displays four maxima around the center which will further move to the center as the diameter becomes smaller. This spatial mapping of key parameters provides guidelines to the distribution of the QW emitters.

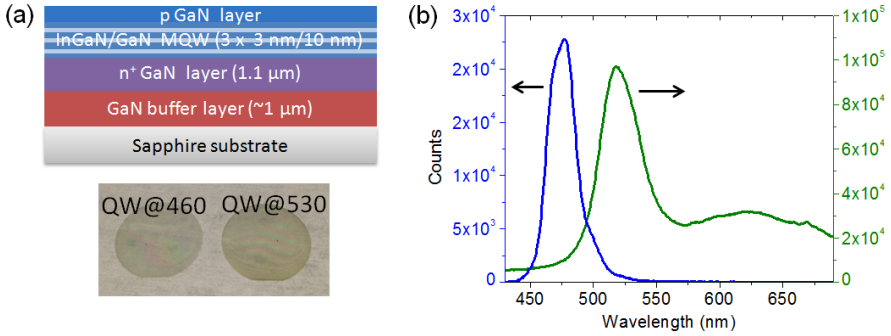

Figure 4.5: (a) Schematic drawing of typical cross-section of a LED structure and optical images of two grown LED samples targeting different emission wavelengths. (b) Photoluminescence spectra of two grown InGaN/GaN multi-QW LED samples with blue (474 nm / 26 nm) and green (520 nm / 40 nm) emissions.

4.4 Ag plasmonic metamaterials for enhancing blue QW LEDs

To experimentally demonstrate the Purcell enhancement of QW LEDs at different emission wavelengths, InGaN/GaN multi-QW LED wafers were grown using a (Thomas Swan close-coupled showerhead 3×2") metal organic chemical vapor deposition (MOCVD) system. Figure 4.5 (a) shows the schematic drawing of the typical cross-section of a LED structure and two grown LED samples targeting different emission wavelengths. 2-inch (double side polished) c-sapphire wafers were used as the substrates. Traditional low-temperature (LT: 530°C) GaN nucleation layer method was used followed by high-temperature (HT: 1040°C) GaN buffer layer for the material growth [104]. Subsequently a 1.1 μm HT n^+-GaN ($n \approx 5 \times 10^{18}$ cm^{-3}), three periods of InGaN/GaN multi-QWs and a top-capping 70 nm p-GaN ($p \approx 8 \times 10^{17}$ cm^{-3}) were grown. Specifically, the multi-QWs were grown at temperatures of 690°C (675°C for 530 nm emission) and 840°C for 2 nm InGaN wells (3 nm for 530 nm emission) and 10 nm GaN barriers, respectively. Finally, p-GaN activation by in-situ annealing in N_2 were performed. The top-capping p-GaN was grown for electrically-pumped LEDs whereas a 10 nm GaN barrier layer will be used as the spacer instead of the p-GaN layer for optically-pumped LEDs.

Figure 4.5 (b) shows photoluminescence spectra of two grown InGaN/GaN multi-QW LED samples measured by a microspectroscopy system. After excited by a 405 nm CW laser, emission from the QWs was collected with an objective of 50×, numerical aperture (NA) = 0.55 and a longpass filter (409 nm) before resolved by a Czerny-Turner spectrograph (Andor Shamrock 303i). The spectrograph was equipped with a diffraction grating of 150 lines/mm and a blaze wavelength at 500 nm, and a charge coupled device (CCD) camera (Andor Newton CCD). A dichroic beamsplitter (405 nm) was used to block the laser light collection. The blue LED has a peak emission around 474 nm with a bandwidth 26 nm, whereas the green LED has a peak around 520 nm with a bandwidth 40 nm.

The enhancement of blue QW LEDs was demonstrated experimentally by integrating nanopatterned Ag plasmonic metamaterials into the near-field of QWs. Figure 4.6 (a) shows the schematic drawing of the preliminary layout of an electrically pumped Ag plasmonic metamaterial enhanced QW LED. LED samples were fabricated following standard cleanroom processes for defining the emitting die area. Ag layer of 30 nm with Ni wetting layer was deposited by e-beam evaporation on to a dry-etch patterned p-GaN layer, forming the nanopatterned Ag plasmonic metamaterials with different geometry parameters. Optical image in Figure 4.6 (b) shows the top view of the fabricated LED device with the zoon-in dark-field optical image of the Ag plasmonic structures embedded in the p-GaN layer. Different plasmonic nanopatterns were included together with a flat Ag film (big square) for comparison. The spacing between the plasmonic structure and the quantum well was kept as small as ∼10 nm to fully utilize the enhanced SPP resonances. The SEM image corresponds to one typical nanopattern with a period of 300 nm before the Ag deposition.

The electroluminescence spectra of the LED devices were characterized by the microspectroscopy system. Electrically pumped luminescence from the bottom side of the sample was collected and analyzed by the spectrograph and corresponding images were taken by a CCD camera. The electroluminescence image of the device at a DC voltage of 5 V is present in Figure 4.6 (c). Emission from patterned areas (1,2,3) has much higher intensity than from the flat area (4). Figure

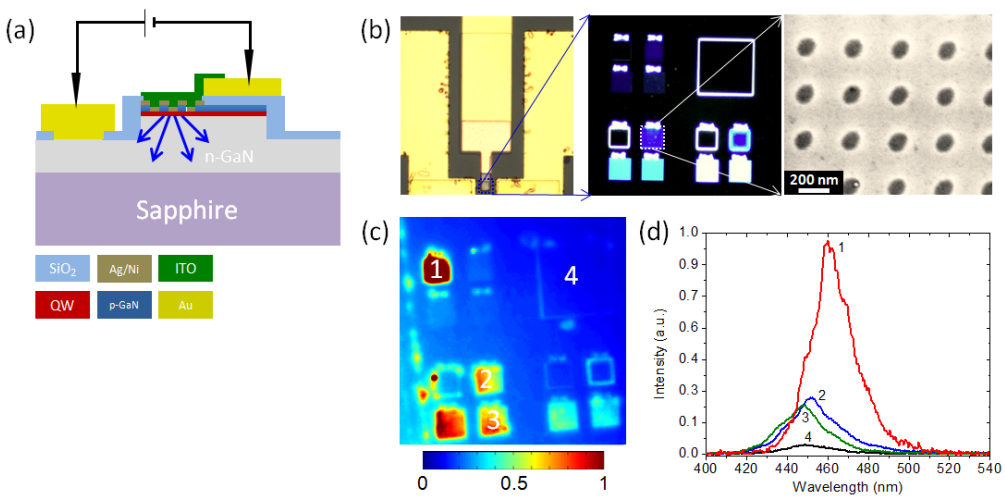

Figure 4.6: Electrical-pumped Ag plasmonic metamaterial enhanced QW LEDs. (a) Schematic cross-section layout of the Ag plasmonic LED. (b) Top-view optical image of the fabricated Ag plasmonic LED with a zoon-in dark-field optical image of the nanopatterned structures. The SEM image shows one nanopattern with a period of 300 nm. (c) Optical image of the electroluminescence intensity under a DC voltage of 5 V for nanopatterns with the periods 200 nm (1), 300 nm (2), 500 (3), and flat Ag area (4). (d) Electroluminescence spectra at a DC voltage of 5 V corresponding to areas in (b).

4.6 (d) gives the measured emission spectra corresponding to different areas in (c). Generally, smaller periods better out-couple plasmonic modes and strongly enhance the emission intensity. A close to 40-fold emission enhancement was obtained with nanopatterned plasmonic LED with a period of 200 nm compared with the flat Ag area at the peak emission wavelength of 460 nm. The emission enhancement depends on the nanostructure parameters, which could be mapped out experimentally by studying more geometry patterns.

4.5 Ag-Si multilayer HMMs for enhancing green QWs

Purcell enhancement for GaN QW LED emitting at green wavelength will be achieved by utilizing nanopatterned Ag-Si multilayer HMMs. The Ag-Si multilayers, made of 5 pairs of 2 nm Si and 18 nm Ag layers with a capping Si layer of

5 nm, were prepared by alternatively DC magnetron sputtering Si and Ag layers onto QW LED substrates with a 10 nm GaN barrier as the spacer at room temperature. Using 40 nm Ni patterned by ebeam lithograph as the etching mask, Ag-Si nanodisk structures with different geometry parameters were made by reactive ion etching process.

The lifetime of the InGaN/GaN Multi-QWs with nanopatterned Ag-Si multilayer nanodisks was measured by time-resolved photoluminescence in a lab-built two-photon microscope system as shown in Figure 4.7 (a). A Ti:Sapphire laser system (Spectra-Physics Mai Tai) with a pulse width of less than 100 fs and an intrinsic repetition rate of 80 MHz was incident to excite QWs, with the excitation wavelength chosen at 800 nm. The excitation laser passes through a longpass filter (660 nm), a dichroic shortpass beamsplitter (690 nm), an objective of 20×, numerical aperture (NA) = 0.45, before illuminating the QW samples. Emission light collected by the same objective was filtered by a series of filters to improve the signal to noise ratio, including a shortpass filter (690 nm), two BG39 glass windows ($<\sim$600 nm pass), and a bandpass filter (520 nm, bandwidth 20 nm) before recorded by a Horiba picoseconds photon detection module. The spatial mapping of lifetime was enabled by scanning the QW sample across the laser spot (1-2 μm diameter) using a nanostage controlled by a two axis electronic controller (MCL Nano-Drive 85). A step size of 1 μm was used with a 10 ms delay and 10 s dwell time on each pixel.

Figure 4.7 (b) gives the time-resolve photoluminescence results for QWs with different Ag-Si multilayer nanodisk periods. Compared with the single slow exponential decay for bare QWs, the time-resolved decay for QWs interacting with the plasmonic structures is dramatically faster and displays multiple decay regions. The fastest decay rate for nanopatterns with a period of 250 nm is measured to be 1/160 ps^{-1}, which is strongly enhanced compared with 1/3.75 ns^{-1} for bare QWs. The spontaneous emission rate is further improved by plasmonic structures with a smaller period 200 nm that better out-couples high-wavevector plasmonic modes. A fastest decay rate of 1/65 ps^{-1} was observed and corresponding 58-fold Purcell enhancement was demonstrated. This implies the potential of plasmonic

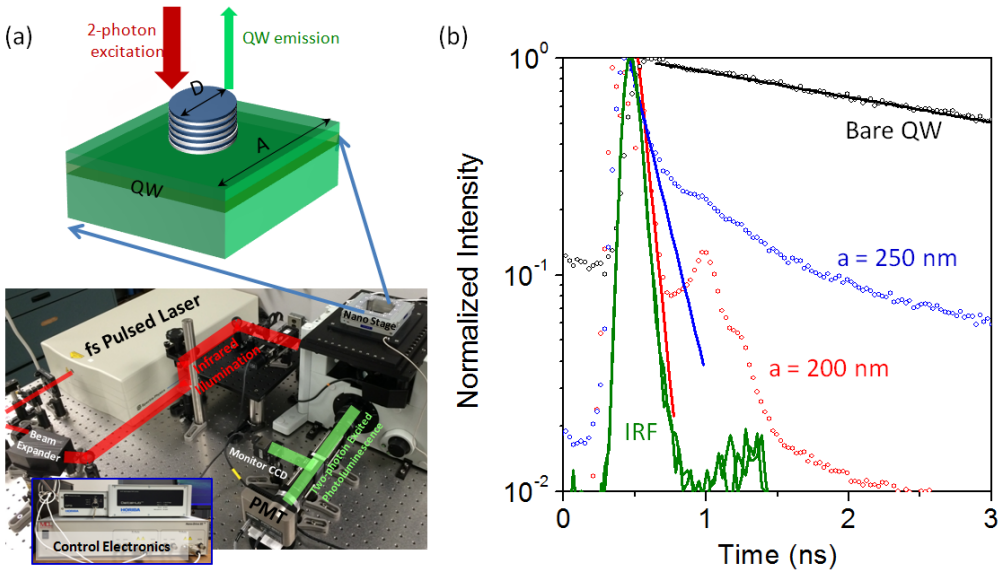

Figure 4.7: Time-resolved photoluminescence characterization of QW LEDs with different plasmonic structures. (a) A two-photon microscope system for time-correlated single photon counting and spatial mapping. (b) Time-resolved photoluminescence measurement for bare QWs (black), QWs with nanopatterned Ag-Si multilayer HMMs (blue: period 250 nm; red: period 200 nm) after normalized to the maximum of individual curves observed at the emission wavelength of 520 nm. The green curve corresponds to the instrumental response function (IRF).

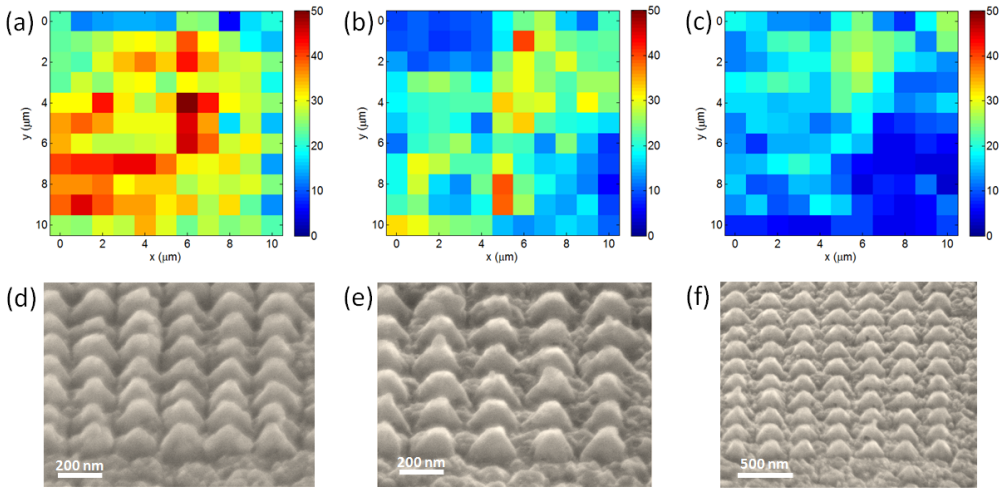

Figure 4.8: Spatial Purcell factor mapping of green QW LED with nanopatterned Ag-Si multilayer HMMs with the array period 200 nm (a), 250 nm (b), and 300 nm (c) at the wavelength of 520 nm. Corresponding SEM images at a tilted angle for the Ag-Si multilayer nanostructures with the period 200 nm (d), 250 nm (e), and 300 nm (f).

metamaterial enhanced QW LEDs for high-speed direct modulation with a 3 dB modulation speed of ∼9.3 GHz.

Such Purcell enhancement is spatially dependent and can be also measured experimentally by scanning the excitation laser spot across the nanopatterned samples. Figure 4.8 (a,b,c) provides the spatial mapping of Purcell factor for nanopatterned Ag-Si multilayer HMMs with different periods at the wavelength of 520 nm obtained by normalizing enhanced spontaneous emission rate to bare QWs. Corresponding SEM images of mapped nanostructures are also included below each Purcell map. Although not very uniform, higher Purcell factor was observed spatially for smaller nanopattern periods. Better uniformity could be obtained by improving the nanostructure quality.

4.6 Conclusion

In conclusion, we extend the concept of tunable Purcell enhancement by nanopatterned plasmonic metamaterials to InGaN/GaN QW LEDs and experimentally demonstrate the spontaneous emission intensity and rate enhancement

at blue (460 nm) and green (520 nm) wavelengths, respectively. Based on theoretical calculation and numerical simulations, Ag based nanodisk array was used to improve the electrically pumped LED light intensity at 460 nm, whereas nanopatterned Ag-Si multilayer HMMs strongly enhanced spontaneous emission rate of green QWs based on time-resolved photoluminescence measurements. LEDs with 3 dB modulation speed of ∼9.3 GHz have useful applications in high-speed wireless communications or Li-Fi.

This work was supported by ONR Young Investigator Award (no. N00014-13-1-0535), NSF-ECCS (grant no. 0969405) and NSF-CMMI (grant no. 1120795).

Chapter 4, in part, is being prepared for submission for publication. Dylan Lu, Haoliang Qian, Kangwei Wang, Bryan VanSaders, Paul K. Yu, and Zhaowei Liu, "Plasmonic metamaterial enhanced InGaN/GaN blue light-emitting diodes (tentative)." The dissertation author was the first author of this paper.

Chapter 4, in part, is being prepared for submission for publication. Dylan Lu, Haoliang Qian, Kangwei Wang, Feifei Wei, Eric E. Fullerton, Paul K. Yu, and Zhaowei Liu, "Multilayer hyperbolic metamaterials speeding up green InGaN/GaN quantum wells (tentative)." The dissertation author was the first author of this paper.

Chapter 5

Anomalously weak scattering in hyperbolic metamaterials

5.1 Background

EM wave scattering is a ubiquitous phenomenon in systems with refractive index contrast between an obstacle and the surrounding material [105]. When illuminated by incident EM waves, electric charges in the obstacle oscillate in response to the excitation field, transferring energy by re-radiation or absorption. The re-radiation pattern and polarization strongly depends on the geometry and size of the obstacle as well as the wavelength-dependent optical properties of its constituent materials [106]. The study of EM scattering by obstacles in the past century has yielded deep physical insight in the prediction of light transmission by atmospheric dust, interstellar particles, or colloidal metals [107, 108, 109, 110], and practical applications in radar cross-section control in stealth technology and medical imaging [111, 112]. Recent advances in plasmonics have revealed strongly dispersive scattering in metallic nanostructures by localized SP resonances, which have been widely explored and utilized for imaging and sensing [5, 113, 114, 115, 116]. Coupling between nanostructures introduces additional degrees of control for improving the scattering efficiency and directionality at the nanometer scale [117, 14, 3, 118, 15, 119, 120]. However, the fixed optical properties of naturally

existing metallic materials limit the range of performance and impose theoretical and practical restrictions.

Metamaterials, one type of artificial nano-structured composites, provide a new route for realizing either attenuated or enhanced plasmonic scattering with designable bandwidths and directions [119, 120, 23, 24, 25, 26, 121, 122, 123, 124, 125, 126, 127, 128, 129, 130]. By engineering material composition in space following the invariance of Maxwell's equations, transformation optics and conformal mapping enable unprecedented control of light for the realization of cloaking [23, 24, 25, 26]. Alternatively, the scattering cross section of an object can be significantly reduced by additional thin layers of plasmonic cover based on scattering cancellation schemes [121, 122, 123, 124]. Metamaterials have also been shown to produce either EM induced transparency (EIT) like features [125, 126, 127] or super-scattering [128, 129, 130] by exploiting coupled resonances in subwavelength objects. Special designs of single plasmonic structures incorporate both suppressed and highly resonant scattering responses in close frequency ranges [131, 132]. Yet the existing proposed schemes rely heavily on mode engineering with complex nanoscale geometry design and are extremely sensitive to fabrication imperfections. Moreover, the resonances in these designs are typically accompanied by strong material absorptions, further limiting the practical applications.

In this chapter we describe an approach where instead of manipulating resonances, we control the scattering by engineering the material properties of anisotropic multilayer-based metamaterials. Multilayer HMMs have recently drawn tremendous attention for providing a simple but effective platform for tunable material properties [28, 70, 72, 73, 75, 133, 87]. Exploiting the properties of HMMs we demonstrate control of EM wave interaction with plasmonic structures by engineering the effective optical constants in Au-Si multilayer HMMs. In contrast with strong plasmonic scattering from pure metallic structures, patterns of various sizes ranging from deep-subwavelength to wavelength scales in Au-Si multilayer HMMs become invisible in a manner that is not achievable with natural metallic or high-index materials. Such anomalously weak scattering (AWS) from metamaterials comprised of conductive components is possible when the permittivity of the

HMMs along the direction of incident electric field impedance-matches with the surrounding medium. At wavelengths away from the AWS, Au-Si HMMs present either metallic-like or dielectric-like scattering behavior. This exotic dispersive plasmonic scattering in HMMs can be applied to patterns of any geometry or size, and by changing the filling ratios of constituent materials it is possible to tune AWS behavior to desired optical wavelengths. We demonstrate this AWS experimentally by the optical characterization of various patterns in Au-Si HMMs, with corroborating full-wave numerical simulations. This stealth functionality in HMMs may lead to potential applications in optical encryption, noninvasive conductive probe designs, and invisible opto-electric devices.

5.2 Concept of AWS

When EM plane waves propagate through a homogeneous medium (ϵ_1), the scattering potential built by the presence of a subwavelength obstacle made of non-magnetic materials with permittivity contrast scatters waves omnidirectionally. For an incident z-polarized plane wave (TE) propagating in the x-y plane, the wave equation describing the resulting electric field distribution as EM waves interact with the obstacle can be written in a general form as,

$$\frac{1}{\omega\mu_y}\frac{\partial^2}{\partial x^2}E_z+\frac{1}{\omega\mu_x}\frac{\partial^2}{\partial y^2}E_z+\omega\epsilon_z E_z=0, \tag{5.1}$$

where E_z denotes the total electric field along the z direction; ω is the angular frequency in free space; ϵ_i and μ_i $(i=x,y,z)$ are permittivity and permeability of the constituent materials along different axes, respectively. For non-magnetic materials, only the permittivity along the z direction in the obstacle responds to the incident electric field, leading to perturbation of the original EM waves. The general analytical expression for the resulting total electric field in the far field will be a summation of the incident and the scattered fields given as follows [105],

$$E_z(\boldsymbol{r})\hat{z}=E_z^{(i)}(\boldsymbol{r})\hat{z}-k^2\hat{r}\times\hat{r}\times\hat{z}\int_V\left(\epsilon_z(\boldsymbol{r'},\omega)/\epsilon_1-1\right)E_z(\boldsymbol{r'})\mathrm{e}^{-i\boldsymbol{k}\cdot\boldsymbol{r'}}\mathrm{d}\boldsymbol{r'}\frac{\mathrm{e}^{ikr}}{r}, \tag{5.2}$$

where $E_z^{(i)}$ denotes the incident electric field, ϵ_1 the permittivity of the surrounding media, the wave number $k=\omega\sqrt{\epsilon_1}/c$, the position vector of the evaluating point $\boldsymbol{r}=$

$r \cdot \hat{r}$, and the time-dependent factor $\exp(-i\omega t)$ has been omitted. This integration describes the overall effect on the scattering field evaluated at the far-field by the scattering potential of the obstacle volume (V) due to the permittivity contrast $\epsilon_z(\boldsymbol{r'},\omega)/\epsilon_1 - 1$. Therefore, z-polarized light scattering by the obstacle can be almost entirely eliminated by matching its permittivity along the z direction with the surrounding medium, that is, $\epsilon_z = \epsilon_1$.

For a plane wave polarized and propagating in the x-y plane (TM wave), the wave equation can be written as,

$$\frac{1}{\omega\epsilon_y}\frac{\partial^2}{\partial x^2}H_z + \frac{1}{\omega\epsilon_x}\frac{\partial^2}{\partial y^2}H_z + \omega\mu_z H_z = 0, \tag{5.3}$$

where H_z denotes the total magnetic field along the z direction. For non-magnetic materials, permittivities along x and y directions in the obstacle respond to the incident electric field, leading to perturbation of the original EM waves. The general analytical expression for the resulting total magnetic field in the far field will be a summation of the incident and the scattered fields given as follows [105],

$$H_z(\boldsymbol{r})\hat{z} = H_z^{(i)}(\boldsymbol{r})\hat{z} + k^2\hat{r}\times \int_V \left(\left(\frac{\epsilon_x(\boldsymbol{r'},\omega)}{\epsilon_1} - 1\right)E_x(\boldsymbol{r'})\hat{x} + \left(\frac{\epsilon_y(\boldsymbol{r'},\omega)}{\epsilon_1} - 1\right)E_y(\boldsymbol{r'})\hat{y}\right)\mathrm{e}^{-i\boldsymbol{k}\cdot\boldsymbol{r'}}\,\mathrm{d}\boldsymbol{r'}\frac{\mathrm{e}^{ikr}}{r}, \tag{5.4}$$

where $H_z^{(i)}$ denotes the incident magnetic field; $\hat{x}$, $\hat{y}$, and $\hat{z}$ are the unit vectors. Therefore, the impedance match condition for TM wave incidence is $\epsilon_x = \epsilon_1$, and $\epsilon_y = \epsilon_1$. In the case of normal incidence, that is, $E_y = 0$, the impedance match condition simplifies to $\epsilon_x = \epsilon_1$. For the multilayer-based metamaterials with the permittivites described by the effective medium theory, the impedance match condition $\epsilon_x = \epsilon_1$ can be satisfied for TE wave under arbitrary incident angles and TM wave incidence normal to the layer surface. For TM wave incidence oblique to the layer surface, the material response perpendicular to the layer surface introduces additional scattering fields, and therefore breaks down the AWS.

Unlike naturally occurring homogeneous metallic or dielectric materials that generally scatter light (Figure 5.1 (a,b)), the properties of multilayer-based metamaterials can be readily engineered, enabling exotic EM wave interaction. The

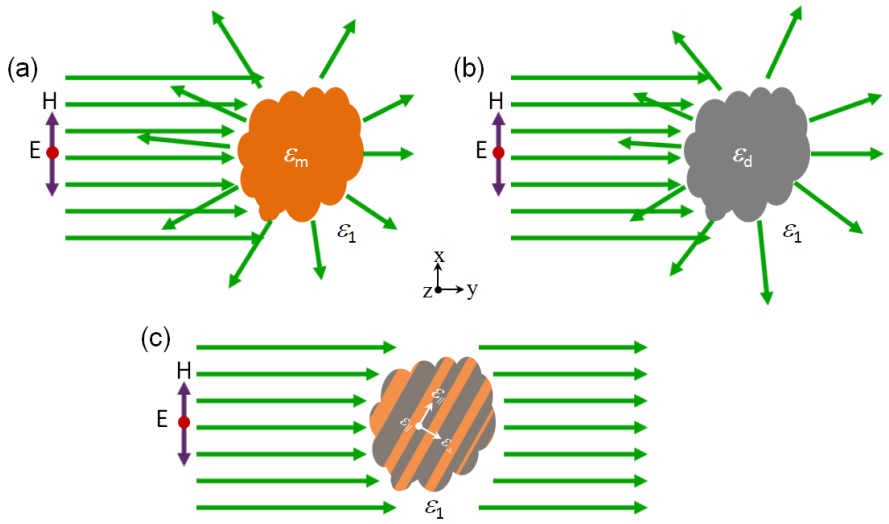

Figure 5.1: Schematics of anomalously weak scattering (AWS) by multilayer HMMs. EM plane waves polarized along the z axis are strongly scattered by an obstacle made of pure metal (a) or high-index dielectric (b) in the surrounding medium with permittivity ϵ_1, whereas AWS occurs for the obstacle comprised of HMMs (c).

permittivity of HMMs can be made highly anisotropic, identified by the effective permittivities parallel ($\epsilon_{\|}$) and perpendicular ($\epsilon_{\perp}$) to the plane of constituent layers (Figure 5.1 (c)). By careful choice of constituent materials and layer thickness light scattering by patterns in HMMs can be well controlled. In the case when the impedance matching condition, $\epsilon_{\|} = \epsilon_1$, is satisfied, EM waves propagate through the medium without seeing the obstacle, achieving a minimum scattering cross section corresponding to AWS (Figure 5.1 (c)).

5.3 Numerical demonstration of AWS

To illustrate the concept of controlling EM wave scattering by metamaterials, we utilize multilayered gold and amorphous silicon composites in our study. As shown in Figure 5.2 (a), full-wave numerical studies of wave propagation through a single slit was carried out for pure Au, Si, and Au-Si HMMs with a metal filling ratio 0.6. The numerical simulation was carried out in a two-dimensional x-y plane by using commercial software Comsol Multiphysics^{TM}. Plane waves with TE or

TM polarizations were incident normally or at a chosen angle onto the slit. Light scattered ($k_{\text{scattered}} \neq k_{\text{incident}}$) from the slits in the forward direction ($k_{\text{scattered}}$ less than 90° changed from k_{incident} and within the transmission half space defined by the uniform film boundary) was collected at different incident wavelengths to obtain the scattered intensity spectra. The permittivities for Au (ϵ_{m}) and Si (ϵ_{d}) are taken from refs. [41] and [42], respectively. The material property for the Au-Si HMMs is described by the effective medium theory with the effective permittivity parallel to the layer $\epsilon_{\parallel} = P\epsilon_{\text{m}} + (1-P)\epsilon_{\text{d}}$ and that perpendicular to the layer $\epsilon_{\perp} = \epsilon_{\text{m}}\epsilon_{\text{d}} \big/ (P\epsilon_{\text{d}} + (1-P)\epsilon_{\text{m}})$, where P is the volumetric filling ratio of Au. All the slits are 100 nm thick, 300 nm wide, and have a surrounding medium with refractive index of 1.5. As indicated by the electric field distribution, incident EM plane waves either reemit a cylindrical wave from the center of the slit in pure Au film or diffract at the edges in pure Si film. The resulting far field patterns off homogenous films are combinations of a Huygens point source (the slit) and plane waves (bulk transmission), which are attributed to their intrinsic optical properties, specifically the negative permittivity of Au and large index of Si in the optical wavelengths. However, EM waves propagate through a single slit in an Au-Si HMM by nearly retaining the original wavefront with only mild attenuation and negligible Huygens point source behavior. Furthermore, this anomalous wave interaction is not sensitive to the incident angle as long as TE polarization is maintained (Figure 5.2 (a) (iv)). These originally strong-scattering constituent materials when put together in an engineered manner result in close to zero scattering cross section of the imbedded patterns.

This phenomenon can be explained when the effective material properties of the multilayer metamaterials are examined. When the layer thickness in multilayer films is much smaller than the probing wavelength, an effective-medium approximation is commonly used to describe the permittivities along distinct directions, that is, $\epsilon_{\parallel}$ and $\epsilon_{\perp}$ (ref. [47]). Figure 5.2 (b) shows the anisotropic effective permittivities for a uniform Au-Si HMM with the Au filling ratio 0.6, where the red (blue) lines correspond to the component parallel (perpendicular) to the layer surfaces. The parallel permittivity displays a Drude-like dispersion that has posi-

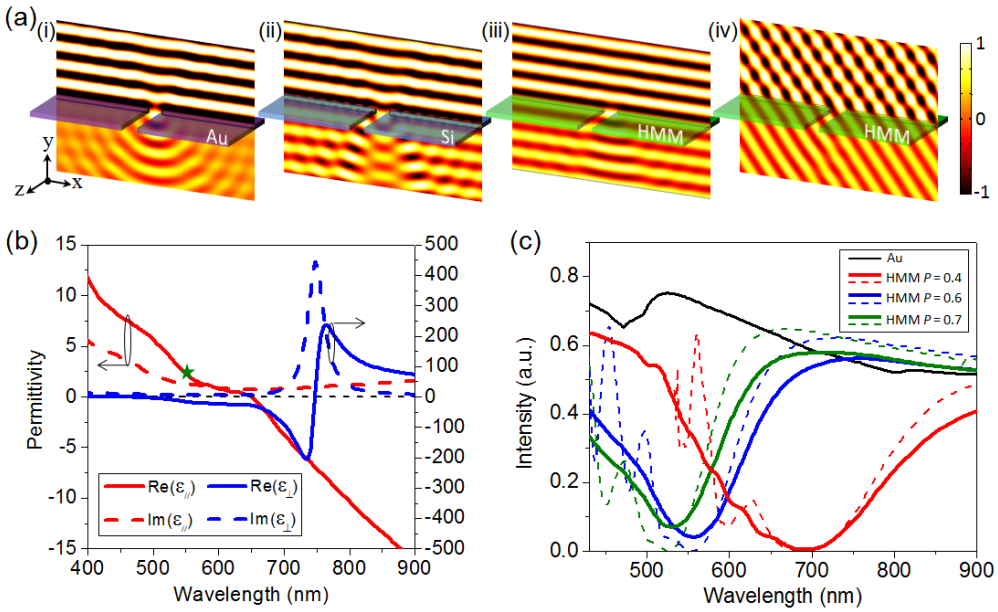

Figure 5.2: Numerical simulations of plasmonic scattering by slits in HMMs. (a) Simulated electric field distributions when a plane wave polarized perpendicular to the incident plane propagates through a single 300 nm wide slit in pure Au film (i), Si film (ii), and Au-Si HMMs with Au filling ratio 0.6 (iii, iv). Incident angles are 0° (i-iii) and 53° (iv). The thickness for all films is 100 nm, and illumination wavelength is fixed at 550 nm. (b) Real and imaginary parts of the permittivities for the Au-Si HMM with an Au filling ratio 0.6 perpendicular ($\epsilon_\perp$) and parallel ($\epsilon_\parallel$) to the constituent layers are calculated based on the effective medium theory. The black dash line corresponds to the zero line and the green star locates the permittivity parallel to the layer at the wavelength of 550 nm. (c) Simulated scattering intensity in the forward direction for EM waves normally incident onto a 80 nm-wide slit in the Au-Si HMMs with a thickness of 100 nm when the Au filling ratio P is tuned. Results for Au-Si HMMs assigned with complex (solid lines) or only real part (dashed lines) of the permittivities are presented. Scattering curves for the same slit in the pure Au film of the same thickness are included for comparison.

tive values at short wavelengths and gradually decreases below zero as wavelength is increased. At the location denoted by the green star, the real part of the parallel permittivity exactly matches the surrounding medium at a wavelength of 550 nm. According to equation (2), such an impedance match along the parallel direction alone results in zero scattering fields for a z-polarized incident EM wave, and thus AWS occurs. This condition can be perfectly satisfied and the incident plane wave is completely undisturbed if only the real part of the permittivity is considered. Imagery part of permittivity results in the attenuated transmission through HMMs with metallic components (Figure 5.2 (a)), which limit the size of encrypted pattern to wavelength scale to avoid high transmission contrast.

The strongly dispersive permittivities in the Au-Si HMMs give rise to highly varying scattering intensity across the whole optical regime (Figure 5.2 (c)). The scattering intensity dips correspond to the AWS which is invariant to TE incident angle and occurs for a wide range of surrounding-medium permattivities, even air, due to the large range of permittivity values covered by the parallel HMM component. At longer wavelengths, the HMM behaves more like a metallic film with stronger scattering intensity due to the effectively negative parallel permittivity, whereas at shorter wavelengths, it behaves as a dielectric film with an effectively positive parallel permittivity (Figure 5.3). By using different filling ratios for Au and Si, the AWS wavelength as well as the whole dispersive scattering curve can be tuned to desired wavelengths (Figure 5.2 (c)). As the Au filling ratio decreases, the AWS intensity gradually approaches the ideal limit with almost zero scattering at $P = 0.4$.

5.4 Experimental demonstration of AWS

5.4.1 HMM fabrication

In our experiment, the HMMs consisting of 10 pairs of 6 nm Au and 4 nm Si layers were prepared by sequential DC magnetron sputtering of Si and Au layers onto glass substrates at room temperature. The base pressure of the chamber was 5×10^{-8} Torr and the Ar sputtering gas pressure was fixed at 2.5 mTorr.

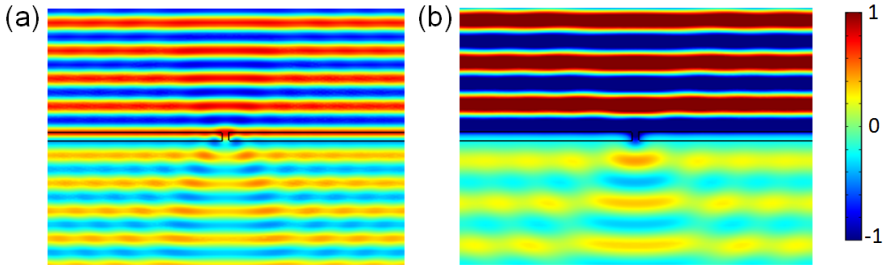

Figure 5.3: Simulated electric field distributions when a plane wave polarized perpendicular to the incident plane at the wavelength of 480 nm (a) and 700 nm (b) propagates through a single 80 nm wide slit in the Au-Si HMM with an Au filling ratio of 0.6. The thickness for the films is 100 nm.

Sputtering rates for Au at 50 W (∼2.5 W cm^{-2}) and Si at 100 W (∼5 W cm^{-2}) were 1.1 Ås^{-1} and 0.19 Ås^{-1}, determined by X-ray reflectivity measurements of calibration film sample thicknesses. 2 nm of Ta and 3 nm of Pd were deposited prior to Au and Si in order to promote adhesion of the multilayer structure to the glass substrate. Structures of several dimensions and shapes were milled into the multilayers by focused ion beam.

In Figure 5.4 (a), bright-field STEM images of cross-sectional views at different magnifications indicate a well-formed periodic lattice structure in the Au-Si multilayers with a highly conformal coating across the substrate. There is no accumulation of the film roughness throughout the growth direction, and the 10 nm thickness periods are well achieved. The element mapping for silicon and gold verifies the multilayer structure and some minor diffusion of Au into Si (Figure 5.4 (b)). The layer thicknesses and multilayer structure were also confirmed by X-ray reflectivity scans.

5.4.2 Optical characterization

The optical characterization of AWS in HMMs including the scattering and direct transmission spectra measured in a microspectroscopy system based on a Carl Zeiss inverted microscope (Axio Observer D1m). Broadband light from a halogen lamp passed through a linear polarizer and an angular controllable condenser illuminated the sample at an incident angle of 53° (numerical aperture (NA)

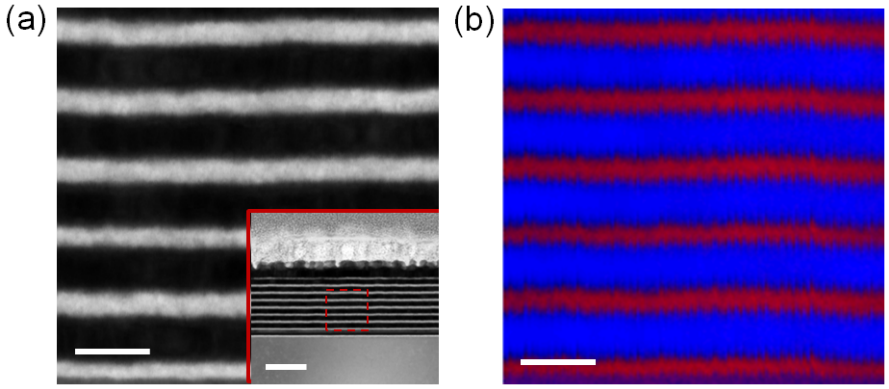

Figure 5.4: Fabrication of Au-Si multilayer HMMs. (a) Bright-field STEM images for the fabricated Au-Si HMM with the white (black) area corresponding to the Si (Au) layer. The inset shows the STEM image at a smaller magnification for the whole cross section of the Au-Si multilayer with the top thick Pt capping for imaging purposes. The Au-Si multilayer is comprised of 10 periods of 10 nm thickness each unit. The red dashed square outlines the imaging area of the main panel. Scale bars: main panel, 10 nm; inset, 50 nm. (b) Element mapping for constituent materials, silicon (red) and gold (blue), verifies the established multilayer lattice with some minor diffusion of Au into Si. Scale bar, 10 nm.

= 0.8). Dark-field scattering light from the samples in the forward direction was collected by an optical objective (50× magnification, NA = 0.55) and analyzed by a Czerny-Turner spectrograph (Andor Shamrock 303i). The spectrograph was equipped with a diffraction grating of 150 lines mm^{-1} (blaze wavelength at 500 nm) and a charge coupled device (CCD) camera (Andor Newton CCD). Direct transmission from the illumination light was carefully blocked so that not collected by the objective. The optical scattering images were captured by the same microscope setup using a Xenon lamp as illumination for its uniform intensity across the optical range, whereas transmission images were taken by a bright-field objective (50× magnification, NA = 0.55) at normal incidence. After passing through a bandpass optical wavelength filter with a bandwidth of 20 nm, the scattering and transmission images were taken by a CCD camera (Andor iXon EM+ 897).

Figure 5.5 (a) presents measured TE-polarized scattering spectra for different slit widths with the inset SEM image showing a 110 nm-wide sample. Strongly dispersive plasmonic scattering was observed in all slits with AWS occurring near the wavelength of 550 nm and strong scattering intensity at both shorter and

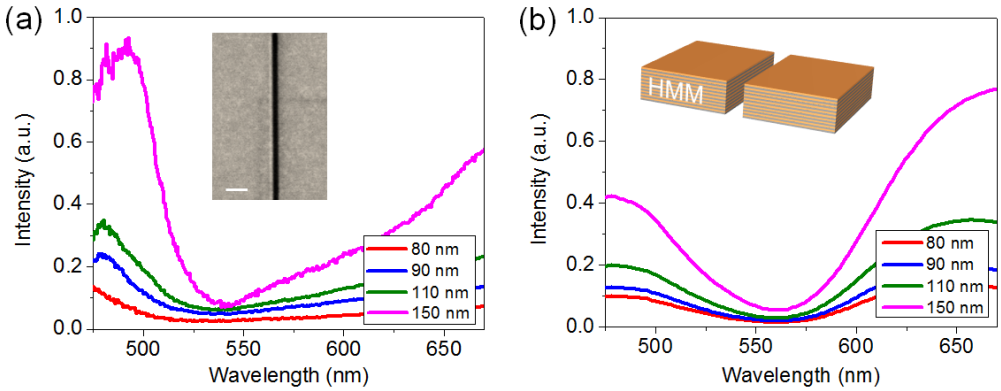

Figure 5.5: Optical scattering spectra of individual slits in the Au-Si HMM. (a) Measured dark-field scattering spectra in the forward direction for individual slits with different widths in the Au-Si HMM under TE-polarized light at an incident angle of 53°. The inset shows a SEM image of one fabricated slit with a width of 110 nm. Scale bar, 500 nm. (b) Simulated scattering spectra in the forward direction for individual slits with different widths in the Au-Si HMM under TE-polarized light at an incident angle of 53°. The inset plots the simulated geometry where real multilayered structure is used.

longer wavelengths. The scattering intensity at the AWS wavelength slightly increases with the slit width due to the non-ideal impedance matching resulting from finite material absorption in the HMMs. Numerical simulations (Figure 5.5 (b)) reproduce the phenomenon observed in real multilayer structures under an incident angle of 53°. Although these results are limited to TE wave incidence, scattering in the same system by TM waves also displays attenuated scattering intensity near the AWS wavelength, however with greater scattering due to the material response ($\epsilon_\perp$) to the probing electric-field component perpendicular to the layer surfaces (Figure 5.6).

5.4.3 AWS for optical stealth

Control over scattering of patterns in the HMMs by engineering material properties is not limited to single one-dimensional slits but is universal for randomly distributed holes, periodic diffraction gratings, and even arbitrarily shaped structures. Figure 5.7 (a) presents measured forward dark-field scattering spectrum of individual holes of various diameters from 140 nm to 230 nm in the Au-Si

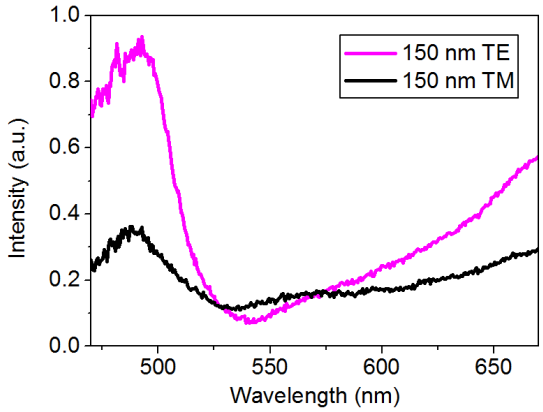

Figure 5.6: Measured scattering spectra in the forward direction for individual slits with a 150 nm width in the Au-Si HMM under TE and TM wave incidence at an angle of 53°.

HMMs with the inset SEM image corresponding to one typical fabricated single-hole structure. Individual holes display similar scattering characteristics to slits yet with a better spectral intensity contrast, and the AWS happens again close to the same wavelength of 550 nm. By distributing such individual holes, more complex patterns like letters of UCSD were also written into the Au-Si HMMs (Figure 5.7 (b)). Corresponding dark-field scattering and direct transmission images at three representative wavelengths were captured by a CCD camera using narrow bandpass optical wavelength filters as shown in Figure 5.7 (c) and (d), respectively. Comparing with well distinguished letter profiles at blue and red wavelengths, the existence of AWS in Au-Si HMMs hides letters completely in the background at the green wavelength. Despite the absorption in HMMs, optical demonstration of the AWS reveals potential stealth capability of multilayer based HMMs.

The AWS concept can also be extended to such optical devices as diffraction grating. A diffraction grating (period 750 nm, slit width 140 nm) was inscribed by focused ion beam into an Au-Si HMM with an Au filling ratio 0.6 (Figure 5.8 (a) SEM image). Scattering characterization of this grating shows an extremely small diffraction efficiency in the optical spectrum (white curve), corresponding to a prominent dark region of the pseudo colorful diffractive pattern in the green wavelengths (Figure 5.8 (a) colorful background). Unlike conventional optical grat-

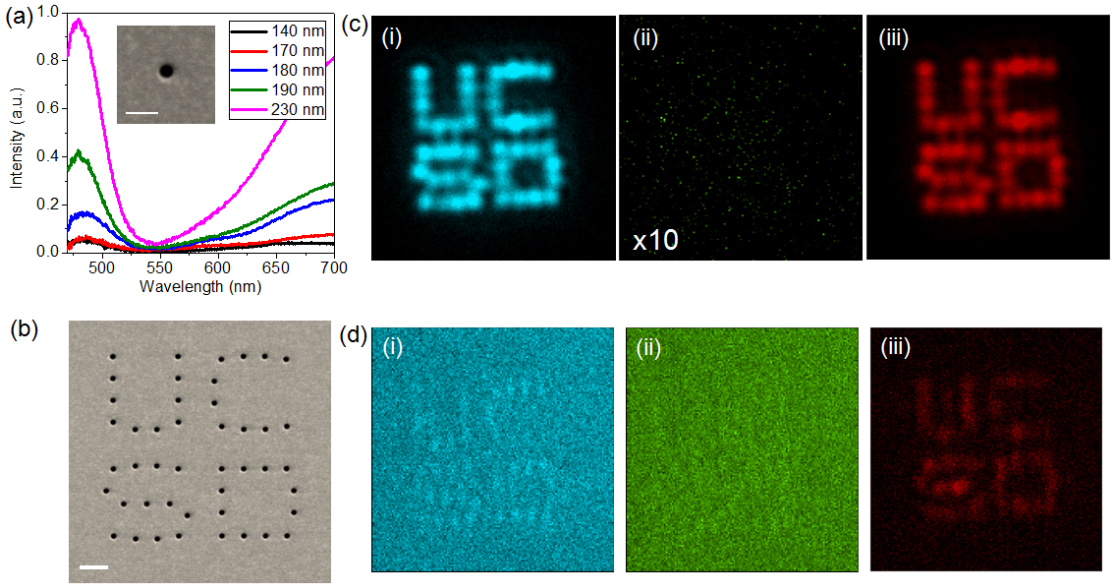

Figure 5.7: Spectrum and imaging characterization of individual and distributed holes in Au-Si HMMs. (a) Forward dark-field scattering spectrum of individual holes with various diameters ranging from 140 nm to 230 nm. The inset shows one SEM image of an individual hole. Scale bar is 500 nm. (b) SEM image of distributed holes forming letters "UCSD" in Au-Si HMMs with an Au filling ratio 0.6. Scale bar is 1 μm. (c) Forward dark-field scattering images in pseudo colors at the wavelengths 485 nm (i), 540 nm (ii), and 735 nm (iii) were captured using bandpass optical wavelength filters. The image intensity at the green wavelength is multiplied by a factor of 10 for better comparison. (d) Corresponding transmission images under normal incidence at the wavelengths 485 nm (iv), 540 nm (v) and 735 nm (vi) were taken by using the same filters.

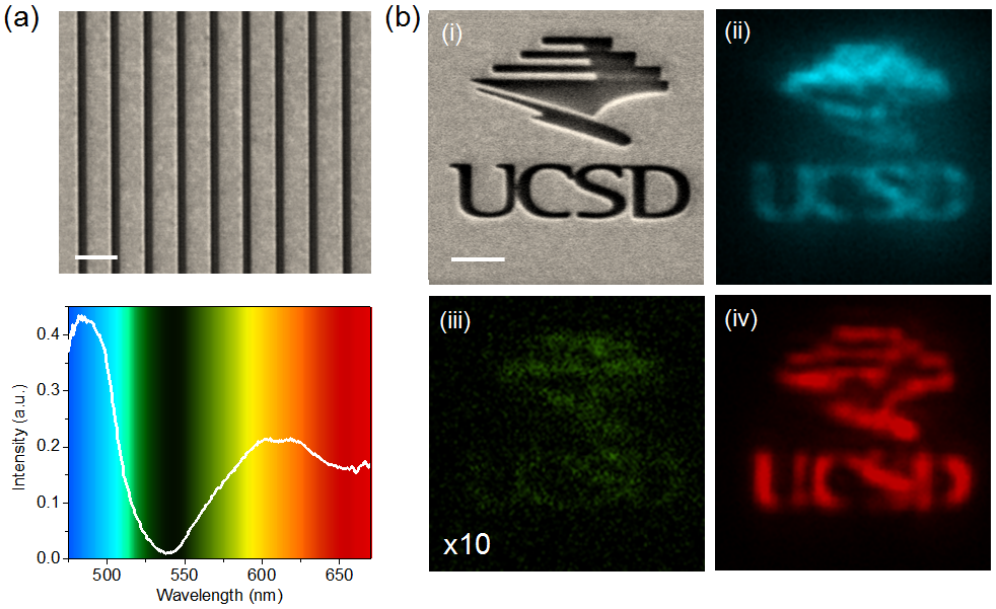

Figure 5.8: Spectrum and imaging characterization of AWS by periodically and randomly shaped patterns in Au-Si HMMs. (a) Top panel: SEM image of a HMM diffraction grating with a period of 750 nm and a slit width of 140 nm (Au fill ratio 0.6). Scale bar, 1 μm. Bottom panel: Experimentally measured dark-field scattering spectrum in the forward direction for this type of grating (white line) with the background showing the same optical spectrum in pseudo colors with the intensity corresponding to the scattering signal. (b) SEM image of the UCSD logo in an Au-Si HMM with an Au filling ratio 0.6 (i). Scale bar is 1 μm. Dark-field scattering images in pseudo colors at the wavelengths 485 nm (ii), 540 nm (iii), and 735 nm (iv) were captured in the forward direction using bandpass optical wavelength filters. The image intensity at the green wavelength is multiplied by a factor of 10 for better comparison.

ings with broadband diffraction, strongly dispersive scattering HMM gratings may find applications in optical imaging and sensing by filtering out unwanted spectral information.

Finally, we demonstrate that AWS in HMMs enable the opto-encryption of information of arbitrary shaped structures by rendering it undetectable at chosen wavelengths. The UCSD logo was milled into the Au-Si HMMs as an example of inscribed information (Figure 5.8 (b)).. Scattering images at blue and red wavelengths clearly outline the UCSD logo (Figure 5.8 (b) (ii, iv)), whereas at the green wavelength, the image of the logo has a barely detectable intensity of 50

fold dimmer due to AWS in the HMMs (Figure 5.8 (b) (iii)). Such tailored information encryption in the HMMs for certain wavelengths will be possibly applied in steganography and watermarking for anti-counterfeiting purposes.

5.5 Discussion

The demonstrated AWS effect in HMMs is geometry independent and can be tuned to any desired wavelengths by varying the material filling ratios. Owing to the anisotropic material properties in multilayer HMMs, the control of scattering is dramatic only for TE polarization, which may be overcome by constructing isotropic three-dimensional metamaterials using a similar scheme. Although the invisibility performance of demonstrated Au-Si multilayer based HMMs in the optical regime is still limited by the unavoidable material absorption, the concept of AWS will have promising application potential by constructing HMMs in near- or mid-infrared regions with reduced loss.

5.6 Conclusion

In conclusion, we demonstrate the control of plasmonic scattering by engineering the material properties of Au-Si multilayer-based HMMs. Patterns in such HMMs become invisible in a chosen band of optical frequencies due to AWS when the permittivity of the constituent HMMs impedance-matches with the surrounding medium. Experimental verifications of this new phenomenon by slits, holes, periodic gratings, and arbitrary objects in the HMMs prove this AWS insensitive to pattern size, shape and incident angles. This new type of tunable HMMs provides an effective and versatile platform for controlling EM wave scattering cross sections, leading to potential applications in optical stealth and invisible opto-electric devices.

This work is financially supported by the Office of Naval Research (ONR) Young Investigator Award (N00014-13-1-0535), NSF-ECCS (0969405), NSF-CMMI (1120795), and ONR MURI program (N00014-13-1-0678). The authors thank P.

Zhang for help with STEM characterization..

Chapter 5, in part, is being prepared for submission for publication. Hao Shen, Dylan Lu, Bryan VanSaders, Jimmy J. Kan, Hongxing Xu, Eric E. Fullerton, and Zhaowei Liu, "Anomalously weak scattering in metal-semiconductor multilayer hyperbolic metamaterials." The dissertation author was the co-first author of this paper.

Chapter 6

Plasmonic metamaterials for solar energy harvesting

6.1 Introduction

Solar energy can potentially play a significant role in the global energy supply [134]. There are two main methods for generating electricity from sunlight: direct solar-electricity conversion using photovoltaic (PV) solar cells and concentrating solar power (CSP) which generates electricity from solar thermal energy [135]. Despite PV technology's rapid development, CSP still offers several unique advantages: higher energy-conversion efficiency, higher thermal energy storage capability (specifically, a higher capacity factor [136]), and the potential to retrofit current coal power plants. Therefore, large-scale deployment of CSP could enable a higher overall penetration of solar energy. As of 2011, the cumulatively installed CSP capacity reached ∼1.17 GW, and ∼17 GW of CSP is under development worldwide [137].

Among the various components in a CSP system, the solar absorber plays a critical role in overall system performance. To increase the Carnot efficiency of the power generation system, it is desirable that the temperature of the heat transfer fluid (HTF) is 600°C or higher [138]. In order to increase the temperature of the receiver, a solar absorber has to maximally absorb solar energy while minimizing

losses due to blackbody emission. At a receiver temperature of 500-800°C, blackbody emission peaks at wavelengths longer than 2 μm. Most energy within the solar spectrum is located at wavelengths below 2 μm, allowing for the possibility of optimizing receiver performance through tuning the spectral absorptivity (equivalent to spectral emissivity at equilibrium). As most materials do not naturally have the desired behavior, engineered composite metamaterials are needed.

In this chapter we describe a novel design for a high-performance spectrally selective coating (SSC), a critical component that enables high-temperature and high-efficiency operation of CSP systems, based on multi-scaled nanostructures. Optimal design of the new structure for high optical performance of the SSC is predicted by the effective medium theory. To demonstrate the feasibility of the design, we fabricate the SSCs using fractal nanostructures with characteristic sizes ranging from ∼10 nm to ∼10 μm. Optical measurements on these structures show unprecedentedly high performance with ∼90-95% solar absorptivity and <30% infrared emissivity near the peak of 500°C black body radiation. The newly developed concept of SSC could be utilized to design solar absorbers with high thermal efficiency for future high temperature CSP systems. Figure 6.1 (a) illustrates the schematic diagram of a solar absorber with a spectrally selective coating (SSC). An ideal SSC has to exhibit high spectral absorptivity, α_{S}, in the solar spectrum (wavelength, 0.3 μm to 2.0 μm), and low spectral emissivity, ϵ_{IR}, in the IR spectrum (wavelength, 2.0 μm to 15 μm) (Figure 6.1 (b)).

There has been an extensive search for mid- to high- temperature SSC materials. Typical SSC structures fall into one or several of the following schemes: 1. Intrinsic selective materials, the simplest structure usually in the form of thin films with proper intrinsic material selectivity [139]. 2. Semiconductor-metal tandems, which are made from semiconductors with proper bandgaps ($E_g \sim 0.5$ eV – 1.26 eV) that absorb solar radiation in tandem with an underlying metal that provides high IR reflectance. The main drawbacks of this structure include the need for an anti-reflection coating, oxidation of the semiconductors at elevated temperatures, and non-scalable processes for producing semiconductor thin films such as CVD [139] or vacuum sputtering. 3. Multilayer absorbers, which use multilayer stacks

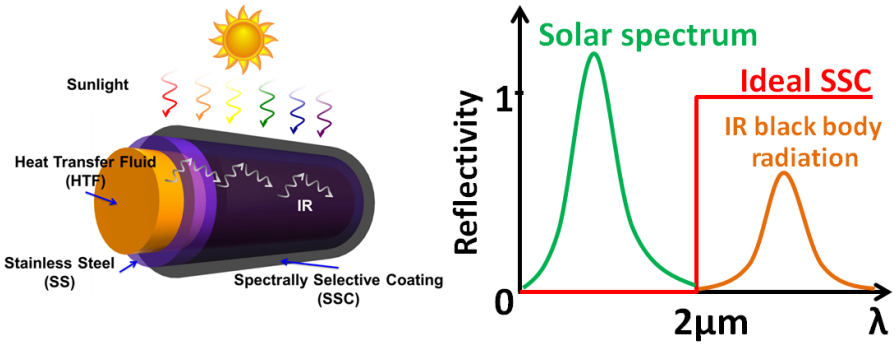

Figure 6.1: Spectrally selective coating (SSC) for concentrated solar power. (a) Schematic of a solar absorber with stainless steel (SS) tube coated with the SSC. (b) Optical reflectance of an ideal SSC. In the solar spectrum (short wavelength), the reflectance is zero (or the absorptance is 100%); in the IR spectrum, the reflectance is 100% (or the emittance is zero). Such an ideal SSC will have the maximum absorptance for solar energy but with minimal heat loss due to the blackbody IR thermal radiation of the absorber itself.

of metals and dielectrics to achieve high selectivity due to the interference effect. This scheme is limited by the high cost of the multi-stack fabrication process, such as sputtering and CVD [140, 141], as well as high-temperature instability [142]. 4. Textured surfaces, which consist of porous and nano-scale structures for the required spectral selectivity through optical trapping of sunlight [143]. The spectral emittance can be adjusted by modifying the microstructure of the coating. However, these highly textured metal surfaces tend to degrade quickly at elevated temperature [144, 145]. 5. Metal-dielectric composites, which utilize a highly solar-absorbent and IR-transparent material deposited onto a highly IR-reflective metal substrate. The "black" absorbing layer is a cermet of fine metal particles in a dielectric matrix [146, 147]. This design offers a very high degree of flexibility for tuning the absorption and scattering cutoff wavelengths by particle and matrix constituents, particle sizes and concentrations, coating thickness, etc.

Based on the above discussion, it is evident that an ideal and practical SSC material and scheme has yet to be identified [148]. Current SSCs typically have a high solar absorptivity but they either need high cost and vacuum processes, such as CVD and sputtering, or do not have a good spectral selectivity at around 1-2 μm. In addition, most SSC materials degrade after prolonged operation at high

temperatures, which is unsatisfactory for future CSP operation at high temperature ($\geq 700°C$). In this chapter, we demonstrated a high-performance SSC based on a novel design of multi-scaled semiconductor particles with sizes ranging from ~10 nm to ~10 μm. The micro/nano multi-scale structures, made from a low-cost and scalable coating process, were shown to yield high optical performance by both theoretical modeling and optical measurements.

6.2 Theoretical modeling and design calculation

The design of the multi-scaled SSC described in this chapter combines several features offered by the existing SSCs summarized above. As shown in Figure 6.2, our approach is based on semiconductor nanoparticles deposited on highly IR-reflective metal surfaces, which utilizes the concepts of the "intrinsic semiconductor", "textured surface" and "metal-dielectric composite" approaches. First, we employed a semiconductor material with a suitable band gap for the selectivity at around 1-2 μm wavelength, which is similar to the "intrinsic semiconductor" scheme. Secondly, we utilized multi-scale structures with a wide range of particle sizes in order to induce an appropriate surface morphology leading to higher light absorption. Since the multi-scaled nanostructures increase light trapping efficiency ("textured surfaces" scheme), there is no need for an additional anti-reflection coating layer. This is parallel to an extremely efficient anti-reflection coating in PV solar cells by using nanostructures to reduce the impedance mismatch and enhance light trapping [149]. However, our multi-scaled structures can be readily achieved by a simple coating process, which is more cost effective than previously reported methods [149] using lithography and etching processes in crystalline Si. Lastly, the composite structure of semiconductor powders and dielectric matrix reported here was inspired by the "metal-dielectric composite" concept that is flexible and versatile.

As a guideline for the fabrications of the SSC structures, we simulate optical properties of a SSC material that is comprised of nanoparticles embedded in a dielectric host with its representative cross-sectional view shown in Figure 6.2 (a).

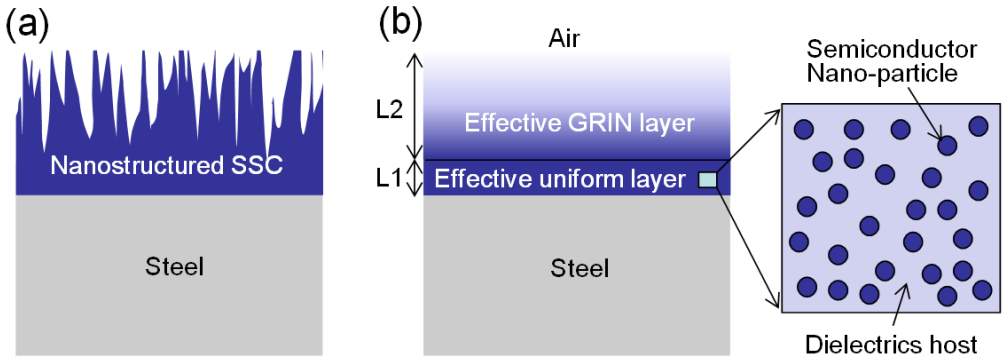

Figure 6.2: Optical modeling system for the SSC. The nanostructured SSC in (a) is modeled by a multilayer system consisting of a gradient refractive index layer with a thickness of L_2 and a uniform effective layer with a thickness of L_1 on the SS substrate as schematically shown in (b). The effective layer corresponds to the semiconductor nanoparticles in the dielectric host. The effective material properties can be described by the effective medium theory when the particle size is much smaller than the operation wavelengths.

An effective-medium-theory-based model was applied by approximating the nanostructured SSC to a two-layer geometry as shown in Figure 6.2 (b). The effective medium approximation treats the uniform nano-composite metamaterial (nanoparticles in the dielectric host) as an isotropic medium with a thickness of L_1 and an effective permittivity determined by the permittivities of individual components, i.e. ϵ_{p} for nanoparticles and ϵ_{h} for the dielectric host [37, 40, 89], and respective volumetric ratios. The surface-structured metamaterial with a thickness of L_2 can thus be treated as a gradient-refractive-index (GRIN) layer mixed between the uniform metamaterials and air. The GRIN layer is modeled by discretizing the material into infinitesimally thin layers in the vertical direction, each of which may be considered as a uniform medium. Determined by the particle filling ratio of the coating, the effective dielectric function for both uniform and GRIN layers follows the Maxwell-Garnett formalism or the Bruggeman mixing theory [40]. The GRIN layer gradually smoothes out the permittivity discontinuity between air and the uniform metamaterial layer, thus serving as a perfect anti-reflection layer.

The reflectance of the total structure can be calculated using a transfer matrix method once the effective permittivities are known [46]. Figure 6.3 (a) shows numerically simulated reflectance spectra of the SSC with different nanoparticle

filling ratios at normal incidence based on the Bruggeman mixing theory. In the simulation, the uniform metamaterial layer is assumed to be made of intrinsic Si nanoparticles embedded in a SiO_2 host, with the corresponding permittivities taken from refs. [42] and [41]. The GRIN layer is divided into 100 individual uniform layers with effective permittivities varying smoothly from air to that of the bulk layer. When the particle filling ratio exceeds 50%, a sharp change is observed in the reflectance spectra of the simulated coating near wavelengths of 1.1 μm, corresponding to the bandgap of Si. Figure 6.3 (b) shows a reflectance curve (blue line) when the Si filling ratio is 75% as compared with the standard solar spectrum and the blackbody radiation spectrum at 700°C. The comparison indicates that the solar absorptivity for the SSC device is close to 99% while its IR emissivity is about 4%. It is worth noting that the optical properties of the SSC layer with different semiconductor and dielectric combinations are always similar, except that the cutoff wavelengths may shift according to the bandgap of the semiconductor. The reflectance curve (green line) for the SiGe with a same filling ratio of 75% in a SiO_2 host indicates that the cutoff wavelength shifts to a longer wavelength with composition change.

From the calculations, it is clear that the following factors are the primary causes of the overall high performance. Firstly, the effective GRIN layer acts as a perfect light trapping or anti-reflection layer. In practice, the Bruggeman mixing theory used here will be a valid approximation when features of the layer are sub-wavelength to incident radiation (<300 nm for visible light). Secondly, an appropriate nanoparticle material and its volumetric filling ratio are the key parameters for tuning the cutoff wavelength in the reflectance spectra. Lastly, a smooth steel layer underneath improves reflectance at IR wavelengths. The surface roughness of steel should be deep sub-wavelength at IR frequencies (typically <100 nm) to reduce the IR absorption due to surface light trapping. As shown in Figure 6.4, the calculated reflectance is almost invariant to light polarizations and incident angles, indicating the robustness of the SSC layer.

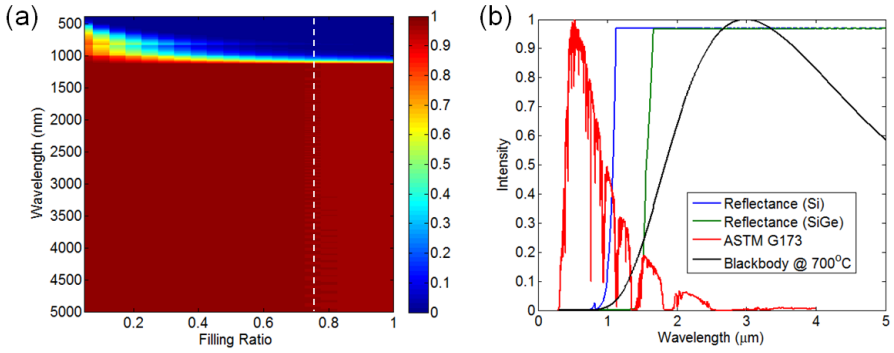

Figure 6.3: Numerical simulation results of the reflectance spectra for the SSC. (a) Reflectance with respect to incident wavelengths and the volumetric filling ratios of the nanoparticles where the incident angle is fixed at 0 degree (normal incidence). The materials of the nanoparticles and dielectric host are Si and SiO_2, respectively. $L_1 = 20$ μm, $L_2 = 10$ μm. (b) Reflectance of the SSC layer when the filling ratio of the nanoparticles is equal to 0.75 (blue line), i.e., at the location marked by the dashed vertical line in (a). Reflectance of the SSC layer (green) made of SiGe (volumetric filling ratio of Si in SiGe, 80%) in SiO_2 host with the same nanoparticle filling ratio, normalized standard solar spectrum in red and the blackbody radiation at 700°C in black are also added for comparison.

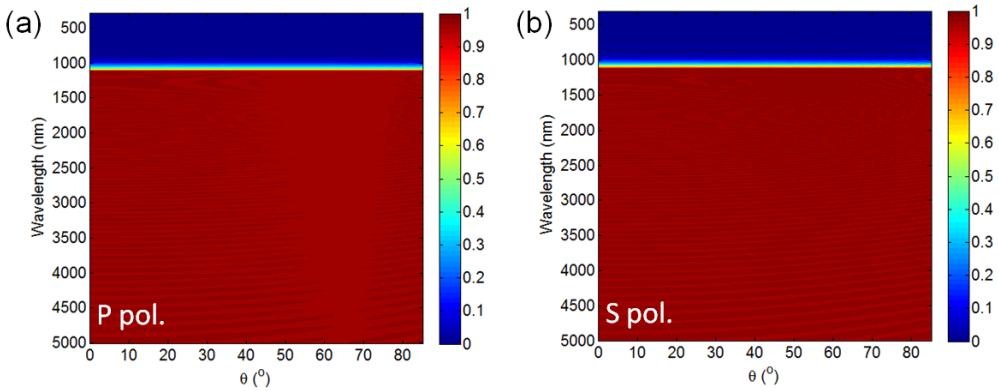

Figure 6.4: Numerical simulation results of the reflectance spectra with respect to different incident wavelengths and collection angles when the volumetric filling ratio of the nanoparticles is fixed at 0.75. All other parameter settings are identical to those calculated Figure 6.3 (a). (a) P-polarized waves; (b) S-polarized waves.

6.3 Experimental demonstration

6.3.1 Fabrication of multi-scaled SSCs

To validate the new design, we used $Si_{0.8}Ge_{0.2}$ as a representative semiconductor material to fabricate SSCs. $Si_{0.8}Ge_{0.2}$ is expected to yield the desirable light absorptivity in VIS-NIR range (<1 μm) due to the intrinsic bandgap of $Si_{0.8}Ge_{0.2}$, ~1.04 eV [150]. The $Si_{0.8}Ge_{0.2}$ powders of various sizes were prepared by a spark erosion process. Following spark erosion, attrition milling was carried out with the spark eroded $Si_{0.8}Ge_{0.2}$ particles for optimizing the particle size distribution to increase the proportion of powders of several hundred nanometers, which are strong scatterers of the range of incident light wavelengths. The as-made $Si_{0.8}Ge_{0.2}$ particles were dispersed into an organic solvent, and the solution was sonicated to make a uniform mixture. Concentration of the solutions was controlled and kept consistent. The nanoparticle solution was then coated onto targeted stainless steel substrates by drop casting. After the solvent dried, a coating film made of $Si_{0.8}Ge_{0.2}$ particles was formed on the stainless steel substrate (Figure 6.5 (a-b)). The film thickness was controlled to ~100 μm by adjusting the drop casting conditions. In order to demonstrate the effect of particle-size distribution, ~100-μm-thick films made from commercial Si powders (Alfa Aesar) with average diameter of ~100 nm were also prepared using the same process (Figure 6.5 (c-d)).

We also performed brief high temperature tests for the SiGe coating at 750°C for 1 hour in air environment. The particular condition was chosen because 750°C is higher than the current operation temperature of the high temperature CSP (550°C) but lower than the melting point of $Si_{0.8}Ge_{0.2}$ (~1270°C). Even though this material can be used in a vacuum enclosure, the oxidation resistance is also desired in case the vacuum was unintentionally breached.

The fabricated SSC samples were characterized by SEM. Figure 6.5 (a-b) show top-view SEM images of the SSC layer made by using spark-eroded SiGe particles. After deposition, micro-scale dome-shaped structures are built up by micro-sized spark-eroded particles. These micro-scale particles are covered with nano-scale powders as shown in Figure 6.5 (b), thus creating the multi-scale fea-

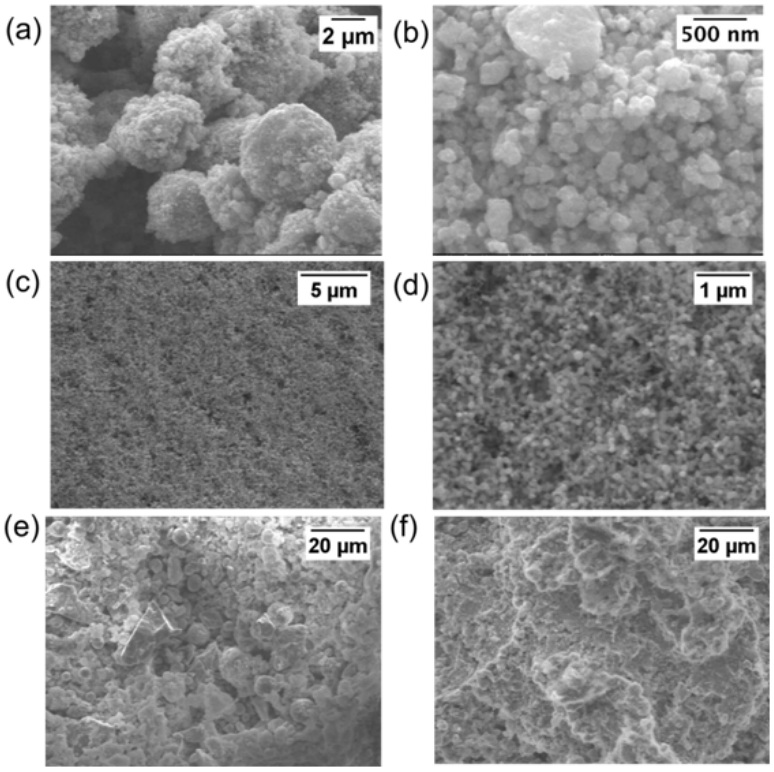

Figure 6.5: Characterization of the SSCs. (a-b) SEM images of the SSC based on spark-eroded $Si_{0.8}Ge_{0.2}$ particles. (c-d) SEM images of the SSC made by ∼100 nm Si nanoparticles. SEM images of the same Si-Ge sample (e) before and (f) after annealing at 750°C in air for 1 hour.

tures. Unlike spark-eroded Si-Ge particles, the top surface of the Si coating is quite smooth except for the roughness at the particle size scale as shown in Figure 6.5 (c-d). Figure 6.5 (e-f) show the SEM images of the same SSC before and after annealing at 750°C for 1 hour in air, respectively. It is evident that the morphology of the SSC remains similar after the annealing test.

6.3.2 Optical characterization of multi-scaled SSCs

The optical reflectance of the SSCs was measured by a UV-VIS spectrometer and directional emission at a temperature of 500°C measured in a Fourier transform infrared (FTIR) spectrometer, with the results presented in Figure 6.6 (a) and (b), respectively. To characterize the SSCs in the UV-VIS range, incident light from Xenon lamp was focused onto the sample surface which was contained within an integration sphere capable of collecting all angles of scattered light. Collected spectra were analyzed by an ANDOR^{TM} Shamrock 303i spectrograph equipped with a Newton 920 CCD detector. High temperature IR emittance was characterized by an FTIR spectrometer (Mattson Galaxy5020) with custom built heated sample stage. The samples were kept under vacuum during measurement to reduce heat loss, and a maximum temperature of samples reached 500°C. A sample of Pyromark 2500 (Tempil) was used as a standard reference for the measurement, with directional emissivity data taken from ref. [151]. As shown in Figure 6.6 (a), the multi-scaled SSC layers made from the spark-eroded powders have low reflectivity of 5%-10% across the UV-NIR solar spectrum. In contrast, the SSC made from uniform Si nanoparticles shows much higher reflectivity (13%-80%). This demonstrates the high light-trapping efficiency of the multi-scaled structures: if the particles are all micro-sized, light will be reflected from the surface of large particles; on the other hand, if the particles are all nano-sized, the uniform surface of the SSC layer will result in inefficient light trapping, as in the case of the control sample made by 100 nm Si nanoparticles. Similar multi-scaled structure has been achieved using lithographic patterning for enhanced light absorption in PV devices [149, 152, 153]. In addition to the light trapping effect, the lower bandgap of Si-Ge particles enables more absorption than Si particles in the spectrum range

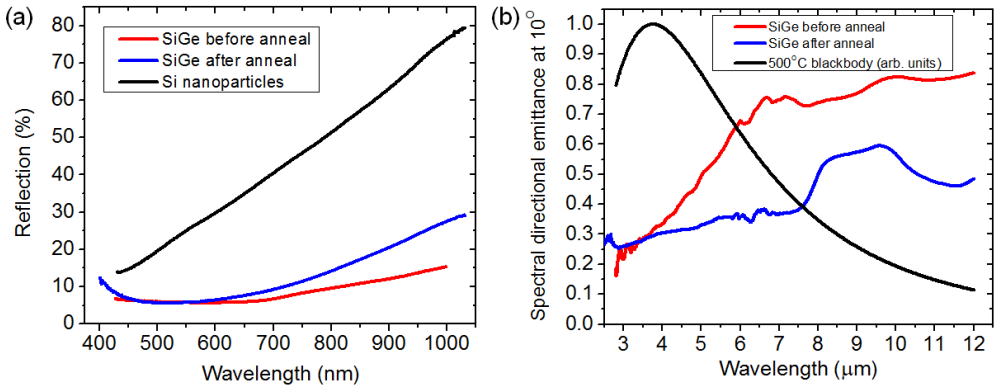

Figure 6.6: (a) Measured reflectance of the SSCs in the UV to near-IR regime. (b) Measured IR emission spectra at 500°C. The black curve in (b) is the normalized blackbody spectrum at 500°C.

below bandgap of Si-Ge (∼1.2 μm). And in the aspect of mass production, the approach we developed is based on multi-scaled particles naturally formed during the spark-erosion process and the following attrition milling, and hence is more readily applicable for large-scale applications such as CSP.

Figure 6.6 (b) shows the directional spectral emittance of SiGe SSC layers at IR frequencies. Rough surfaces generally display isotropic (Lambertian) scattering and we can therefore expect the presented data to be representative of all-angle emission spectra. The SiGe sample shows low emission below 0.3 near the peak of 500°C blackbody radiation which stems from the low absorption coefficient obtained by the light with energy below the bandgap of $Si_{0.8}Ge_{0.2}$ (∼1.04 eV or 1.2 μm). The discrepancy between simulated (Figure 6.3 (b)) and experimental emission spectra at IR is mainly attributed to the excitation of considerable hot carriers at elevated temperature.

We also evaluated the potential of the multi-scaled structural SSCs for high temperature operation (≥700°C). The blue curves in Figure 6.6 (a) and (b) show the reflectance of the SiGe SSC sample after annealing at 750°C for 1 hour in air. Even though $Si_{0.8}Ge_{0.2}$ can be oxidized at high temperature in air environment, we observed the annealed sample exhibited a small increase in the reflectance in the UV-VIS-NIR range. This coincides with the structural observation showing minimal morphological and structural changes of the particles after the annealing

(Figure 6.5 (e-f)).

6.4 Discussion

The demonstrated multi-scaled SSC provides a promising conceptual example for application in future CSP system. However, a high-performance SSC for CSP systems has to show not only good energy conversion efficiency but also high-temperature endurance. The measured solar absorption is so far 90-95%. Further optimization of the coating, including material selection, particle size distribution, and coating morphology, is likely to reduce the solar reflectivity further, as shown in our simulation results (Figure 6.3). The optimal parameters such as the particle size range and distribution warrant further investigation. On the other hand, annealed sample exhibited a small reflectance increase in the UV-VIS-NIR range, which requires a comprehensive study and oxidation degradation be conducted in the next step to improve high temperature stability. A systematic high temperature durability tests as well as oxidation protective coating need to be performed to evaluate the applicability of the new SSC for future CSP systems. Meanwhile, the application of high temperature durable materials having appropriate band gaps, such as conductive oxides, will be a promising approach.

6.5 Conclusion

In conclusion, We reported the design and fabrication of a new SSC structure based on multi-scaled semiconductor nanostructures. The SiGe SSC is highly absorbent for short-wavelength photons (with energy higher than the semiconductor bandgap) and efficiently reflective for long-wavelength photons. The measured spectral solar reflectance (5%-10%) and IR emissivity (<30%) of the SSC indicate high performance for CSP applications. We also found that the multi-scale features (10 nm $\sim$ 10 μm) of the particles have significantly enhanced the solar absorptivity compared to uniform nanoparticles due to the more efficient light trapping. The particles and the SSC are made by spark erosion and low-cost drop casting

process, which is applicable for making large-scale solar absorbers. We anticipate the high solar absorptance and low IR emittance of the developed SSC will significantly benefit future high temperature CSP technologies by improving their maximum attainable temperature and thermal efficiency. In addition, the SSC shows the potential to maintain the multi-scale structure and optical properties after high temperature process. Further applications of the multi-scaled structure on high temperature materials and systematic high temperature durability tests will be performed to evaluate the applicability of the new SSC for future high temperature CSP systems.

This work is supported by the US Department of Energy, SunShot Program Contract No. DE-EE005802.

Chapter 6, in part, is a reprint of the material as it appears on Nano Energy 8, 238-246 (2014). Jaeyun Moon, Dylan Lu, Bryan VanSaders, Tae Kyoung Kim, Seong Deok Kong, Sungho Jin, Renkun Chen, and Zhaowei Liu, "High performance multi-scaled nanostructured spectrally selective coating for concentrating solar power." The dissertation author was the co-first author of this paper.

Chapter 7

Summary and future directions

7.1 Thesis summary

In this thesis, we demonstrated plasmonic metamaterials with tunable plasmonic properties, and their applications in controlling spontaneous emission process of quantum emitters, and manipulating light propagation, scattering and absorption.

Composite metamaterials and multilayer metamaterials were introduced as promising alternatives to existing plasmonic materials for providing tunable plasmonic properties in many applications. We demonstrate modified optical properties in composite metamaterials by adding additional dielectrics or semiconductors into bulk Ag. Angular-resolved reflection spectra in the Fourier space at different wavelengths were obtained for Ag-SiO_2 and Ag-Si composite films and fitted by a theoretical model. Effective material properties of such composite films were therefore retrieved and tunable SPP dispersions were present. On the other hand, the working wavelength of multilayer metamaterials was proved to be tunable across a broad band of wavelengths by optimized combination of materials and filling ratios. Ag-Al_2O_3 and high-quality ultrathin Ag-Si and Au-Si multilayer metamaterials were fabricated and their optical responses were characterized.

Nanopatterned multilayer metamaterials with hyperbolic dispersion relations were further utilized for controlling the process of light emission. Both strongly enhanced spontaneous emission rates and improved radiative emission

into the far field from molecules on such multilayer substrates were investigated theoretically and demonstrated experimentally at desired frequencies through the Purcell effect. A tunable broadband Purcell enhancement of 76 fold on the Ag-Si HMMs was measured by time-resolved photoluminescence and the emission intensity improvement of 80 fold was achieved by the out-coupling effect of nanopatterned structures. The performance dependence of multilayer metamaterials on the geometry was also discussed.

This concept of metamaterial enhanced light emission was later applied to GaN quantum-well light emitting devices for improving both the light efficiency and modulation speed at blue and green wavelengths. Based on detailed numerical designs, Ag-based plasmonic nanostructures were incorporated into blue LEDs and the strongly improved electrically-pumped light emitting intensity was optically characterized. Ag-Si multilayer HMMs were nanopatterned onto the green QWs and time-resolved photoluminescence measured close to 60-fold spontaneous emission rate enhancement corresponding to potentially a 3 dB modulation speed of $\sim$9.3 GHz.

On the passive light manipulation, we demonstrated the control of scattering by engineering the material properties of anisotropic multilayer-based metamaterials. In contrast to strong plasmonic scattering from metal Au patterns, an anomalously weak scattering by patterns in Au-Si multilayer HMMs was observed and experimentally demonstrated to be insensitive to pattern sizes, shapes and incident angles, and by changing the filling ratios of constituent materials it is possible to tune AWS behavior to desired optical wavelengths.

Lastly, the concept of metamaterials was also extended to selective control of light absorption and reflection for potential solar energy applications. A high-performance spectrally selective coating based on multi-scaled metamaterials was designed and fabricated with 90%-95% solar absorptivity and $<$30% infrared emissivity near the peak of 500°C black body radiation, which can be utilized for designing solar absorbers with high thermal efficiency for future high temperature concentrating solar power systems.

7.2 Future directions

This thesis focused on part of interesting properties and useful functionalities of plasmonic metamaterials. A lot more unknown fundamental properties and possible directions are worth of exploration. Towards the end of the thesis, I am bringing up a few prospective future work either following the existing projects or inspiring new research interests.

The plasmonic enhancement of QW LEDs was demonstrated so far for the electrically-pumped light emission intensity enhancement at blue wavelengths and the optically-pumped spontaneous emission rate enhancement at green wavelengths, respectively, in Chapter 4. Although it provided preliminary support for the feasibility of bright high-speed LED enabled by plasmonic metamaterials, it is still more desirable to demonstrate an ultrafast direct electrical modulated plasmonc LED to a few GHz. Due to a relatively simpler integration, Ag plasmonic metamaterial enhanced LED at blue wavelength is more straightforward for electrical pumping. First, the thickness of p-GaN layer and location of Ag plasmonic materials have to be designed well to balance the requirement for adequate p-type carriers and the strong enough plasmonic interaction. Second, when dealing with high-speed electro-optics, an electrical probe that supports high-frequency modulated signal and strong enough input power has to be employed. On-chip circuit patterns have also to be designed to support propagation of high-speed RF signal to ensure an efficient portion of power has been delivered to the QW area. Third, the dynamics of electron-hole carriers at high modulation speed may have to be analyzed. And the heat sink has to be managed well since the Purcell enhancement quickly drops as the internal quantum efficiency decreases at elevated temperatures.

On the other hand, the characterization of multilayer enhanced green QWs can be more complete if the wavelength dependent lifetimes could be mapped out. This will be enabled by incorporating a monochrometer into the current time-correlated single photon counting system. Lifetime wavelength mapping could provide us deep understanding of the Purcell interaction and guide the systematic design. Moreover, the electrical version of multilayer HMM LEDs is promising

despite the complexity of multilayer incorporation into the QW LED with p-GaN layer. With both blue and green high-speed LEDs, the concept of tunable Purcell enhancement will be well proved.

EM wave control by metamaterials has always been one of the important topics in this area. Not only anomalously weak scattering can be realized in multilayer HMMs as discussed in Chapter 5, but also superscattering [128] is expected from individual scatters made of multilayer HMMs. The scattering properties of individual scatters made of multilayer HMMs compared with pure metal is another interesting topic. Due to the large density of states in HMMs, careful engineering of the composition and geometry of individual HMM scatter will align different modes, leading to much stronger scattering than pure metal. Such super HMM scatters may find applications in further improving light emission intensity when combined with molecules or QW LEDs. Their enhancement of Raman signal is another promising direction to work on.

All possible new physics phenomena and applications depend on the material properties of plasmonic metamaterials. The multilayer metamaterials we utilized so far still have nonnegligible loss in the optical wavelengths. HMMs with lower loss will significantly improve their plasmonic performance. To achieve low loss HMMs, promising approaches combine new material system [154] and higher quality growth technique, such as epitaxial growth. Higher quality new material based HMMs may endure high temperature, and therefore could be utilized in the thermal radiation applications. Recent proposed super-Planckian thermal emission postulate HMMs with high density of states could break the blackbody limit [155, 156].

Another direction as an extension of existing plasmonic metamaterials is to a length scale where classical EM theory or effective medium theory are no longer valid and quantum description of the metamaterial properties has to be taken into account. The quantum nature takes place when either the size of [157] or the spacing between [158] plasmonic metamaterials is small enough. The multilayer based metamaterials are good candidate for investigating such quantum properties by reducing the layer thickness. Effective medium theory used in this thesis will

no longer be valid, and a quantum version of effective medium theory may be developed. Quantization of energy levels in such system will lead to unprecedented material properties, rewriting the story of plasmonic metamaterials for active and passive light control.

Bibliography

[1] H. R. Raether. *Surface Plasmons on Smooth and Rough Surfaces and on Gratings*. Springer, New York, 1988.

[2] Mark L. Brongersma and Pieter G. Kik. *Surface Plasmon Nanophotonics*. Springer, Dordrecht, 2007.

[3] Jon A. Schuller, Edward S. Barnard, Wenshan Cai, Young Chul Jun, Justin S. White, and Mark L. Brongersma. Plasmonics for extreme light concentration and manipulation. *Nature Materials*, 9:193–204, 2010.

[4] Stefan A. Maier. *Plasmonics: Fundamentals and Applications*. Springer Science+Business Media LLC, New York, 2007.

[5] T. W. Ebbesen, H. J. Lezec, H. F. Ghaemi, T. Thio, and P. A. Wolff. Extraordinary optical transmission through sub-wavelength hole arrays. *Nature*, 391(6668):667–669, 1998.

[6] Stefan A. Maier, Pieter G. Kik, Harry A. Atwater, Sheffer Meltzer, Elad Harel, Bruce E. Koel, and Ari A.G. Requicha. Local detection of electromagnetic energy transport below the diffraction limit in metal nanoparticle plasmon waveguides. *Nature Materials*, 2:229, 2003.

[7] Nicholas Fang, Hyesog Lee, Cheng Sun, and Xiang Zhang. Sub-diffraction-limited optical imaging with a silver superlens. *Science*, 308:534–537, 2005.

[8] Zhaowei Liu, Stephane Durant, Hyesog Lee, Yuri Pikus, Nicolas Fang, Yi Xiong, Cheng Sun, and Xiang Zhang. Far-field optical superlens. *Nano Lett.*, 7(2):403–408, 2007.

[9] Gerasimos Konstantatos and Edward H. Sargent. Nanostructured materials for photon detection. *Nature Nanotechnology*, 5:391, 2010.

[10] Liang Tang, Sukru Ekin Kocabas, Salman Latif, Ali K. Okyay, Dany-Sebastien Ly-Gagnon, Krishna C. Saraswat, and David A. B. Miller. Nanometre-scale germanium photodetector enhanced by a near-infrared dipole antenna. *Nature Photonics*, 2:226, 2008.

[11] Ekmel Ozbay. Plasmonics: Merging photonics and electronics at nanoscale

dimensions. *Science*, 311:189, 2006.

[12] Kevin F. MacDonald, Zsolt L. Samson, Mark I. Stockman, and Nikolay I. Zheludev. Ultrafast active plasmonics. *Nature Photonics*, 3:55, 2009.

[13] Koichi Okamoto, Isamu Niki, Alexander Shvartser, Yukio Narukawa, Takashi Mukai, and Axel Scherer. Surface-plasmon-enhanced light emitters based on ingan quantum wells. *Nature Materials*, 3:601–605, 2004.

[14] Anika Kinkhabwala, Zongfu Yu, Shanhui Fan, Yuri Avlasevich, Klaus-MuÂĺllen, and W. E. Moerner. Large single-molecule fluorescence enhancements produced by a bowtie nanoantenna. *Nature Photonics*, 3:654–657, 2009.

[15] H. A. Atwater and A. Polman. Plasmonics for improved photovoltaic devices. *Nature Materials*, 9(3):205–213, 2010.

[16] S. Linic, P. Christopher, and D. B. Ingram. Plasmonic-metal nanostructures for efficient conversion of solar to chemical energy. *Nature Materials*, 10:911–921, December 2011.

[17] J. B. Pendry, A. J. Holden, W. J. Stewart, and I. Youngs. Extremely low frequency plasmons in metallic mesostructures. *Phys. Rev. Lett.*, 76:4773, 1996.

[18] D. R. Smith, S. Schultz, P. Markos, and C. M. Soukoulis. Determination of effective permittivity and permeability of metamaterials from reflection and transmission coefficients. *Phys. Rev. B*, 65:195104, 2002.

[19] R. A. Shelby, D. R. Smith, and S. Schultz. Experimental verification of a negative index of refrraction. *Science*, 292:77–79, 2001.

[20] J. Yao, Z. W. Liu, Y. M. Liu, Y. Wang, C. Sun, G. Bartal, A. M. Stacy, and X. Zhang. Optical negative refraction in bulk metamaterials of nanowires. *Science*, 321(5891):930, 2008.

[21] J. Valentine, S. Zhang, T. Zentgraf, E. Ulin-Avila, D. A. Genov, G. Bartal, and X. Zhang. Three-dimensional optical metamaterial with a negative refractive index. *Nature*, 455:376–379, September 2008.

[22] Nikolay I. Zheludev and Yuri S. Kivshar. From metamaterials to metadevices. *Nature Materials*, 11:917–924, 2012.

[23] J. B. Pendry, D. Schurig, and D. R. Smith. Controlling electromagnetic fields. *Science*, 312(5781):1780–1782, 2006.

[24] U. Leonhardt. Optical conformal mapping. *Science*, 312(5781):1777–1780, 2006.

[25] D. Schurig, J. J. Mock, B. J. Justice, S. A. Cummer, J. B. Pendry, A. F. Starr, and D. R. Smith. Metamaterial electromagnetic cloak at microwave frequencies. *Science*, 314(5801):977–980, 2006.

[26] J. Valentine, J. S. Li, T. Zentgraf, G. Bartal, and X. Zhang. An optical cloak made of dielectrics. *Nature Materials*, 8(7):568–571, 2009.

[27] J. B. Pendry. Negative refraction makes a perfect lens. *Phys. Rev. Lett.*, 85:3966, 2000.

[28] Zhaowei Liu, Hyesog Lee, Yi Xiong, Cheng Sun, and Xiang Zhang. Far-field optical hyperlens magnifying sub-diffraction-limited objects. *Science*, 315:1686–1701, 2007.

[29] J. Rho, Z. L. Ye, Y. Xiong, X. B. Yin, Z. W. Liu, H. Choi, G. Bartal, and X. Zhang. Spherical hyperlens for two-dimensional sub-diffractional imaging at visible frequencies. *Nature Communications*, 1:143, 2010.

[30] S. Han, Y. Xiong, D. Genov, Z. W. Liu, G. Bartal, and X. Zhang. Ray optics at a deep-subwavelength scale: a transformation optics approach. *Nano Letters*, 8(12):4243–4247, 2008.

[31] Y. Xiong, Z. W. Liu, and X. Zhang. A simple design of flat hyperlens for lithography and imaging with half-pitch resolution down to 20 nm. *Applied Physics Letters*, 94(20):203108, 2009.

[32] Uwe Kreibig and M. Vollmer. *Optical properties of metal clusters*. Springer-Verlag, New York, 1995.

[33] V. M. Shalaev. Optical negative-index metamaterials. *Nature Photonics*, 1:41, 2007.

[34] M. Gaudry, Lerm, eacute, J., E. Cottancin, M. Pellarin, J. L. Vialle, M. Broyer, Pr, B. vel, M. Treilleux, and P. linon. Optical properties of $(Au_xAg_{1-x})_n$ clusters embedded in alumina: Evolution with size and stoichiometry. *Physical Review B*, 64(8):085407, 2001.

[35] D. Y. Lei, J. Li, and H. C. Ong. Tunable surface plasmon mediated emission from semiconductors by using metal alloys. *Appl. Phys. Lett.*, 91:021112, 2007.

[36] V. M. Shalaev. *Nonlinear Optics of Random Media: Fractal Composites and Metal-Dielectric Films*. Springer, Berlin Heidelberg, 2000.

[37] Wenshan Cai, Dentcho A. Genov, and Vladimir M. Shalaev. Superlens based on metal-dielectric composites. *Phys. Rev. B*, 72:193101, 2005.

[38] R. B. Nielsen, M. D. Thoreson, W. Chen, A. Kristensen, J. M. Hvam, V. M.

Shalaev, and A. Boltasseva. Toward superlensing with metal-dielectric composites and multilayers. *Appl. Phys. B*, 100:93, 2010.

[39] W. Chen, M. D. Thoreson, A. V. Kildishev, and V. M. Shalaev. Fabrication and optical characterizations of smooth silver-silica nanocomposite films. *Laser Phys. Lett.*, 7(9):677, 2010.

[40] Jordi Sancho-Parramon, Vesna Janicki, and Hrvoje Zorc. On the dielectric function tuning of random metal-dielectric nanocomposites for metamaterial applications. *Opt. Express*, 18:26915, 2010.

[41] Marvin.J. Weber. *Handbook of Optical Materials*. CRC Press, 2003.

[42] D. E. Aspnes and A. A. Studna. Dielectric functions and optical parameters of si, ge, gap, gaas, gasb, inp, inas, and insb from 1.5 to 6.0 ev. *Physical Review B*, 27(2):985, 1983.

[43] P. B. Johnson and R. W. Christy. Optical constants of the noble metals. *Phys. Rev. B*, 6:4370, 1972.

[44] A. Hilger, M. Tenfelde, and U. Kreibig. Silver nanoparticles deposited on dielectric surfaces. *Appl. Phys. B*, 73:361, 2001.

[45] A. Pinchuk, U. Kreibig, and A. Hilger. Optical properties of metallic nanoparticles: influence of interface effects and interband transitions. *Surface Science*, 557:269, 2004.

[46] Pochi Yeh. *Optical Waves in Layered Media*. Wiley, Hoboken, NJ, 2005.

[47] S. Anantha Ramakrishna, J. B. Pendry, M. C. K. Wiltshire, and W. J. Stewart. Imaging the near field. *Journal of Modern Optics*, 50:1419–1430, 2003.

[48] William L. Barnes, Alain Dereux, and Thomas W. Ebbesen. Surface plasmon subwavelength optics. *Nature*, 424:824–830, 2003.

[49] K. T. Shimizu, W. K. Woo, B. R. Fisher, H. J. Eisler, and M. G. Bawendi. Surface-enhanced emission from single semiconductor nanocrystals. *Physical Review Letters*, 89(11):117401, 2002.

[50] P. Anger, P. Bharadwaj, and L. Novotny. Enhancement and quenching of single-molecule fluorescence. *Physical Review Letters*, 96(11):113002, 2006.

[51] Chang-Hee Cho, Carlos O. Aspetti, Michael E. Turk, James M. Kikkawa, Sung-Wook Nam, and Ritesh Agarwal. Tailoring hot-exciton emission and lifetimes in semiconducting nanowires via whispering-gallery nanocavity plasmons. *Nature Materials*, 10:669–675, 2011.

[52] H. G. Frey, S. Witt, K. Felderer, and R. Guckenberger. High-resolution

imaging of single fluorescent molecules with the optical near-field of a metal tip. *Physical Review Letters*, 93(20):200801, 2004.

[53] Ziyang Ma, Jordan M. Gerton, Lawrence A. Wade, and Stephen R. Quake. Fluorescence near-field microscopy of dna at sub-10 nm resolution. *Phys. Rev. Lett.*, 97:260801, 2006.

[54] T. H. Taminiau, F. D. Stefani, F. B. Segerink, and N. F. Van Hulst. Optical antennas direct single-molecule emission. *Nature Photonics*, 2(4):234–237, 2008.

[55] E. Fort and S. Gresillon. Surface enhanced fluorescence. *Journal of Physics D-Applied Physics*, 41(1):013001, 2008.

[56] S. M. Nie and S. R. Emery. Probing single molecules and single nanoparticles by surface-enhanced raman scattering. *Science*, 275(5303):1102–1106, 1997.

[57] Eric C. Le Ru and Pablo G. Etchegoin. *Principles of Surface-Enhanced Raman Spectroscopy: and related plasmonic effects*. Elsevier, Amsterdam, The Netherlands, 2009.

[58] J. R. Lakowicz. Radiative decay engineering 5: metal-enhanced fluorescence and plasmon emission. *Analytical Biochemistry*, 337(2):171–194, 2005.

[59] P. Lodahl, A. F. van Driel, I. S. Nikolaev, A. Irman, K. Overgaag, D. Vanmaekelbergh, and W. L. Vos. Controlling the dynamics of spontaneous emission from quantum dots by photonic crystals. *Nature*, 430(7000):654–657, 2004.

[60] S. Noda, M. Fujita, and T. Asano. Spontaneous-emission control by photonic crystals and nanocavities. *Nature Photonics*, 1(8):449–458, 2007.

[61] G. Shambat, B. Ellis, A. Majumdar, J. Petykiewicz, M. A. Mayer, T. Sarmiento, J. Harris, E. E. Haller, and J. Vuckovic. Ultrafast direct modulation of a single-mode photonic crystal nanocavity light-emitting diode. *Nature Communications*, 2:539, 2011.

[62] E.M. Purcell. Spontaneous emision probabilities at radio frequencies. *Phys. Rev.*, 69:681, 1946.

[63] J. P. Reithmaier, G. Sek, A. Loffler, C. Hofmann, S. Kuhn, S. Reitzenstein, L. V. Keldysh, V. D. Kulakovskii, T. L. Reinecke, and A. Forchel. Strong coupling in a single quantum dot-semiconductor microcavity system. *Nature*, 432(7014):197–200, 2004.

[64] Volker J. Sorger, Nitipat Pholcha, Ertugrul Cubukcu, Rupert F. Oulton, Pavel Kolchin, Christian Borschel, Martin Gnauck Carsten Ronning, and Xiang Zhang. Strongly enhanced molecular fluorescence inside a nanoscale

waveguide gap. *Nano Lett.*, 11(11):4907–4911, 2011.

[65] M. Bayer, T. L. Reinecke, F. Weidner, A. Larionov, A. McDonald, and A. Forchel. Inhibition and enhancement of the spontaneous emission of quantum dots in structured microresonators. *Phys. Rev. Lett.*, 86:3168, 2001.

[66] G. S. Solomon, M. Pelton, and Y. Yamamoto. Single-mode spontaneous emission from a single quantum dot in a three-dimensional microcavity. *Physical Review Letters*, 86(17):3903–3906, 2001.

[67] G.W. Ford and W.H Weber. Electromagnetic interactions of molecules with metal surfaces. *Physics Reports*, 113(4):195–287, 1984.

[68] W.L. Barnes. Fluorescence near interfaces: the role of photonic mode density. *Journal of Modern Optics*, 45(4):661–699, 1998.

[69] Xiang Zhang and Zhaowei Liu. Superlenses to overcome the diffraction limit. *Nature Materials*, 7:435–441, 2008.

[70] Dylan Lu and Zhaowei Liu. Hyperlenses and metalenses for far-field superresolution imaging. *Nature Communications*, 3:1205, 2012.

[71] C. L. Cortes, W. Newman, S. Molesky, and Z. Jacob. Quantum nanophotonics using hyperbolic metamaterials. *Journal of Optics*, 14(6):063001, 2012.

[72] Z. Jacob and V. M. Shalaev. Plasmonics goes quantum. *Science*, 334(6055):463–464, 2011.

[73] H. N. S. Krishnamoorthy, Z. Jacob, E. Narimanov, I. Kretzschmar, and V. M. Menon. Topological transitions in metamaterials. *Science*, 336(6078):205–209, 2012.

[74] Z. Jacob, I. I. Smolyaninov, and E. E. Narimanov. Broadband purcell effect: Radiative decay engineering with metamaterials. *Applied Physics Letters*, 100(18):181105, 2012.

[75] Xiaodong Yang, Jie Yao, Junsuk Rho, Xiaobo Yin, and Xiang Zhang. Experimental realization of three-dimensional indefinite cavities at the nanoscale with anomalous scaling laws. *Nature Photonics*, 6:450–454, 2012.

[76] Yanxia Cui, Kin Hung Fung, Jun Xu, Hyungjin Ma, Yi Jin, Sailing He, and Nicholas X. Fang. Ultrabroadband light absorption by a sawtooth anisotropic metamaterial slab. *Nano Lett.*, 12(3):1443–1447, 2012.

[77] Z. Jacob, J.-Y. Kim, G.V. Naik, A. Boltasseva, E.E. Narimanov, and V. M. Shalaev. Engineering photonic density of states using metamaterials. *Appl. Phys. B*, 100:215, 2010.

[78] X. Ni, G.V. Naik, A. V. Kildishev, Y. Barnakov, A. Boltasseva, and V. M.

Shalaev. Effect of metallic and hyperbolic metamaterial surfaces on electric and magnetic dipole emission transitions. *Appl. Phys. B*, 103:553, 2011.

[79] T. Tumkur, G. Zhu, P. Black, Y. A. Barnakov, C. E. Bonner, and M. A. Noginov. Control of spontaneous emission in a volume of functionalized hyperbolic metamaterial. *Applied Physics Letters*, 99(15):151115, 2011.

[80] J. Kim, V. P. Drachev, Z. Jacob, G. V. Naik, A. Boltasseva, E. E. Narimanov, and V. M. Shalaev. Improving the radiative decay rate for dye molecules with hyperbolic metamaterials. *Optics Express*, 20(7):8100–8116, 2012.

[81] S. Kuhn, U. Hakanson, L. Rogobete, and V. Sandoghdar. Enhancement of single-molecule fluorescence using a gold nanoparticle as an optical nanoantenna. *Physical Review Letters*, 97(1):017402, 2006.

[82] F. Tam, G. P. Goodrich, B. R. Johnson, and N. J. Halas. Plasmonic enhancement of molecular fluorescence. *Nano Lett.*, 7(2):496–501, 2007.

[83] M. Toma, K. Toma, P. Adam, J. Homola, W. Knoll, and J. Dostalek. Surface plasmon-coupled emission on plasmonic bragg gratings. *Optics Express*, 20(13):14042–14053, 2012.

[84] Y. Jiang, H. Y. Wang, H. Wang, B. R. Gao, Y. W. Hao, Y. Jin, Q. D. Chen, and H. B. Sun. Surface plasmon enhanced fluorescence of dye molecules on metal grating films. *Journal of Physical Chemistry C*, 115(25):12636–12642, 2011.

[85] O. L. Muskens, V. Giannini, J. A. Sanchez-Gil, and J. Gomez Rivas. Strong enhancement of the radiative decay rate of emitters by single plasmonic nanoantennas. *Nano Lett.*, 7(9):2871–2875, 2007.

[86] K. C. Y. Huang, M. K. Seo, Y. J. Huo, T. Sarmiento, J. S. Harris, and M. L. Brongersma. Antenna electrodes for controlling electroluminescence. *Nature Communications*, 3:1005, 2012.

[87] Dylan Lu, Jimmy J. Kan, Eric E. Fullerton, and Zhaowei Liu. Enhancing spontaneous emission rates of molecules using nanopatterned multilayer hyperbolic metamaterials. *Nature Nanotechnology*, 9:48–53, 2014.

[88] E. Fred Schubert. *Light-Emitting Diodes (2nd Ed.)*. Cambridge University Press, New York, 2006.

[89] Dylan Lu, Jimmy Kan, Eric E. Fullerton, and Zhaowei Liu. Tunable surface plasmon polaritons in ag composite films by adding dielectrics or semiconductors. *Appl. Phys. Lett.*, 98:243114, 2011.

[90] C. Stringari, A. Cinquin, O. Cinquin, M. A. Digman, P. J. Donovan, and E. Gratton. Phasor approach to fluorescence lifetime microscopy distin-

guishes different metabolic states of germ cells in a live tissue. *Proc. Natl. Acad. Sci. USA*, 108(33):13582–13587, 2011.

[91] K. A. Selanger, J. Falnes, and T. Sikkeland. Fluorescence lifetime studies of rhodamin 6g in methanol. *The Journal of Physical Chemistry*, 81(20):1960, 1977.

[92] J. Wang, A. A. Chabanov, D. Y. Lu, Z. Q. Zhang, and A. Z. Genack. Dynamics of mesocopic fluctuations of localized waves. *Phys. Rev. B*, 81:241101 (R), 2010.

[93] R. N. Hall, G. E. Fenner, J. D. Kingsley, T. J. Soltys, and R. O. Carlson. Coherent Light Emission From GaAs Junctions. *Physical Review Letters*, 9:366–368, November 1962.

[94] M. I. Nathan, W. P. Dumke, G. Burns, F. H. Dill, Jr., and G. Lasher. Stimulated Emission of Radiation from GaAs p-n Junctions. *Applied Physics Letters*, 1:62–64, November 1962.

[95] K. Huang, N. Gao, C. Wang, X. Chen, J. Li, S. Li, X. Yang, and J. Kang. Top- and bottom-emission-enhanced electroluminescence of deep-UV light-emitting diodes induced by localised surface plasmons. *Scientific Reports*, 4:4380, March 2014.

[96] D. Fattal, M. Fiorentino, M. Tan, D. Houng, S. Y. Wang, and Raymond G. Beausoleil. Design of an efficient light-emitting diode with 10 ghz modulation bandwidth. *Appl. Phys. Lett.*, 93:243501, 2008.

[97] Min-Ki Kwon, Ja-Yeon Kim, Baek-Hyun Kim, Il-Kyu Park, Chu-Young Cho, Clare Chisu Byeon, and Seong-Ju Park. Surface-plasmon-enhanced light-emitting diodes. *Adv. Materials*, 20:1253–1257, 2008.

[98] Koichi Okamoto and Yoichi Kawakami. High-efficiency ingan/gan light emitters based on nanophotonics and plasmonics. *IEEE JOURNAL OF SELECTED TOPICS IN QUANTUM ELECTRONICS*, 15:1190, 2009.

[99] Koichi Okamoto, Isamu Niki, Axel Scherer, Yukio Narukawa, Takashi Mukai, and Yoichi Kawakami. Surface plasmon enhanced spontaneous emission rate of ingan/gan quantum wells probed by time-resolved photoluminescence spectroscopy. *Appl. Phys. Lett.*, 87(7):071102, 2005.

[100] C. C. Kao, Y. K. Su, C. L. Lin, and J. J. Chen. Localized surface plasmon-enhanced nitride-based light-emitting diode with ag nanotriangle array by nanosphere lithography. *IEEE PHOTONICS TECHNOLOGY LETTERS*, 22(13):984–986, 2010.

[101] C.-Y. Cho, K. S. Kim, S.-J. Lee, M.-K. Kwon, H. Ko, S.-T. Kim, G.-Y. Jung,

and S.-J. Park. Surface plasmon-enhanced light-emitting diodes with silver nanoparticles and SiO2 nano-disks embedded in p-GaN. *Applied Physics Letters*, 99(4):041107, July 2011.

[102] T. Kawashima, H. Yoshikawa, S. Adachi, S. Fuke, and K. Ohtsuka. Optical properties of hexagonal gan. *Journal of Applied Physics*, 82(7):3528–3535, 1997.

[103] E. D. Palik. *Handbook of optical constants of solids*. Academic Press, 1985.

[104] S. Nakamura. GaN Growth Using GaN Buffer Layer. *Japanese Journal of Applied Physics*, 30:L1705–L1707, October 1991.

[105] Max Born and Emil Wolf. *Principles of Optics*. Cambridge University Press, Cambridge, UK, 1999.

[106] Craig F. Bohren and Donald R. Huffman. *Absorption and Scattering of Light by Small Particles*. Wiley, New York, 1998.

[107] G. Mie. Articles on the optical characteristics of turbid tubes, especially colloidal metal solutions. *Annalen Der Physik*, 25(3):377–445, 1908.

[108] P. Debye. The heliograph of spheres of any material. *Annalen Der Physik*, 30(11):57–136, 1909.

[109] H. C. van de Hulst. *Light scattering by small particles*. Structure of matter series. Wiley, New York, 1957.

[110] H. M. Nussenzveig. *Diffraction effects in semiclassical scattering*. Montroll memorial lecture series in mathematical physics. Cambridge University Press, Cambridge ; New York, 1992.

[111] Eugene F. Knott John F. Shaeffer and Michael T. Tuley. *Radar cross section*. Artech House, Boston, 1993.

[112] Christopher J. Morgan and William R. Hendee. *Introduction to nuclear magnetic resonance imaging*. Multi-Media Pub., Denver, 1984.

[113] C. Genet and T. W. Ebbesen. Light in tiny holes. *Nature*, 445(7123):39–46, 2007.

[114] F. J. G. de Abajo. Colloquium: Light scattering by particle and hole arrays. *Reviews of Modern Physics*, 79(4):1267–1290, 2007.

[115] K. A. Willets and R. P. Van Duyne. Localized surface plasmon resonance spectroscopy and sensing. *Annual Review of Physical Chemistry*, 58:267–297, 2007.

[116] J. N. Anker, W. P. Hall, O. Lyandres, N. C. Shah, J. Zhao, and R. P.

Van Duyne. Biosensing with plasmonic nanosensors. *Nature Materials*, 7(6):442–453, 2008.

[117] E. Prodan, C. Radloff, N. J. Halas, and P. Nordlander. A hybridization model for the plasmon response of complex nanostructures. *Science*, 302(5644):419–422, 2003.

[118] L. Novotny and N. van Hulst. Antennas for light. *Nature Photonics*, 5(2):83–90, 2011.

[119] B. Luk'yanchuk, N. I. Zheludev, S. A. Maier, N. J. Halas, P. Nordlander, H. Giessen, and C. T. Chong. The fano resonance in plasmonic nanostructures and metamaterials. *Nature Materials*, 9(9):707–715, 2010.

[120] J. A. Fan, C. H. Wu, K. Bao, J. M. Bao, R. Bardhan, N. J. Halas, V. N. Manoharan, P. Nordlander, G. Shvets, and F. Capasso. Self-assembled plasmonic nanoparticle clusters. *Science*, 328(5982):1135–1138, 2010.

[121] A. Alu and N. Engheta. Achieving transparency with plasmonic and metamaterial coatings. *Physical Review E*, 72(1):016623, 2005.

[122] A. Alu and N. Engheta. Multifrequency optical invisibility cloak with layered plasmonic shells. *Physical Review Letters*, 100(11):113901, 2008.

[123] P. Y. Fan, U. K. Chettiar, L. Y. Cao, F. Afshinmanesh, N. Engheta, and M. L. Brongersma. An invisible metal-semiconductor photodetector. *Nature Photonics*, 6(6):380–385, 2012.

[124] V. A. Tamma, Y. H. Cui, and W. Park. Scattering reduction at near-infrared frequencies using plasmonic nanostructures. *Optics Express*, 21(1):1041–1056, 2013.

[125] N. Papasimakis, V. A. Fedotov, N. I. Zheludev, and S. L. Prosvirnin. Metamaterial analog of electromagnetically induced transparency. *Physical Review Letters*, 101(25):253903, 2008.

[126] S. Zhang, D. A. Genov, Y. Wang, M. Liu, and X. Zhang. Plasmon-induced transparency in metamaterials. *Physical Review Letters*, 101(4):047401, 2008.

[127] N. Liu, L. Langguth, T. Weiss, J. Kastel, M. Fleischhauer, T. Pfau, and H. Giessen. Plasmonic analogue of electromagnetically induced transparency at the drude damping limit. *Nature Materials*, 8(9):758–762, 2009.

[128] Z. C. Ruan and S. H. Fan. Superscattering of light from subwavelength nanostructures. *Physical Review Letters*, 105(1):013901, 2010.

[129] Z. C. Ruan and S. H. Fan. Design of subwavelength superscattering nanospheres. *Applied Physics Letters*, 98(4):043101, 2011.

[130] L. Verslegers, Z. F. Yu, Z. C. Ruan, P. B. Catrysse, and S. H. Fan. From electromagnetically induced transparency to superscattering with a single structure: A coupled-mode theory for doubly resonant structures. *Physical Review Letters*, 108(8), 2012.

[131] F. Monticone, C. Argyropoulos, and A. Alu. Multilayered plasmonic covers for comblike scattering response and optical tagging. *Physical Review Letters*, 110(11):113901, 2013.

[132] F. Monticone, C. Argyropoulos, and A. Alu. Layered plasmonic cloaks to tailor the optical scattering at the nanoscale. *Scientific Reports*, 2:912, 2012.

[133] N. Engheta. Pursuing near-zero response. *Science*, 340(6130):286–287, 2013.

[134] N. S. Lewis. Toward Cost-Effective Solar Energy Use. *Science*, 315:798–, February 2007.

[135] Hank Price, Eckhard Lupfert, David Kearney, Eduardo Zarza, Gilbert Cohen, Randy Gee, and Rod Mahoney. Advances in parabolic trough solar power technology. *Journal of Solar Energy Engineering*, 124(2):109–125, Apr 2002.

[136] I. Gur, K. Sawyer, and R. Prasher. Searching for a Better Thermal Battery. *Science*, 335:1454–, March 2012.

[137] Ucilia Wang. The rise of concentrating solar thermal power. http://www.renewableenergyworld.com/rea/news/article/2011/06/the-rise-of-concentrating-solar-thermal-power, June 2011.

[138] S. Chu and A. Majumdar. Opportunities and challenges for a sustainable energy future. *Nature*, 488:294–303, August 2012.

[139] Z. Crnjak Orel, B. Orel, and M. Klanjsek Gunde. Spectrally selective sno2:f film on glass and black enamelled steel substrates: spray pyrolytical deposition and optical properties. *Solar Energy Materials and Solar Cells*, 26(1-2):105–116, March 1992.

[140] D.D. Allred, M.R. Jacobson, and E.E. Chain. Spectrally selective surfaces by chemical vapor deposition. *Solar Energy Materials*, 12(2):87–129, May 1985.

[141] B. Seraphin. Chemical vapor deposition of spectrally selective surfaces for high temperature photothermal conversion. *Thin Solid Films*, 57:293–297, March 1979.

[142] J. Thornton and J.L. Lamb. Thermal stability studies of sputter-deposited multilayer selective absorber coatings. *Thin Solid Films*, 96:175–183, October 1982.

[143] L.K. Thomas and E.E. Chain. Spectrally selective black tungsten films. *Thin Solid Films*, 105(3):203–211, July 1983.

[144] M. Lira-Cantu, A. Morales Sabio, A. Brustenga, and P. Gomez-Romero. Electrochemical deposition of black nickel solar absorber coatings on stainless steel aisi316l for thermal solar cells. *Solar Energy Materials and Solar Cells*, 87(1-4):685–694, May 2005.

[145] S. N. Patel, O. T. Inal, A. J. Singh, and A. Scherer. Optimization and thermal degradation study of black nickel solar collector coatings. *Solar Energy Materials*, 11:381–399, February 1985.

[146] A. Anderson, O. Hunderi, and C. G. Granqvist. Nickel pigmented anodic aluminum oxide for selective absorption of solar energy. *Journal of Applied Physics*, 51:754–764, January 1980.

[147] V. Teixeira, E. Sousa, M.F. Costa, C. Nunes, L. Rosa, M.J. Carvalho, M. Collares-Pereira, E. Roman, and J. Gago. Spectrally selective composite coatings of cr-cr2o3 and mo-al2o3 for solar energy applications. *Thin Solid Films*, 392(2):320–326, July 2001.

[148] E. Randich and D.D Allred. Chemically vapor-deposited zrb2 as a selective solar absorber. *Thin Solid Films*, 83(4):393–398, Sept 1981.

[149] F. Toor, M. R. Page, H. M. Branz, and H.-C. Yuan. In *37th IEEE Photovoltaic Specialists Conference*, Seattle, Washington, 2011.

[150] R. Braunstein, A. R. Moore, and F. Herman. Intrinsic Optical Absorption in Germanium-Silicon Alloys. *Physical Review*, 109:695–710, February 1958.

[151] Clifford K. Ho, Roderick Mahoney, Andrea Ambrosini, Marlene Bencomo, Aaron Hall, and Timothy N. Lambert. Characterization of pyromark 2500 paint for high-temperature solar receivers. *J. Sol. Energy Eng.*, 136(1):014502, July 2013.

[152] Andrew R. Parker, Zoltan Hegedus, and Richard A. Watts. SolarÍcabsorber antireflector on the eye of an eocene fly. *P. Roy. Soc. Lond. B*, 265(1398):811–815, May 1998.

[153] A. R. Parker and H. E. Townley. Biomimetics of photonic nanostructures. *Nature Nanotechnology*, 2:347–353, June 2007.

[154] Gururaj V. Naik, Bivas Saha, Jing Liu, Sammy M. Saber, Eric A. Stach, Joseph M. K. Irudayaraj, Timothy D. Sandsa, Vladimir M. Shalaev, and Alexandra Boltasseva. Epitaxial superlattices with titanium nitride as a plasmonic component for optical hyperbolic metamaterials. *Proc. Natl. Acad. Sci. U.S.A.*, 111:7546ÍC7551, 2014.

[155] Evgenii E. Narimanov and Igor I. Smolyaninov. Beyond stefan-boltzmann law: Thermal hyper-conductivity. *arXiv:1109.5444v1*, Sep 2011.

[156] Y. Guo, C. L. Cortes, S. Molesky, and Z. Jacob. Broadband super-Planckian thermal emission from hyperbolic metamaterials. *Applied Physics Letters*, 101(13):131106, September 2012.

[157] J. A. Scholl, A. L. Koh, and J. A. Dionne. Quantum plasmon resonances of individual metallic nanoparticles. *Nature*, 483:421–427, March 2012.

[158] K. J. Savage, M. M. Hawkeye, R. Esteban, A. G. Borisov, J. Aizpurua, and J. J. Baumberg. Revealing the quantum regime in tunnelling plasmonics. *Nature*, 491:574–577, November 2012.